Seismic attribute analysis of the Upper Morrow Sandstone and the Arbuckle Group from 3D-3C seismic data at Cutter Field, southwest Kansas

by

Clyde Redger

Submitted to the graduate degree program in Geology and the Graduate Faculty of the University of Kansas in partial fulfillment of the requirements for the degree of Master of Science.

Advisory Committee

Dr. George Tsoflias, Co-Chair

Dr. Don Steeples, Co-Chair

Dr. W. Lynn Watney

Dr. Gene Rankey

Date defended: 4/10/2015

The Thesis Committee for Clyde Redger

certifies that this is the approved version of the following thesis:

Seismic attribute analysis of the Upper Morrow Sandstone and the Arbuckle Group from 3D-3C seismic data at Cutter Field, southwest Kansas

Advisory Committee

Dr. George Tsoflias, Co-Chair

Dr. Don Steeples, Co-Chair

Dr. W. Lynn Watney

Dr. Gene Rankey

Date approved: 4/10/2015

Abstract

Arbuckle Group and Upper Morrow Sandstone reservoirs have pronounced economic and environmental importance to the state of Kansas because of their history of oil production and potential for CO_2 storage. Characterizing and delineating these reservoirs with seismic methods is challenging for a number of geophysical reasons. This study investigates the accuracy with which analysis of post-stack 3D-3C seismic data can delineate Upper Morrow Sandstone reservoirs and predict Arbuckle Group rock properties at Cutter Field in southwest Kansas. P-P and P-SV seismic responses of the Upper Morrow Sandstone and Arbuckle Group are modeled using Zoeppritz' equations and P-impedance inversion is performed. Seismic attributes are extracted at well locations and compared to models. The Upper Morrow Sandstone is below resolution of both the P-P and P-SV data. No significant correlation is evident between amplitudes or inverted P-impedance and Upper Morrow Sandstone thickness. Instantaneous frequency values of 43 ± 2 Hz are observed at well locations where Upper Morrow Sandstone thickness is greater than 5 m whereas values of 45 ± 6 Hz are observed at well locations where thickness is less than 5 m. The difference in the rms instantaneous frequency values is statistically significant at the 90% confidence interval. Well log data from the Arbuckle Group shows an approximate neutron porosity range of 3-13% and an inverse correlation between neutron porosity and P-impedance, significant at the 99.9% confidence interval with a standard error of regression of 2% porosity. Model-based P-impedance inversion and results and flow unit interpretation from well log data suggest that porosity and flow units within the Arbuckle Group can be approximated by a three-layer model. Investigators can draw upon the results of this study to guide seismic acquisition and interpretation practices in geologic settings analogous to Cutter Field.

Acknowledgements

First and foremost, I would like to thank my co-advisors George Tsoflias and Don Steeples for their guidance and support throughout my time at KU. George was a great research mentor and provided much of the direction for this project. Don's knowledge and experience were a valuable resource. He was always available to offer advice and enjoyable conversation. I would like to thank Lynn Watney and Gene Rankey for serving on my committee and providing valuable feedback. I would also like to thank Rick Miller for giving me the opportunity to work at the Kansas Geological Survey for a summer and gain valuable field experience. Lastly, I would like to thank geophysics students Yousuf Fadolalkarem, Brett Judy, Jordan Nolan, Blair Schneider, José Vélez, Chris Perll, Amanda Livers, Sarah Morton, Yao Wang, Bevin Bailey, and Brian Miller for their friendship and support during my time at KU. Support for this project was provided by the Kansas Interdisciplinary Carbonates Consortium. The Cutter 3D-3C seismic data used in this study was acquired with the support of the U.S. Department of Energy and National Energy Technology Laboratory under contract DE-FE-0002056. The Round About seismic data used in this study was donated by Berexco, LLC. Software used in this project was provided by CGG Veritas and IHS.

Table of contents

List of figures and tables

Figures

Tables

Chapter 1: Introduction

Arbuckle Group and Upper Morrow Sandstone (UMS) reservoirs have pronounced economic and environmental importance to the state of Kansas. These reservoirs account for 36% and 3% of cumulative Kansas oil production, respectively (Bhattacharya et al., 2002; Franseen et al., 2004). In addition to its prolific oil production history, the Kansas Arbuckle Group has the potential to store an estimated 1.1-3.8 billion metric tons of CO_2 and is a prime candidate for future carbon capture and storage (CCS) efforts (Carr et al., 2005). Seismic imaging has shown to add little value to the delineation and characterization of these reservoirs. Upper Morrow Sandstone reservoirs are thin, discontinuous, and commonly exhibit weak P-wave reflectivity. The Arbuckle Group consists of dolomitized carbonate platform deposits and suffers from imaging problems that are common within carbonate reservoirs: poor resolution, weak reflectivity, energy scattering by karst, and heterogeneous rock properties.

UMS reservoirs consist of fluvial and estuarine sandstones. Previous attempts to image UMS reservoirs with seismic methods have produced highly variable results. A pervasive theme in the literature is that UMS reservoirs cannot be imaged with conventional P wave surveys due to insufficient contrast between the UMS and encasing shales (Blott and Davis, 1999; Van Dok and Gaiser, 2001; Singh and Davis, 2011). An exception to this finding is a P wave study by Halverson (1988) in which a correlation between reflection amplitude and UMS thickness was observed for sands within the thin-bed regime of 10-15 m. Other successful attempts of imaging UMS reservoirs have relied on additional S wave information. A 3D-3C study by Blott and Davis (1999) found Vp/Vs ratios to be effective for delineating UMS reservoirs, where the UMS has a maximum thickness of 17 m in southeast Colorado.. However, S waves have not proven to be an effective method for overcoming UMS imaging challenges in all cases. Von Dock and

Gaiser (2011) analyzed 3D-3C data acquired over UMS reservoirs in three different study areas and found that P-SV data failed to deliver consistent results.

The Arbuckle Group is Cambrian to Lower Ordovician in age and consists of mostly dolomitized broad carbonate platform strata. Early studies described Arbuckle Group reservoirs as simple homogenous reservoirs with porosity and permeability controlled by fractures and karstic features that developed from prolonged subaerial exposure (e.g., Walters, 1958). This view became ubiquitous among oil producers in Kansas and led to a practice of drilling wells into only the top 3 m of the Arbuckle Group to stay in productive zones and avoid water (Franseen, 2004). Consequently, knowledge of deep Kansas Arbuckle Group strata was scarce until core studies by Franseen (2000) and Franseen et al. (2004) revealed that Arbuckle Group strata can contain complex vertical and lateral heterogeneities. Few attempts to characterize Kansas Arbuckle Group reservoirs with seismic methods can be found in literature. A study by Nissen et al. (2007) in north-central Kansas concluded that P-impedance could not be used to map lateral porosity variations within the Arbuckle. However, the study was limited to study of wells that penetrated only 4 m into the Arbuckle.

This study investigates the ability of 3D-3C seismic methods to accurately delineate UMS reservoirs and to accurately predict rock properties within the Arbuckle Group at Cutter Field in southwest Kansas. The UMS reservoir at Cutter Field has been heavily drilled, making it an ideal location for investigating the capability of seismic methods to image UMS reservoirs. This study seeks to identify correlations between seismic attributes and UMS thickness by modeling seismic attribute responses and comparing them to attributes extracted from field data. Well 15-189-22781, drilled to basement in 2012, offers a rare look through the entire depth of the Arbuckle Group. Cross plots of well logs and inverted P-impedance advance the understanding of rock properties within the Arbuckle Group. This study demonstrates varying degrees of success at overcoming seismic imaging challenges posed by the Arbuckle Group and the Upper Morrow Sandstone at Cutter Field. Investigators can draw upon the results of this study to guide seismic acquisition and interpretation practices in geologic settings analogous to Cutter Field.

Chapter 2: Theory and background

This chapter provides the theoretical framework for the methods used in this study. Body wave propagation is reviewed to introduce the concept and applications of multicomponent seismic data. Reviews of seismic resolution, the convolutional model, and model-based inversion are also provided.

2.1 Body waves

Interpreting 3D-3C seismic data requires an understanding of body wave propagation. The equation of motion for an isotropic elastic medium can be expressed as

$$(\lambda + 2\mu)\nabla\big(\nabla \cdot \boldsymbol{u}(\boldsymbol{x}, t)\big) - \mu\nabla \times \big(\nabla \times \boldsymbol{u}(\boldsymbol{x}, t)\big) = \rho \frac{\partial^2 \boldsymbol{u}(\boldsymbol{x}, t)}{\partial t^2} \qquad (2.1)$$

where λ is the Lamè Constant, μ is the shear modulus, ρ is density, and *u(x,t)* is the displacement vector. Solutions to Eq. (2.1) permit two modes of wave propagation with velocities α and β given by

$$\alpha = \sqrt{\frac{\lambda + 2\mu}{\rho}} \qquad (2.2)$$

and

$$\beta = \sqrt{\frac{\mu}{\rho}}. \qquad (2.3)$$

A full derivation of these solutions can be found in Stein and Wysession (2003). Waves that propagate with velocity α are termed P, or compressional waves whereas waves that propagate with velocity β are termed S, or shear, waves. P waves are longitudinal waves, which means they exhibit particle motion parallel to the direction of propagation. S waves are transverse waves which means they exhibit particle motion perpendicular to the direction of propagation. As transverse waves, S waves can be polarized in more than one plane.

It is convention to express S waves by their vertical and horizontal components termed SV and SH, respectively (Figure 2.1). This convention is convenient because SV and P waves are coupled and undergo mode conversion at reflective interfaces. Mode conversion is the process whereby a fraction of energy from an incident P wave is converted into a SV wave (or vice versa) at a reflective interface. SH waves are not coupled with P waves and do not undergo mode conversion.

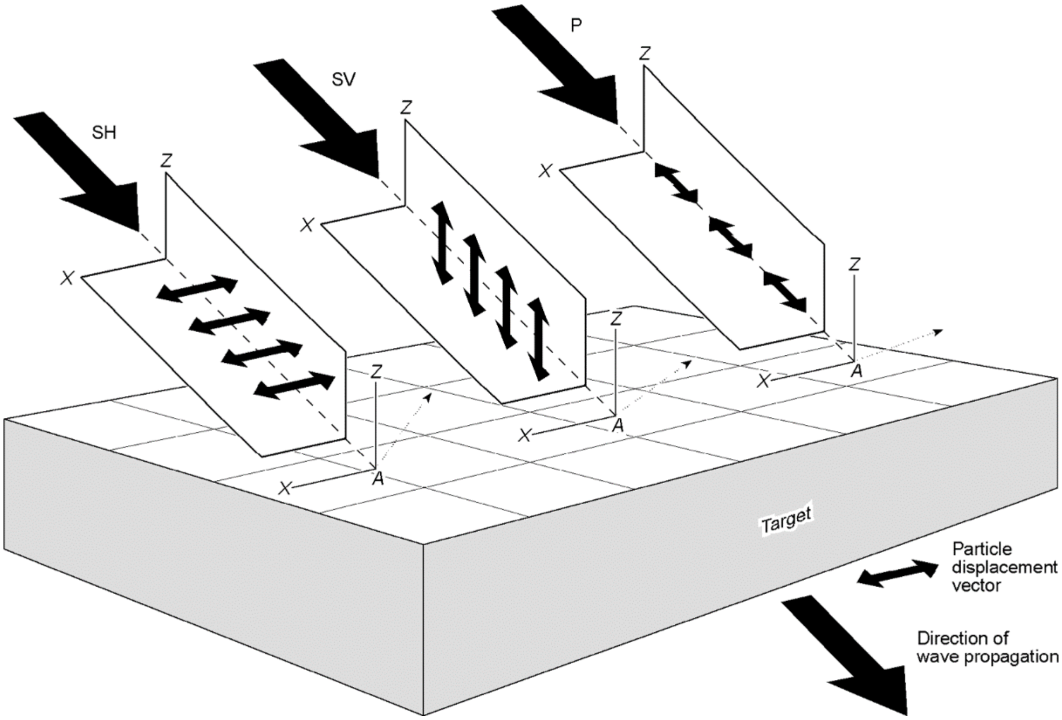

Figure 2.1. Diagram of body waves. Particle displacement of P waves is parallel to the direction of wave propagation. Particle displacement of the SV component is perpendicular to the direction of propagation and in the vertical plane. Particle displacement of the SH component is perpendicular to the direction and in the horizontal plane (From Hardage, 2007).

2.2 Partitioning of energy at a boundary

Partitioning of seismic energy occurs at boundaries at which there is a change in elastic properties. Knott (1899) was the first to derive a solution to the partitioning of energy problem. Knott's derivation begins with displacement potential functions from which displacements can be derived through differentiation. Zoeppritz (1919) developed a more understandable approach by working directly with displacements. The Zoeppritz' equations for an incident P wave can be expressed in matrix form as:

$$\begin{pmatrix} -\sin e & \cos f & \sin e' & \cos f' \\ \cos e & \sin f & \cos e' & -\sin f' \\ \sin 2e & -\frac{\alpha}{\beta}\cos 2f & \frac{\rho'}{\rho}\frac{\alpha}{\alpha'}\left(\frac{\beta'}{\beta}\right)^2 \sin 2e' & \frac{\rho'}{\rho}\frac{\alpha}{\beta'}\left(\frac{\beta'}{\beta}\right)^2 \cos 2f' \\ -\cos 2f & -\frac{\beta}{\alpha}\sin 2f & \frac{\rho'}{\rho}\frac{\alpha'}{\alpha}\cos 2f' & -\frac{\rho'}{\rho}\frac{\beta'}{\alpha}\sin 2f' \end{pmatrix} \begin{pmatrix} A_1/A \\ B_1/A \\ A'/A \\ B'/A \end{pmatrix} \tag{2.4}$$

$$= \begin{pmatrix} \sin e \\ \cos e \\ \sin 2e \\ \cos 2f \end{pmatrix}.$$

From Pujols, (2003)

Variables for Eq. (2.4) are defined in Table 2.1 and Figure 2.2. The values of A1/A and B1/A are referred to as reflection coefficients, whereas the values the A'/A and B'/A are the transmission coefficients. All reflection and transmission angles are related by the constant ray parameter *p*, given by Snell's Law:

$$p = \frac{\alpha}{\sin e} = \frac{\beta}{\sin f} = \frac{\alpha'}{\sin e'} = \frac{\beta'}{\sin f'}. \tag{2.5}$$

In the case of normal incidence (*e=0*), the Zoeppritz’ equations yields

$$B_1 = B' = 0 \tag{2.6}$$

and

$$\frac{A_1}{A} = \frac{\rho'\alpha' - \rho\alpha}{\rho'\alpha' + \rho\alpha}. \tag{2.7}$$

Eq. (2.6) reveals that no mode conversion occurs for an incident P wave with *e=0*. Eq. (2.7) gives the reflection coefficient of a P-P reflection at zero-offset. This equation is frequently used for modeling P-P data because a processed and stacked P-P trace is intended to approximate a zero-offset trace (Liner, 2004).

Variable	**Description**
A	Incident P wave amplitude
A_1	Reflected P wave amplitude
A’	Transmitted P wave amplitude
B_1	Reflected SV wave amplitude
B’	Transmitted SV wave amplitude
e	P wave angle of incidence & reflection
e’	P wave angle of transmission
f	SV wave angle of reflection
f’	SV wave angle of transmission
α	P wave velocity of layer 1
α'	P wave velocity of layer 2
β	SV wave velocity of layer 1
B’	SV wave velocity of layer 2
ρ	Density of layer 1

Table 2.1. Description of variables from Eq. (4).

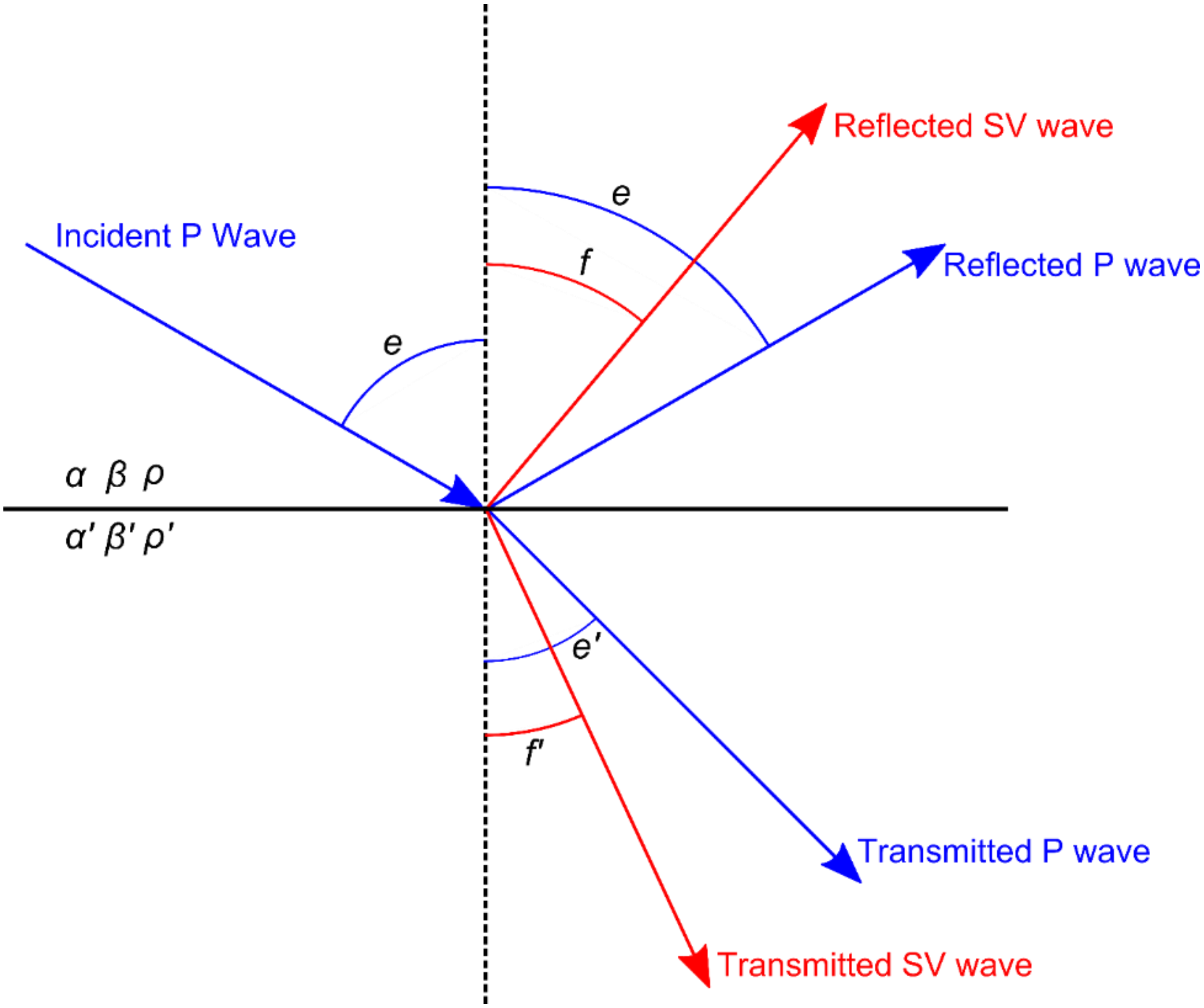

Figure 2.2. Relation between reflection and transmission angles for an incident P wave.

2.3 Shear wave splitting

In anisotropic media, a shear wave will split into two linearly polarized quasi-shear waves (Cerveny, 2001). The prefix "quasi" denotes that the particle motion in these waves is not perfectly orthogonal to the direction of propagation. These waves propagate at different velocities and are referred to as fast and slow shear modes. A comprehensive summary of the theory behind shear wave splitting can be found in Cervney, (2001).

The polarization directions of the fast and slow shear modes can be identified by travel times in azimuthal gathers (Figure 2.3). Shear wave splitting is evident in exploration seismic data sets in areas that contain vertical fractures or have significant difference between its maximum and minimum horizontal stresses. In the case of vertical fractures, the time delay between the fast and slow modes has been shown to be dependent on fracture density and has been used to characterize fractured reservoirs (Sondergeld and Rai, 1992; Mueller, 1992).

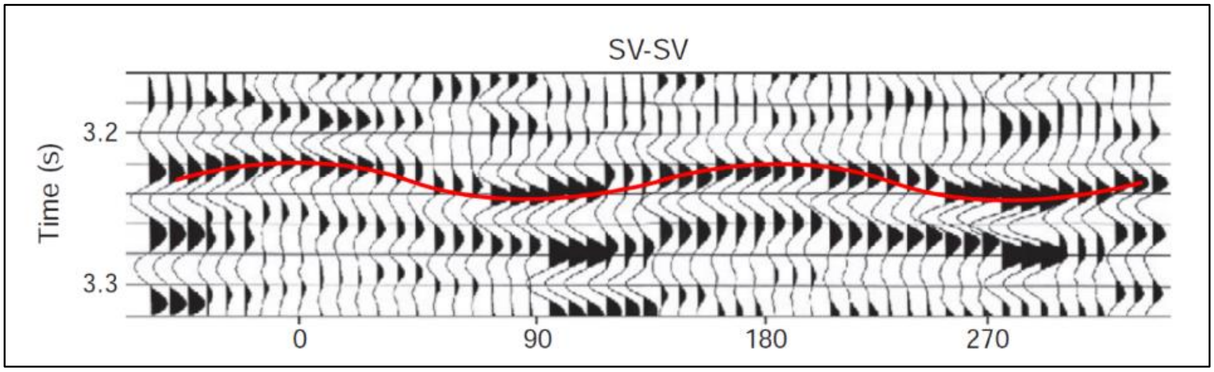

Figure 2.3. . Azimuthal gather of SV-SV data. X-axis units are degrees. Note the sinusoidal nature of reflections due to shear wave splitting. The fast mode is polarized along the 0-180 axis and the slow mode is polarized along the 90-270 axis (Modified from Hardage et al., 2011).

2.4 Multicomponent seismic methods

Although P wave data is generally more practical for seismic exploration, acquiring additional S wave information can be beneficial for imaging interfaces with weak P-P reflectivity, fracture characterization, lithology discrimination, and imaging below gas clouds. Multicomponent seismic surveys simultaneously detect P waves and S waves by placing three-component sensors at each receiver location. The three-component sensors measure ground motion in three orthogonal directions (one vertical and two horizontal), permitting detection of both P wave and S wave particle motion.[1] Multicomponent seismic surveys are classified as three-component (3C) or nine-component (9C). These surveys differ in the type of sources used to generate P waves and S waves. Three-component surveys use only a P wave source to generate P-P and P-SV wave modes.[2] Nine-component surveys use a P wave source, and two orthogonally oriented S wave sources to generate all possible wave modes: P-P, P-SV, SV-SV, SV-P, and SH-SH.

Following acquisition, S wave data must be converted mathematically from inline/crossline coordinates to radial/transverse coordinates (Figure 2.4). Once the coordination transformation is complete, SV-SV and SH-SH data can be processed using the same common-midpoint (CMP) principles used for P-P data. CMP principles do not apply to converted waves data because of the asymmetric nature of converted wave reflections. Whereas CMP processing assumes reflections occur midway between source and receiver, a P-SV reflection point will occur closer to the receiver, and an SV-P reflection point will occur closer to the

---

[1] Four-component sensors can be used for ocean-bottom surveys. These consist of a three-component sensor and a hydrophone.

[2] P wave sources also generate a down-going SV wave field that produces SV-SV and SV-P wave modes. However, energy from SV-SV and SV-P wave modes is generally regarded as noise in 3C surveys.

source. The methodology for overcoming this challenge is known as common conversion point processing (CCP) (Hardage et al., 2011).

In isotropic materials, all SV energy is constrained to the radial plane and all SH energy is constrained to the transverse plane. Energy from a single wave mode found in both planes is evidence of anisotropy and shear wave splitting (Section 2.3). In such cases, fast and slow directions can be identified through examination of azimuthal gathers (as shown previously in Figure 2.3). Stacked radial and transverse volumes are produced from energy found in the radial and transverse directions and stacked fast and slow volumes are produced from energy found in the fast and slow directions.

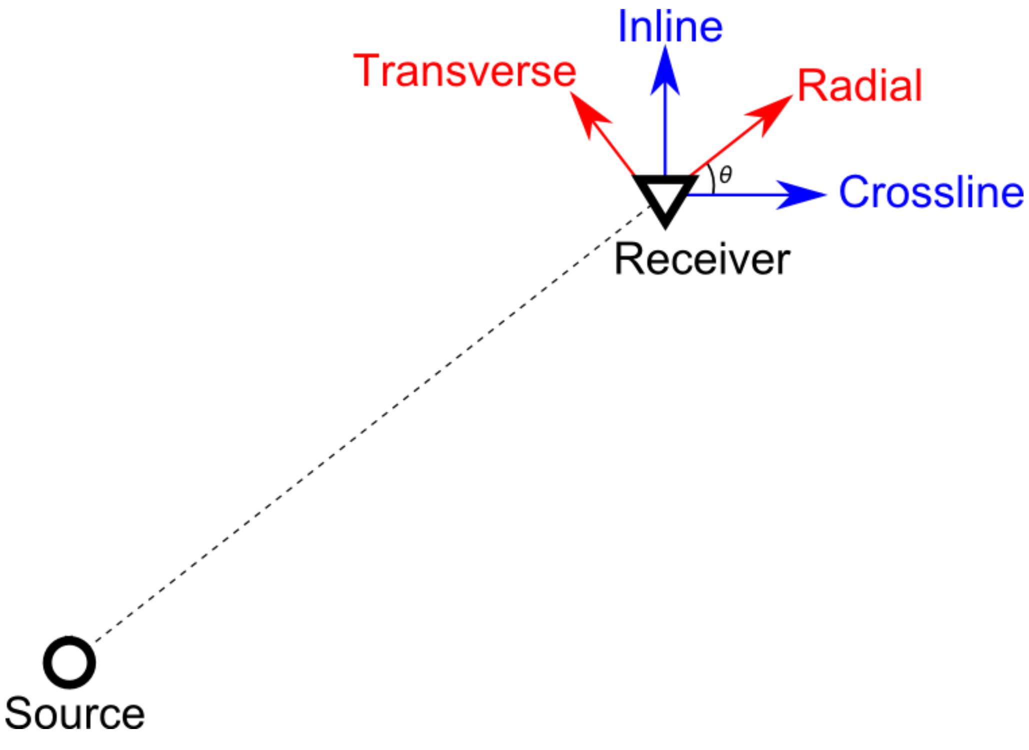

Figure 2.4. Rotation of inline/crossline coordinates to radial/transverse coordinates. The radial direction is defined as the direction that is parallel to the source-receiver line and the transverse direction is defined as the direction perpendicular to the source-receiver line.

2.5 Seismic resolution and tuning

Reservoir thicknesses can be below seismic resolution and must be inferred from the amplitude and shape of the reflected waveform. The vertical resolution limit of seismic data, as defined by the Rayleigh criterion, is 1/4 λ where λ is wavelength. The value of λ can be crudely approximated as

$$\lambda = v \, / f \; , \tag{2.8}$$

where *v* is seismic velocity and *f* is the dominant frequency in the seismic data. Working with finite wavelets, as is the case in exploration seismology, wavelength is better expressed as

$$\lambda = v \, T \; , \tag{2.9}$$

where T is the period or breadth of the wavelet. In this study, modeling is conducted using a Ricker wavelet defined as:

$$Ricker(t) = (1 - 2\pi^2 f^2 t^2) e^{-\pi^2 f^2 t^2}. \tag{2.10}$$

The period of a Ricker Wavelet is given by:

$$T_{Ricker} = \frac{\sqrt{6}}{\pi f}. \tag{2.11}$$

Although geologic beds with thicknesses below the Rayleigh criterion cannot be resolved directly, thickness can, in theory, still be inferred though amplitude analysis (Widess, 1973). This outcome is demonstrated with opposite polarity Ricker wavelet reflections (Figures 2.5 and 2.6). As bed thickness decreases, reflections from the top and bottom interfaces interfere with one another to form a composite waveform. For thicknesses greater than the Rayleigh criterion, the apparent thickness inferred from the location of peaks and troughs is approximately equivalent to true thickness. For thicknesses less than the Rayleigh criterion, apparent thickness diverges from true thickness, and the amplitude of the composite waveform smoothly decays to zero. In high-quality seismic data, these changes in amplitude can be used to infer thicknesses for beds below the Rayleigh criterion. The constructive and destructive interference of wavelets commonly referred to as the “tuning effect”. Apparent velocity, v_A, must be used for calculating the resolution of P-SV data. Apparent velocity is given by

$$v_A = \frac{2}{\frac{1}{\alpha} + \frac{1}{\beta}}, \tag{2.12}$$

where α is P wave velocity and β is S wave velocity (Vermeer, 2012).

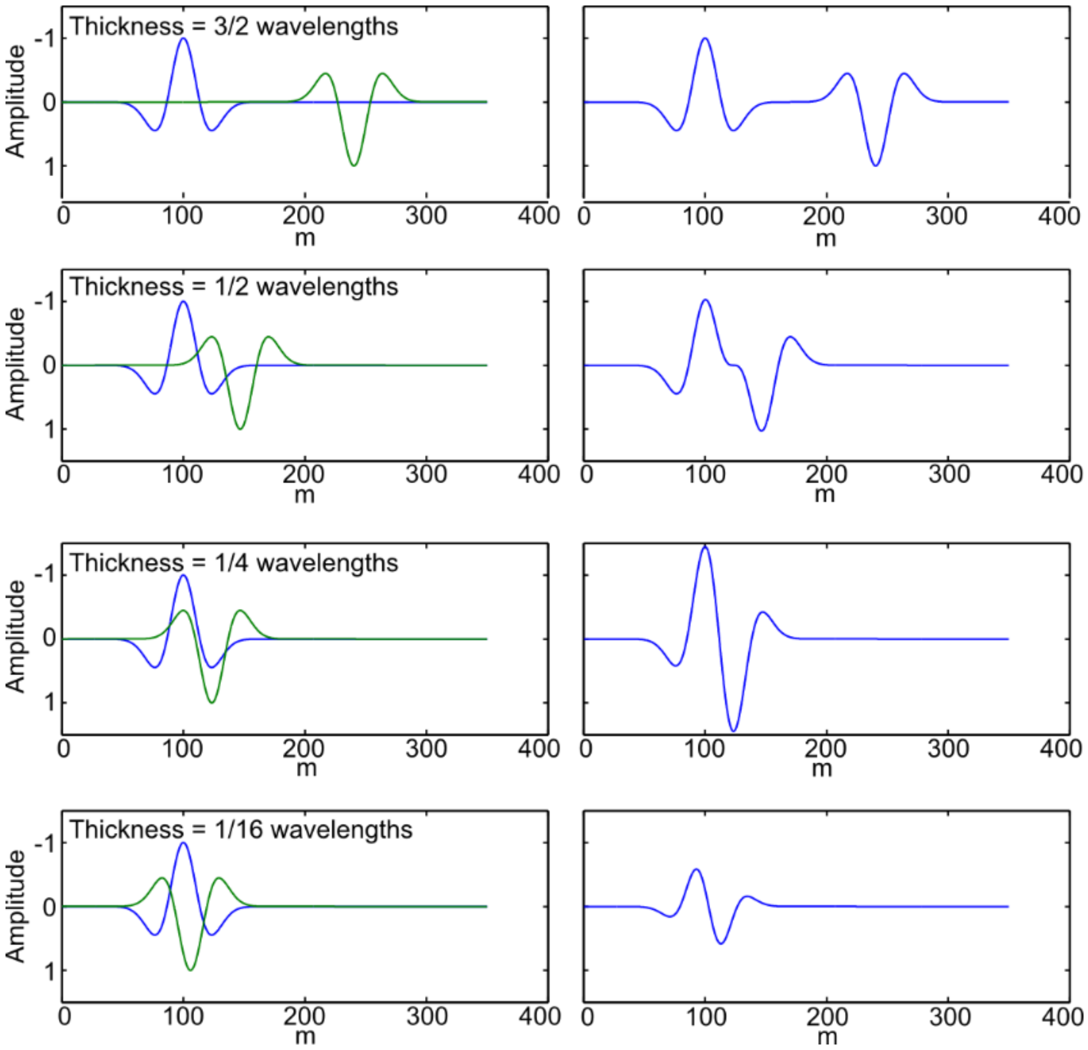

Figure 2.5. Seismic response of opposite polarity, zero phase Ricker wavelet reflections for differing bed thicknesses. Bed thicknesses are expressed in wavelengths as defined in Eq. (2.9). Here, one wavelength is ~47 m. Individual waveforms are shown on the left. Composite waveforms, given by the summation of the individual waveforms, are shown on the right. When thickness falls below 1/4 wavelengths, the two reflections form a composite waveform.

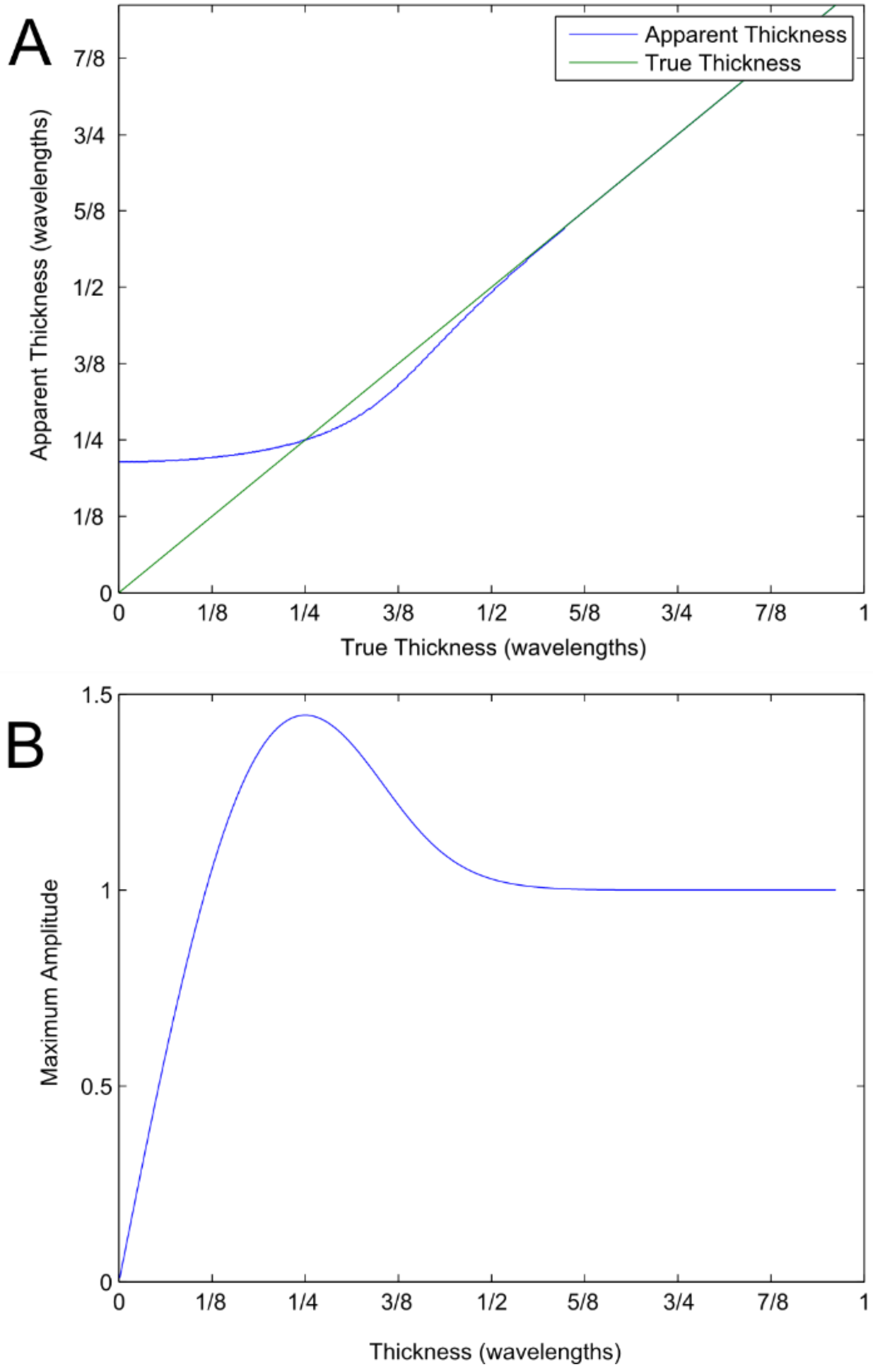

Figure 2.6 (A) Plot of apparent thickness vs true thickness. Apparent thickness diverges from true thickness at the Rayleigh criterion thickness of 1/4 λ. (B) Plot of maximum amplitude versus thickness. Maximum amplitude occurs at the Rayleigh criterion thickness of 1/4 λ.

2.6 Convolutional model

All synthetic seismograms in this study are based on the convolutional model (Figure 2.7). In the convolutional model, a zero offset seismic trace, S(t), is given by

$$S(t) = W(t) * R(t) + Noise \tag{2.12}$$

where R(t) is a time series of reflection coefficients, W(t) is the source wavelet and, "*" is the convolutional operator defined as

$$f(t) * g(t) = \sum_{k} f_k \, g_{t-1}. \tag{2.13}$$

The convolutional model assumes that the source wavelet remains constant and ignores multiples and attenuation (Stein and Wysession, 2003).

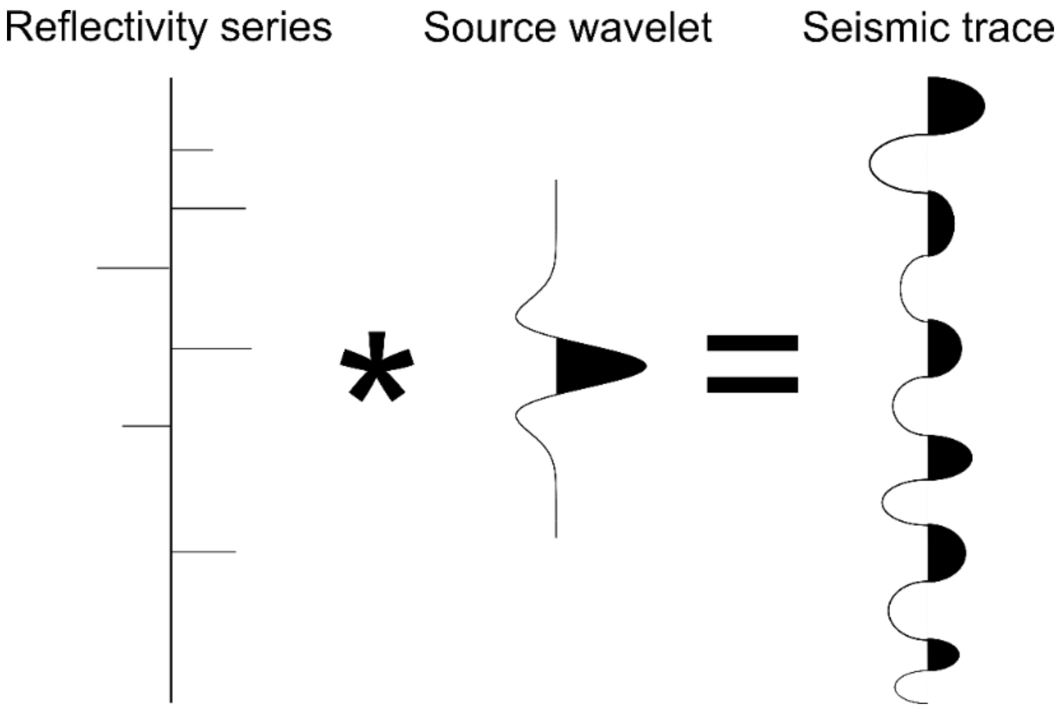

Figure 2.7 Depiction of a seismic trace as described by the convolutional model.

2.7 Model-based inversion

The model based inversion workflow in the Hampson-Russell Strata software estimates reflection coefficients from seismic amplitudes. The estimated reflection coefficients are transformed into impedance volumes, which can be useful for quantitative predictions of rock properties (e.g. porosity, fluid saturation). The process involves estimating a wavelet, building an initial low-frequency model, and perturbing the model to produce a final model that is consistent with the observed seismic data. The wavelet is defined by its frequency and phase content, which is estimated statistically from seismic and well log data. The initial low-frequency impedance model is derived from sonic and density logs and is interpolated through the volume using seismic horizons as structural guides (Hampson-Russell Software Services, 1999).

The Hampson-Russell Strata inversion process is based on the least-squares solution to the seismic inverse problem. For a single seismic trace of N samples, the least-squares solution is given by

$$R = (W^T W)^{-1} W^T S, \tag{2.14}$$

where R is a vector of length N containing unknown reflection coefficients for each time sample, W is an N x N matrix containing the estimated wavelet of length M formatted as

$$\begin{bmatrix} W_1 & 0 & \cdots & 0 \\ W_2 & W_1 & 0 & \vdots \\ \vdots & W_2 & W_1 & 0 \\ W_M & \vdots & W_2 & W_1 \\ 0 & W_M & \vdots & W_2 \\ \vdots & 0 & W_M & \vdots \\ 0 & \vdots & \vdots & W_M \end{bmatrix}, \tag{2.15}$$

and S is a vector of length N containing the observed seismic amplitudes for each time sample.

Given perfect knowledge of S and W, Eq. (2.14) will produce the exact earth reflectivity. However, in practice S always contains noise and W varies spatially and temporally. These effects can produce large cumulative errors to give results that bear little resemble to the exact earth reflectivity. These errors tend to manifest themselves as anomalous low-frequency trends in the derived impedance models. This outcome is a direct consequence of the lack of low-frequency (0-10 Hz) information in exploration seismic data.

Hampson-Russell Strata overcomes this limitation by incorporating the initial low-frequency model from well data. Synthetic traces are computed on the initial model and compared to observed traces. The model is perturbed iteratively to minimize the differences between the synthetic and observed traces (Figure 2.8). A more complete description of the inversion methods used in Hampson-Russell Strata is available in Hampson-Russell Software Services (1999).

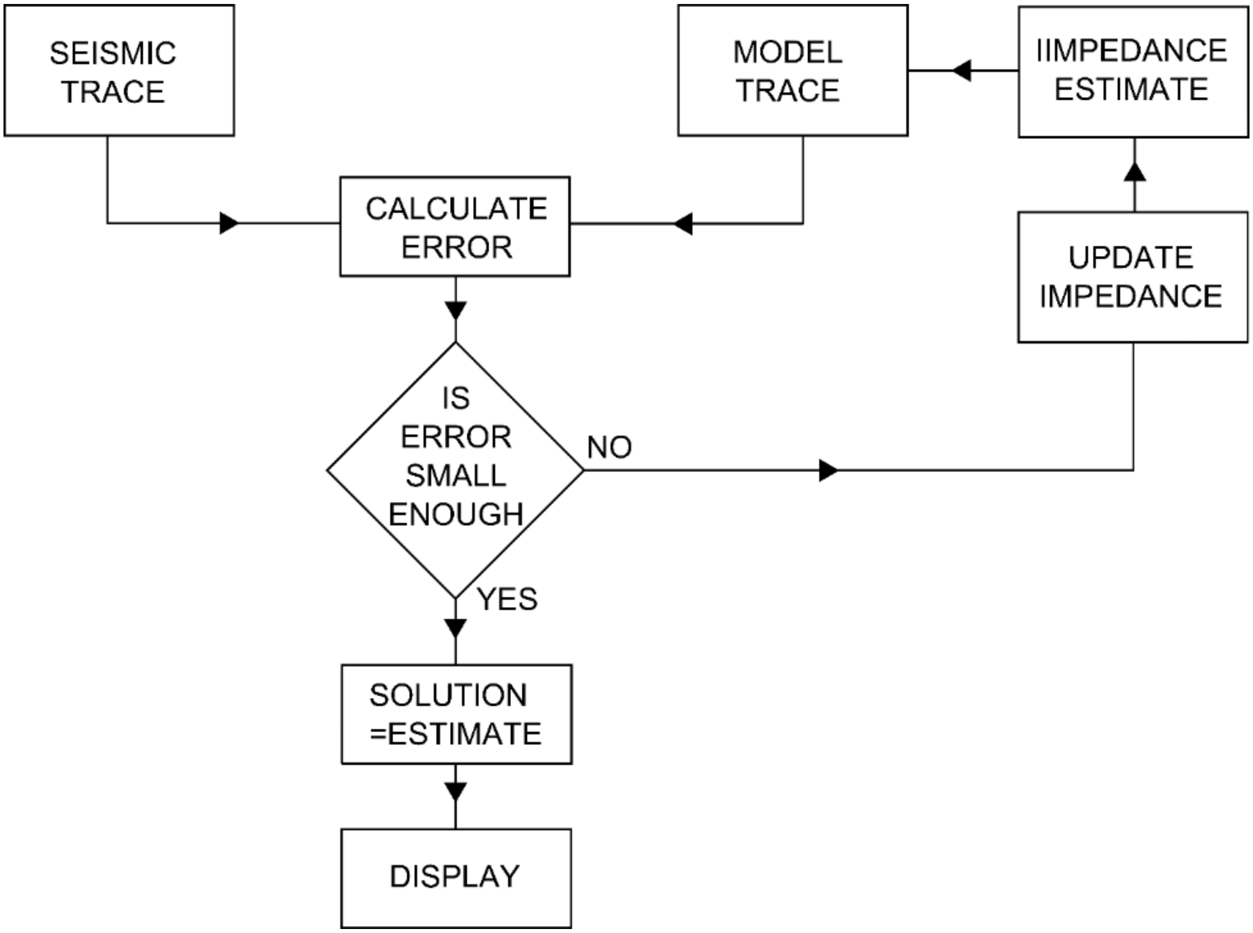

Figure 2.8. Model-based inversion flow chart (Modified from Russell, 1988).

Chapter 3: Seismic and well data sets

The study area is located at Cutter Field in southwest Kansas (Figure 3.1). Seismic data used in this study is from the Cutter 3D-3C survey that was acquired in 2012. Seismic processing for the Cutter 3D-3C survey was completed by Fairfield Nodal. Several seismic volumes were used for analysis:

PSTM stacked P-P
PoSTM stacked P-SV radial
PoSTM stacked P-SV fast
PoSTM stacked P-SV slow.

'PSTM' indicates pre-stack time migration and 'PoSTM' indicates post-stack time migration. The Cutter 3D-3C survey had a bin size of 82.5 ft x 82.5 ft (25.1 m x 25.1 m) and maximum offset of 3465 ft (~1056 m). The area of Cutter 3D-3C survey is ~25 km^2. Fairfield Nodal merged the PSTM stacked P-P volume with the adjacent Round About survey. The total area of the merged P-P data set is ~36 km^2. The Round About survey is located to the northeast of the Cutter 3D-3C survey (Figure 3.2). The merged P-P data set has an inline range of 1 - 283 and a crossline range of 1 – 274. The Cutter 3D-3C survey has an inline range of 1-234 and a crossline range of 1 – 170.

Well log data from 42 wells were included in the analysis (Figure 3.2 & Table 3.1). Well logs include sonic, density, gamma ray, density porosity, and neutron porosity logs. Well 15-189-22781 was drilled to basement in 2012 and was the primary well used for well log analysis in this study because it contains a full suite of logs, is located over the UMS reservoir in Cutter Field, and is the only well in the survey area that penetrates through the Arbuckle Group. All X-Y coordinates are given in the State Plane Coordinate System (SPS) with units of feet. The SPS zone is Kansas South (1502) and the geodetic datum is NAD27.

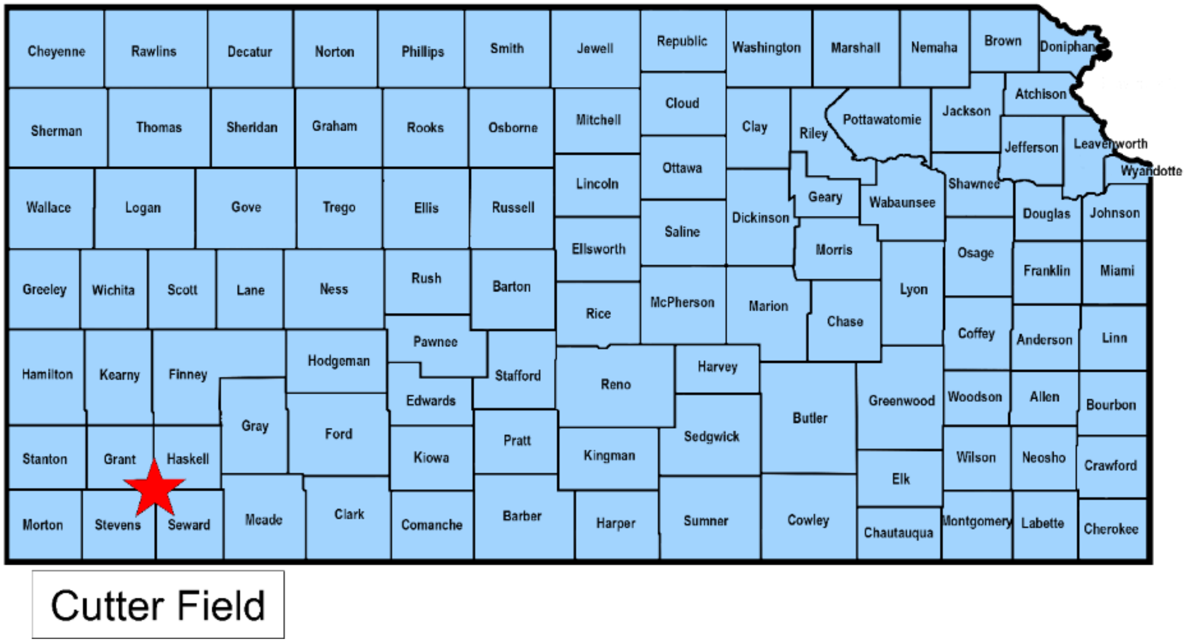

Figure 3.1. Location of Cutter Field in southwest Kansas.

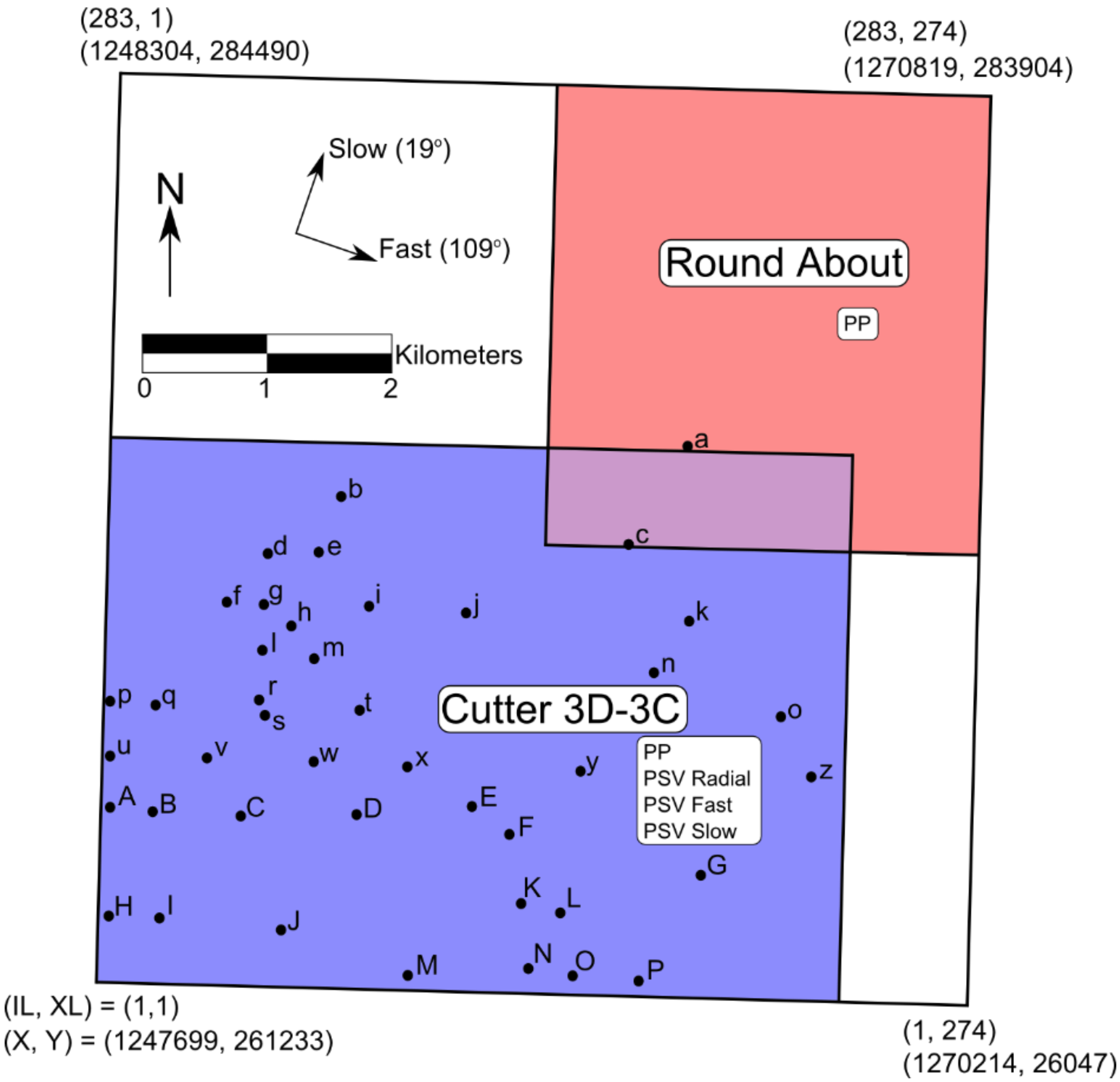

Figure 3.2. Base map of study area. The Cutter 3D-3C survey area is indicated by blue fill. The Round About survey area is indicated by red fill. Fast and slow arrows indicate the directions used for processing the PSV Fast and PSV Slow seismic volumes. Black dots indicate well locations.

Map Symbol	Well API	Total Depth (m)	Logs	Spud Date
a	15-081-21199	1762	DT, GR, NPHI	04/18/1998
b	15-081-20019	1609	DT	10/04/1969
c	15-175-21636	1768	DT, GR, NPHI	08/28/1997
d	15-189-20093	1740	DT, GR	12/22/1970
e	15-189-20021	1739	DT, GR	01/10/1969
f	15-189-22687	1759	DT, GR, RHOB	10/06/2009
g	15-189-10021	1753	DT, GR	08/26/1961
h	15-189-22781	2352	DT, GR, NPHI, RHOB	08/01/2012
i	15-175-10119	1731	DT, GR	01/15/1962
j	15-175-10129	1689	DT	07/09/1964
k	15-175-21588	1752	GR, NPHI	12/11/1996
l	15-189-22560	1766	GR, RHOB	11/14/2006
m	15-189-10022	1728	DT, GR	07/03/1962
n	15-175-21521	1753	DT, GR, NPHI	01/11/1996
o	15-175-21107	1739	GR, NPHI	10/10/1989
p	15-189-20545	1740	GR, NPHI, RHOB	04/08/1981
q	15-189-10119	1771	DT, GR	09/12/1951
r	15-189-00026	2131	DT, GR	12/17/1960
s	15-189-22602	1778	DT, GR, RHOB	08/03/2007
t	15-175-10049	1768	DT, GR	10/11/1961
u	15-189-10029	1759	DT, GR	06/06/1962
v	15-189-10042	1777	DT, GR	08/12/1962
w	15-189-50001	1756	DT, GR	05/15/1962
x	15-175-20018	1737	DT, GR	10/31/1967
y	15-175-21593	1783	GR, NPHI	01/17/1997
z	15-175-20998	1768	GR, NPHI	01/21/1988
A	15-189-20720	1773	GR, NPHI, RHOB	05/15/1984
B	15-189-50000	1756	DT, GR	10/27/1961
C	15-189-10027	1765	DT, GR	07/25/1961
D	15-175-10048	1737	DT, GR	12/21/1961
E	15-175-21217	1762	GR, NPHI	12/05/1991
F	15-175-21197	1757	DT, GR, NPHI, RHOB	09/06/1991
G	15-175-21219	1726	GR, NPHI	11/14/1991

Table 3.1. Well information of wells identified in Figure 3.2. Logs other than DT, GR, NPHI, and RHOB logs are not noted.

Chapter 4: Geologic setting

4.1 Cutter Field

Cutter Field covers 22 km^2 and contains 96 wells. As of September 2014, the field included 26 productive oil wells and 21 productive gas wells. Production occurs from the Marmaton, Morrowan, and Mississippian intervals. Cumulative production as of September 2014 is 7,743,363 bbls of oil and 13,832,908 mcf of gas. Annual production in 2014 was 22,881 bbls of oil and 39,023 mcf of gas (KGS, 2015).

4.2 Anadarko Basin

Cutter Field is located within the Hugoton embayment of the Anadarko basin. The Anadarko basin lies in western Oklahoma, the Texas panhandle, southwestern Kansas, and southeastern Colorado. The basin is bounded to the north by the Cambridge arch, the south by the Wichita and Amarillo uplifts, to the east by the Nemaha and Central Kansas uplifts and to the west by the Cimarron and Los Animas arches.

The basin region was part of a broad epicontinental sea from Late Cambrian though Mississipian time. Deposition during this time was characterized by shallow-marine carbonates, including the Arbuckle Group, and some fine silicilastics. The present boundaries of the basin were formed primarily by tectonic activity during Pennsylvanian time, highlighted by the sharp uplift of the Wichita-Amarillo block and downward warping of the crust beneath the basin. Pennsylvanian deposits, include coarse siliciclasitcs, marine shales, sandstones, and limestones. Permian though Holocene time was characterized by deposition of Permian carbonates, red beds, and evaporites. Thin post-Permian strata were deposited during this time, but most were eroded during late Jurassic/early Cretaceous and late Cretaceous/middle Tertiary uplifts (Johnson, 1989) (Figure 4.1).

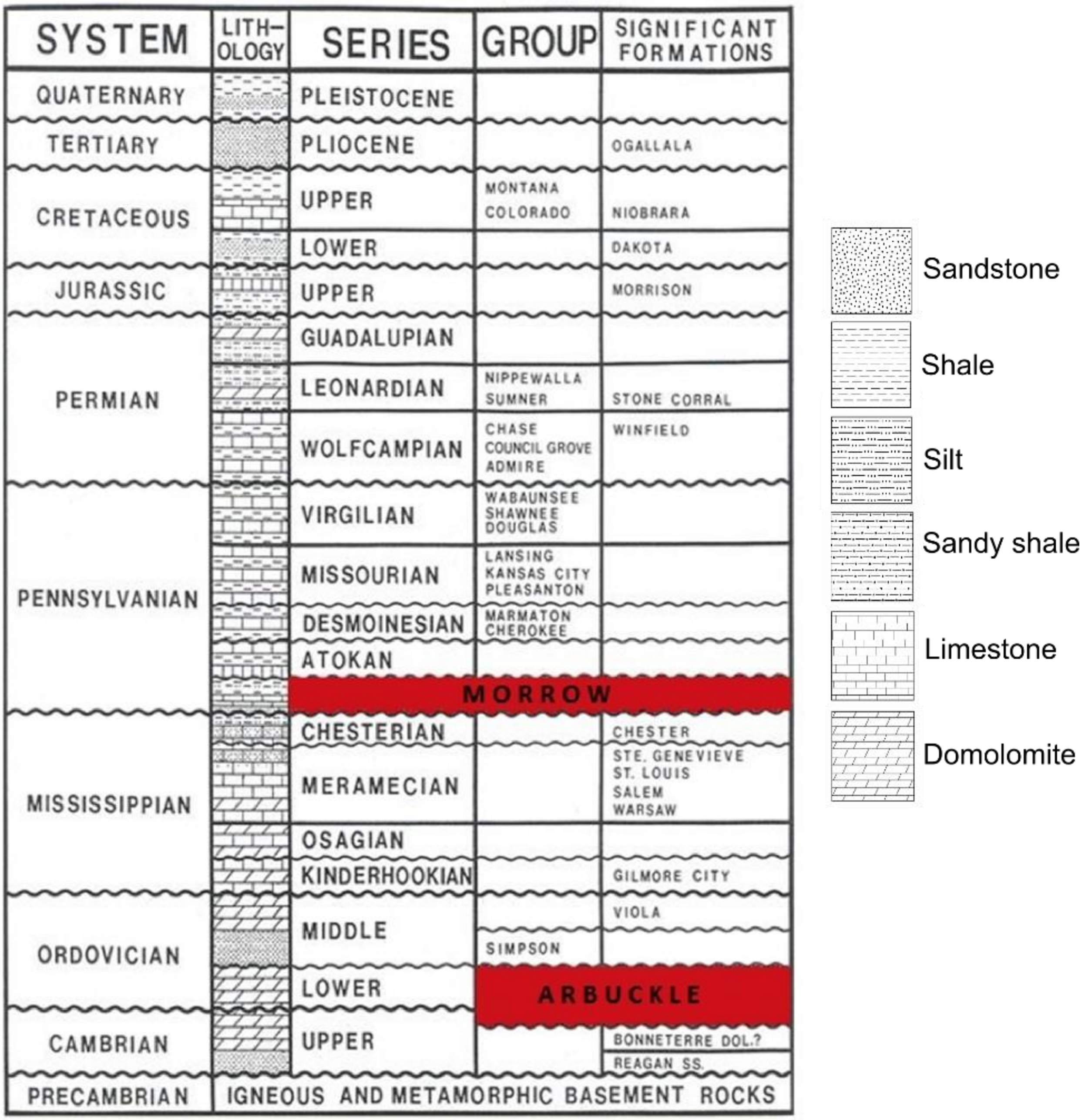

SYSTEM	LITHOLOGY	SERIES	GROUP	SIGNIFICANT FORMATIONS
QUATERNARY		PLEISTOCENE		
TERTIARY		PLIOCENE		OGALLALA
CRETACEOUS		UPPER	MONTANA COLORADO	NIOBRARA
		LOWER		DAKOTA
JURASSIC		UPPER		MORRISON
PERMIAN		GUADALUPIAN		
		LEONARDIAN	NIPPEWALLA SUMNER	STONE CORRAL
		WOLFCAMPIAN	CHASE COUNCIL GROVE ADMIRE	WINFIELD
PENNSYLVANIAN		VIRGILIAN	WABAUNSEE SHAWNEE DOUGLAS	
		MISSOURIAN	LANSING KANSAS CITY PLEASANTON	
		DESMOINESIAN	MARMATON CHEROKEE	
		ATOKAN		
		MORROW		
MISSISSIPPIAN		CHESTERIAN		CHESTER
		MERAMECIAN		STE. GENEVIEVE ST. LOUIS SALEM WARSAW
		OSAGIAN		
		KINDERHOOKIAN		GILMORE CITY
ORDOVICIAN		MIDDLE	SIMPSON	VIOLA
		LOWER	ARBUCKLE	
CAMBRIAN		UPPER		BONNETERRE DOL.? REAGAN SS.
PRECAMBRIAN	IGNEOUS AND METAMORPHIC BASEMENT ROCKS			

Figure 4.1. Stratigraphic column of southwestern Kansas with Arbuckle and Morrow intervals highlighted in red. Modified from Salcedo (2004).

4.2 Arbuckle Group deposition

The Arbuckle Group is part of the "great American carbonate bank" deposited on the Laurentian continent during the Cambrian and early Ordovician (Figure 4.2). Arbuckle strata have been interpreted as, "platform deposits dominated by ramp-type subtidal to peritidal carbonates" (Franseen, 2000). This shallow marine environment persisted throughout the deposition of the Arbuckle (Bliefnick, 1992). Subaerial exposure during the Middle Ordovician produced extensive karst features. In Kansas, the Arbuckle rocks are predominantly dolomite but also contain chert, sand, and small amounts of glauconite and pyrite (Merriam, 1963). The Arbuckle is present across the majority of Kansas and thickens from north to south (Figure 4.3). Production in Kansas occurs primarily along the Central Kansas Uplift.

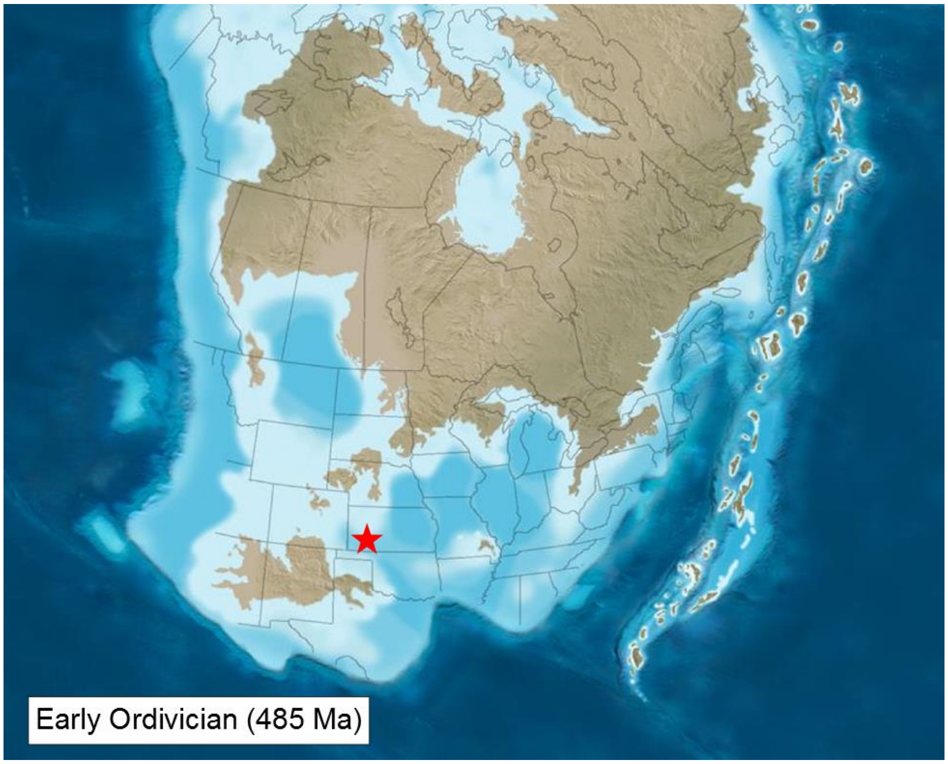

Figure 4.2. North American paleogeography during time of Arbuckle Group deposition (Map by Ron Blakey, Colorado Plateau Geosystems, Arizona, USA). The red star indicates the location of Cutter Field.

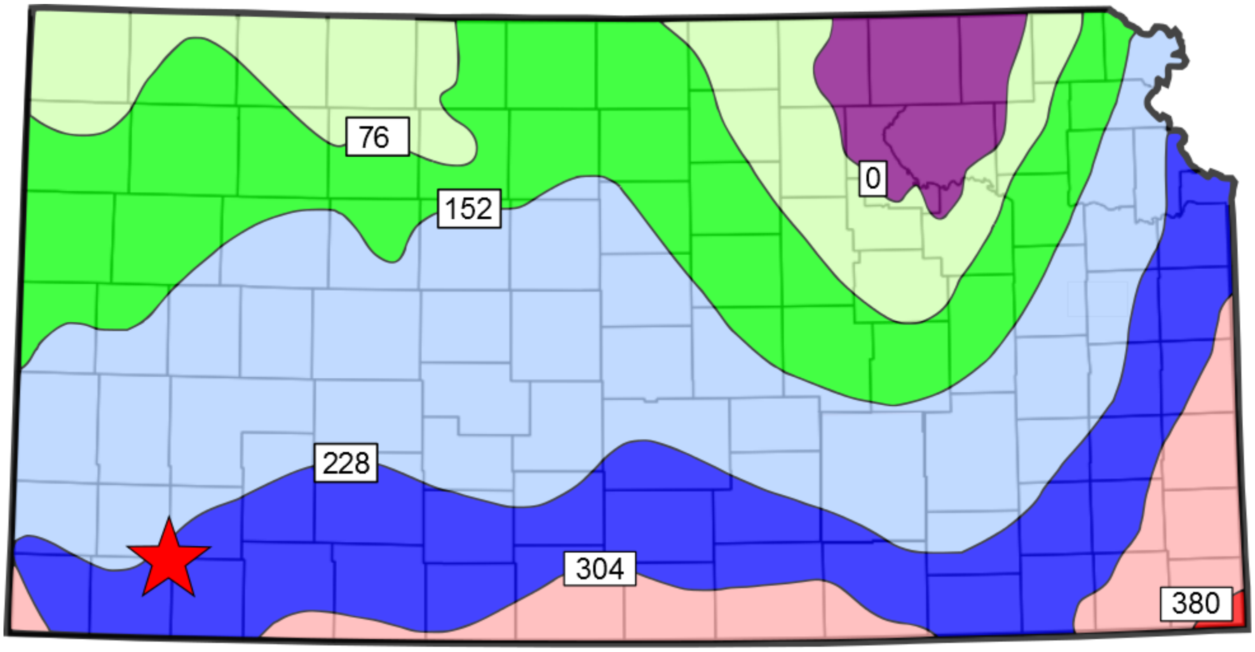

Figure 4.3. Arbuckle Group isopach in meters. Contour interval is 76 m (250 ft) (Modified from Merriam, 1963). The red star indicates the location of Cutter Field.

4.4 Morrow deposition

The Morrow Formation unconformaby overlies Mississippian units, and is disconformably overlain by Atokan Series. Morrow strata in the Anadarko basin region represents deposits of environments that ranged from fluvial to offshore marine (Figure 4.4). The Morrow is divided informally into upper and lower members. The Lower Morrow is dominated by offshore marine shale and shoreface sandstone. Peritidal platform carbonates are present in some areas, particularly along the Colorado-Kansas border. Upper Morrow deposits consist of marine shale and transgressive valley-fill sequences (Figure 4.5). At least seven cycles of relative change in sea level took place during deposition of Upper Morrow strata. Fluvial environments persisted during lowstands, and produced valley incisions. During relative rises in sea level, valley incisions were filled sequentially by fluvial sandstone, esturian sandstone, and marine shale (Wheeler et al., 1990). Point-bar sands have been the primary exploration target within the Upper Morrow (Halverson, 1988).

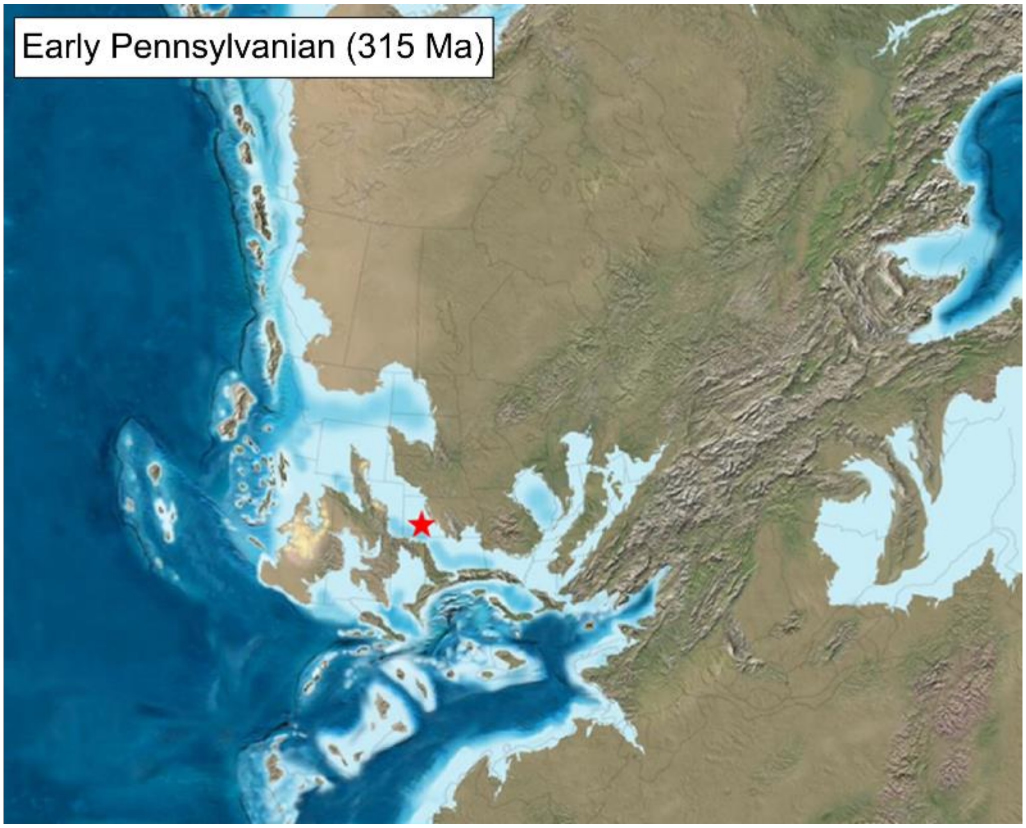

Figure 4.4. North American paleogeography during time of Morrow deposition showing offshore marine environment at the location of Cutter Field, indicated by the red star. (Map by Ron Blakey, Colorado Plateau Geosystems, Arizona, USA). During Morrow deposition, the environment of the Anadarko Basin alternated between fluvial and offshore marine.

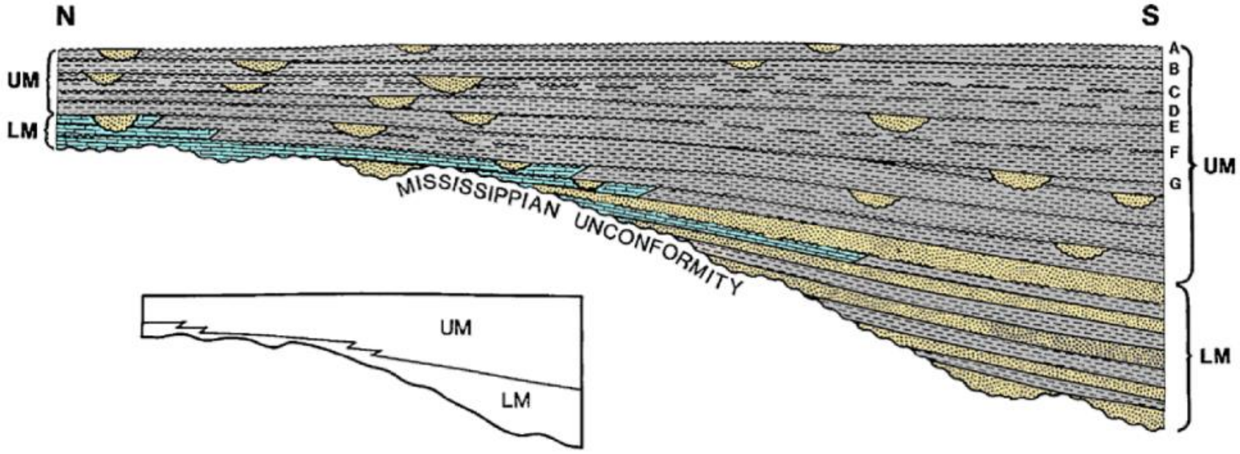

Figure 4.5 Cross section of the Lower and Upper Morrow along the Colorado-Kansas border (Modified from Wheeler et al., 1990). LM represents "Lower Morrow" and UM represents "Upper Morrow".

Chapter 5: Conventional interpretation

5.1 P-P well-to-seismic tie

A time-depth relationship for the P-P seismic data was generated through a well-to-seismic tie completed using well 15-189-22781 in the Hampson-Russell Geoview software package. There are four primary steps to completing a well-to-seismic tie: (1) estimating a wavelet, (2) computing a zero offset reflectivity series from computed impedance logs, (3) convolving the wavelet with the reflectivity series to produce a synthetic trace, and (4) shifting the synthetic trace in time to find the optimal time-depth correlation at which the modeled synthetic trace closely approximates the observed trace at the well location.

A zero phase statistical wavelet was extracted from the seismic volume using a time window of 300-1100 ms and a trace range of inlines 50-150 and crosslines 50-150. The statistical wavelet, termed “P-P Statistical”, had a dominant frequency of 42 Hz, bandwidth of 8 Hz – 78 Hz, and period of 20 ms (Figure 5.1). A zero offset reflectivity series was computed using sonic and density well logs from well 15-189-22781 and was convolved with the statistical wavelet to generate a synthetic trace. A representative trace for the location of well 15-189-22781 was extracted from the P-P volume by averaging a 3 x 3 grid of traces surrounding the well location. Averaging was performed to reduce the impact of anomalous data that may be present in individual traces. A good qualitative character match between peaks and troughs on the synthetic and the extracted trace was obtained by matching the peak at 1200 m in the synthetic trace with the peak at 690 ms in the extracted trace. After completing the time shift, phase rotations ranging from -180 degrees to 180 degrees in increments of one degree were applied to the statistical wavelet to determine the wavelet phase that provided the maximum correlation coefficient between the synthetic and observed traces. A phase rotation of 96 degrees provided the highest correlation coefficient and was applied to the wavelet. The correlation coefficient for the well-to-seismic tie completed with the wavelet P-P Statistical and calculated over a window of 680 – 1140 ms was 0.74. This window represents the entire length of the sonic log at well 15-189-22781.

After an initial time-depth correlation is derived, the “extract wavelet using wells” feature can be employed to further improve the well-to-seismic tie correlation. This feature incorporates well log data into the wavelet extraction process and provides a direct measurement of wavelet phase. This workflow was completed using the “constant phase” option and a time window of 680 – 1140 ms. The extracted wavelet, termed “P-P 22781”, had a dominant frequency of 39 Hz, bandwidth of 8 – 72 Hz, and phase of 88 degrees. (Figure 5.1). The remainder of the well-to-seismic tie procedure was repeated with the new wavelet. A phase rotation was not necessary since the wavelet phase was directly measured during the extraction process. A 10 ms stretch was applied to the lower half of sonic log to improve the correlation between the synthetic and observed trace peaks near 1010 ms. The final correlation coefficient for the well-to-seismic tie completed with wavelet P-P 22781 and calculated over a window of 680 ms – 1140 ms was 0.89 (Figure 5.2).

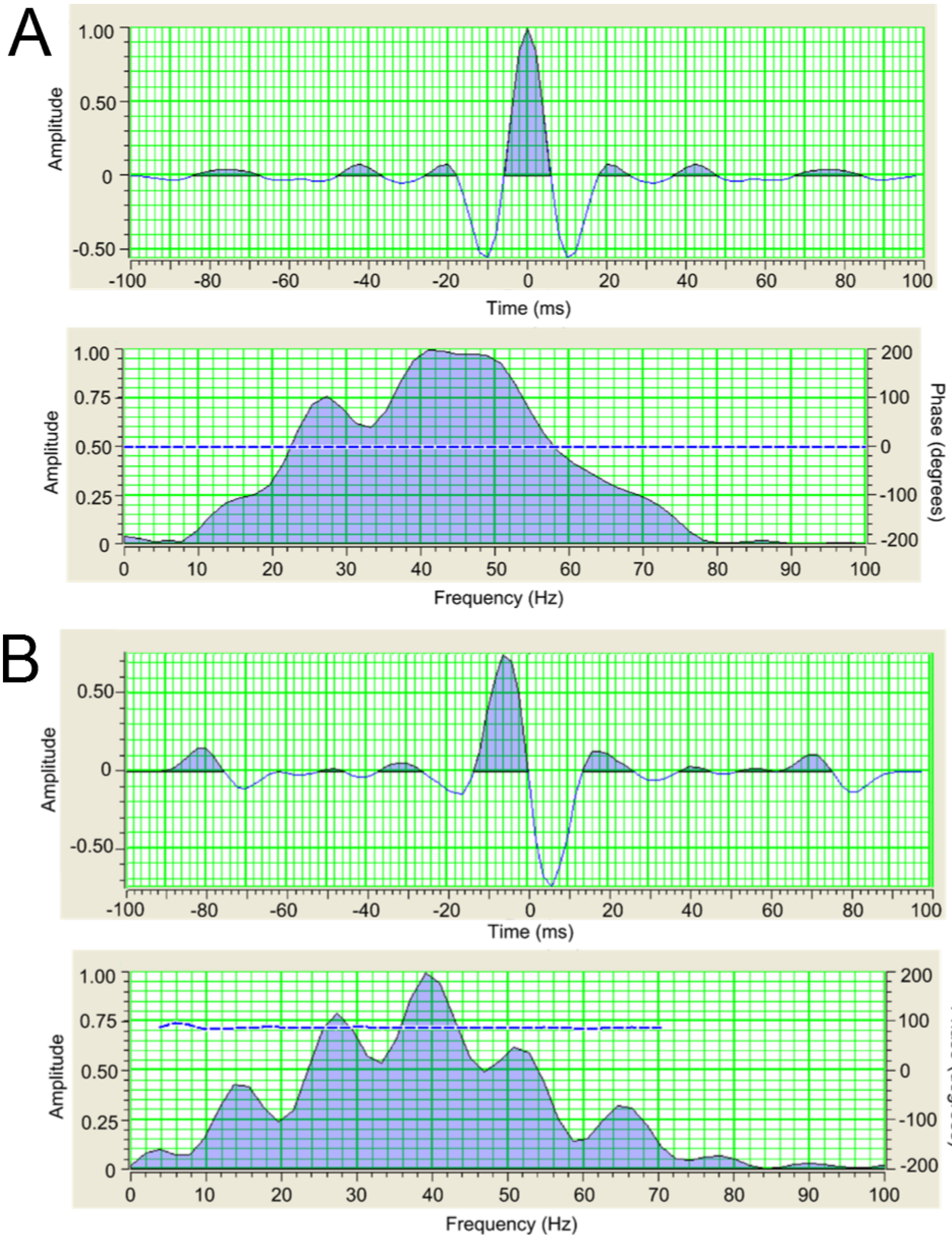

Figure 5.1. (A) Wavelet P-P Statistical estimated from P-P seismic data over a window of 300-1100 ms. (B) Wavelet P-P 22781 estimated from seismic and well log data over a window of 680-1140 ms. Phase = 88 degrees. The wavelet extraction reveals the P-P data to have a dominant frequency of ~40 Hz and a phase of ~90 degrees.

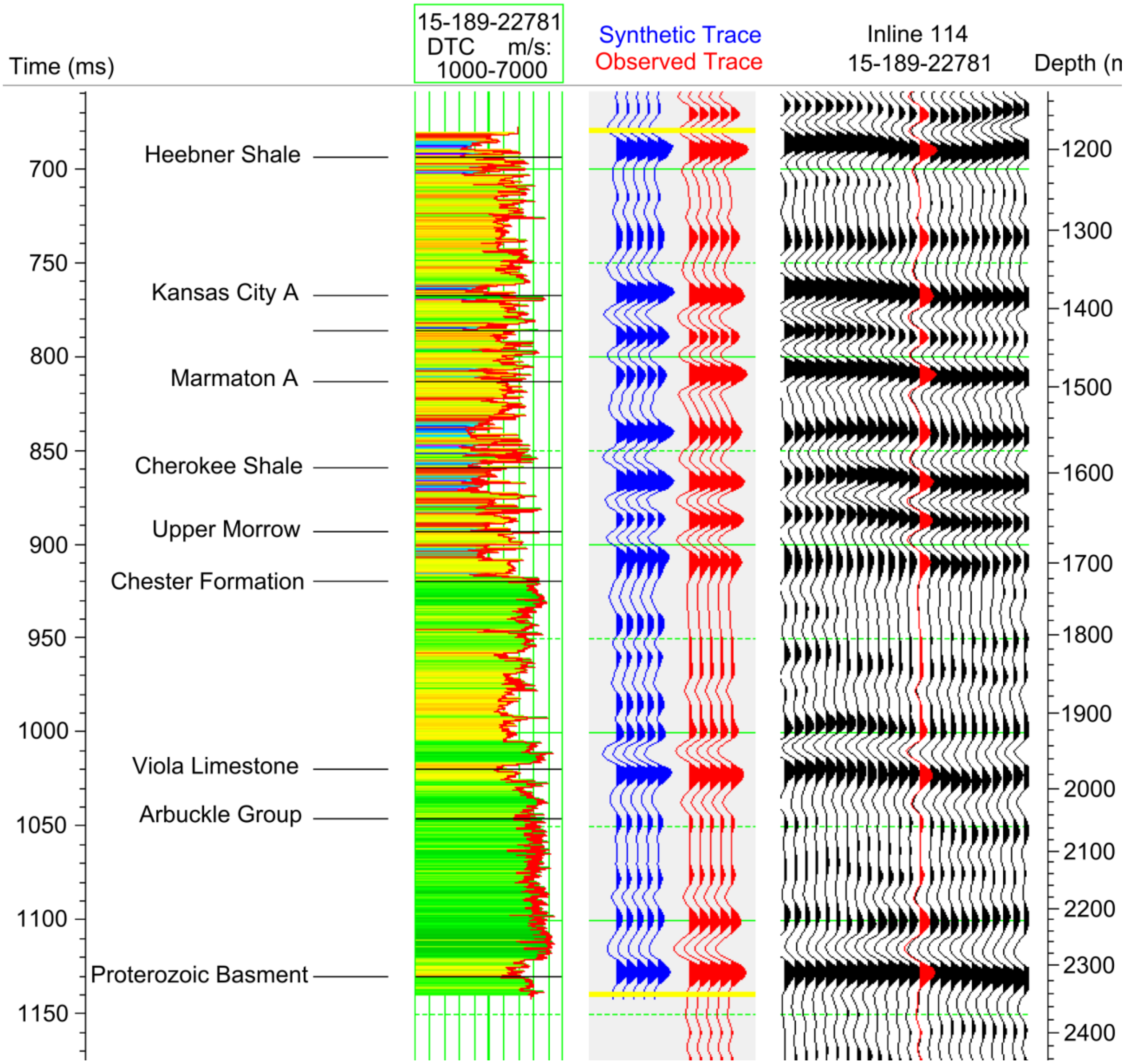

Figure 5.2. P-P well-to-seismic tie at well 15-189-22781. Correlation coefficient = 0.89 (680-1140 ms).

5.2 P-SV frequency filtering

Frequency content of seismic data decreases with depth because higher frequencies attenuate more rapidly than lower frequencies. Yet in the P-SV data, high frequencies (>40 Hz) are visible in amplitude spectrum of the P-SV data for times greater than 1600 ms. There is no physical mechanism that can support the appearance of high frequency P-SV signal for times greater than 1600 ms, and so the high frequency content was assumed to be noise. Prior to completing the P-SV well-to-seismic tie, a low pass filter with a cutoff frequency of 40 Hz was applied to all three P-SV volumes (Figure 5.3). The low pass filter enhanced the P-SV signal for times greater than 1600 ms (Figure 5.4).

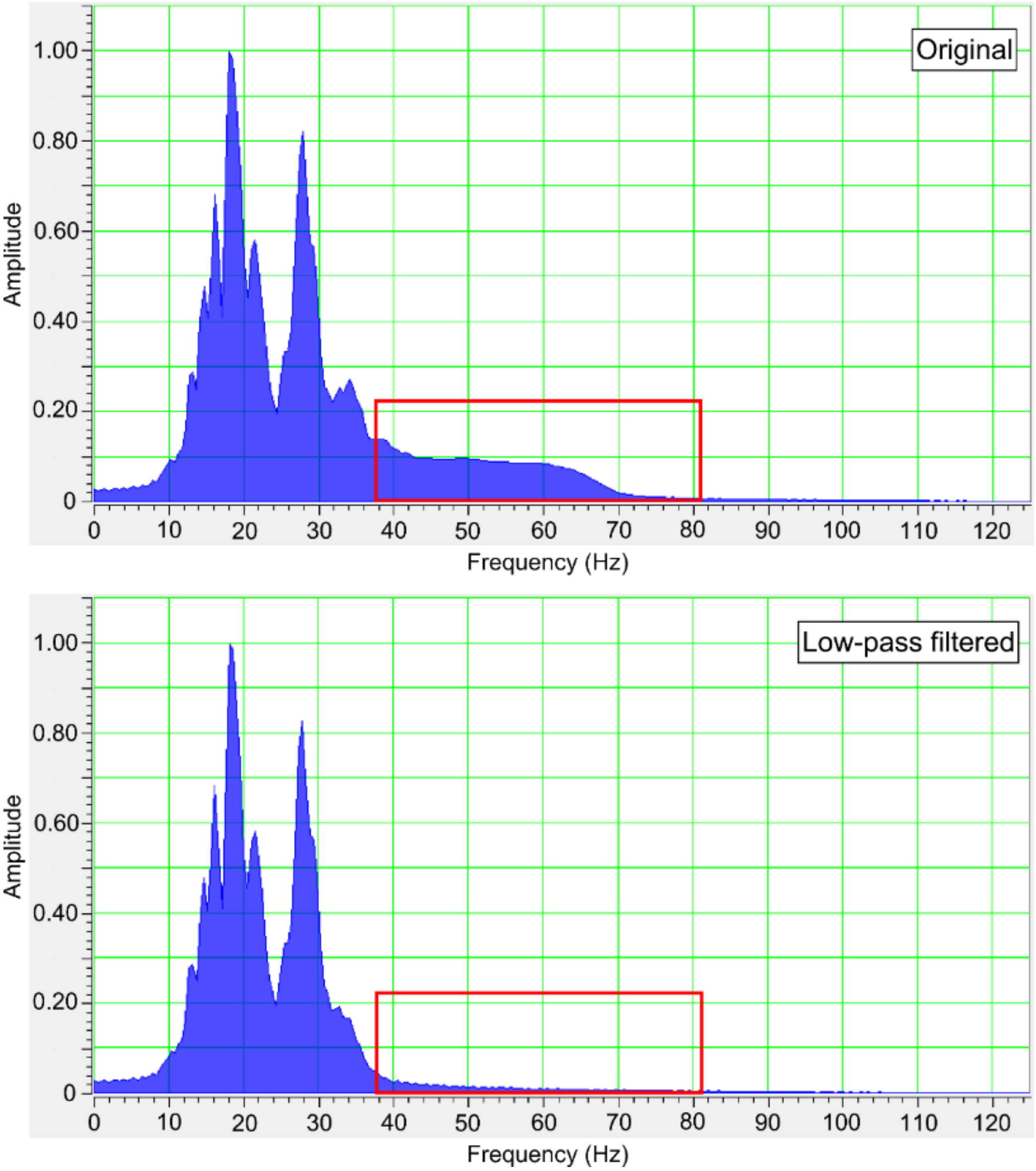

Figure 5.3. Comparison of P-SV amplitude spectrums before and after low-pass filtering.

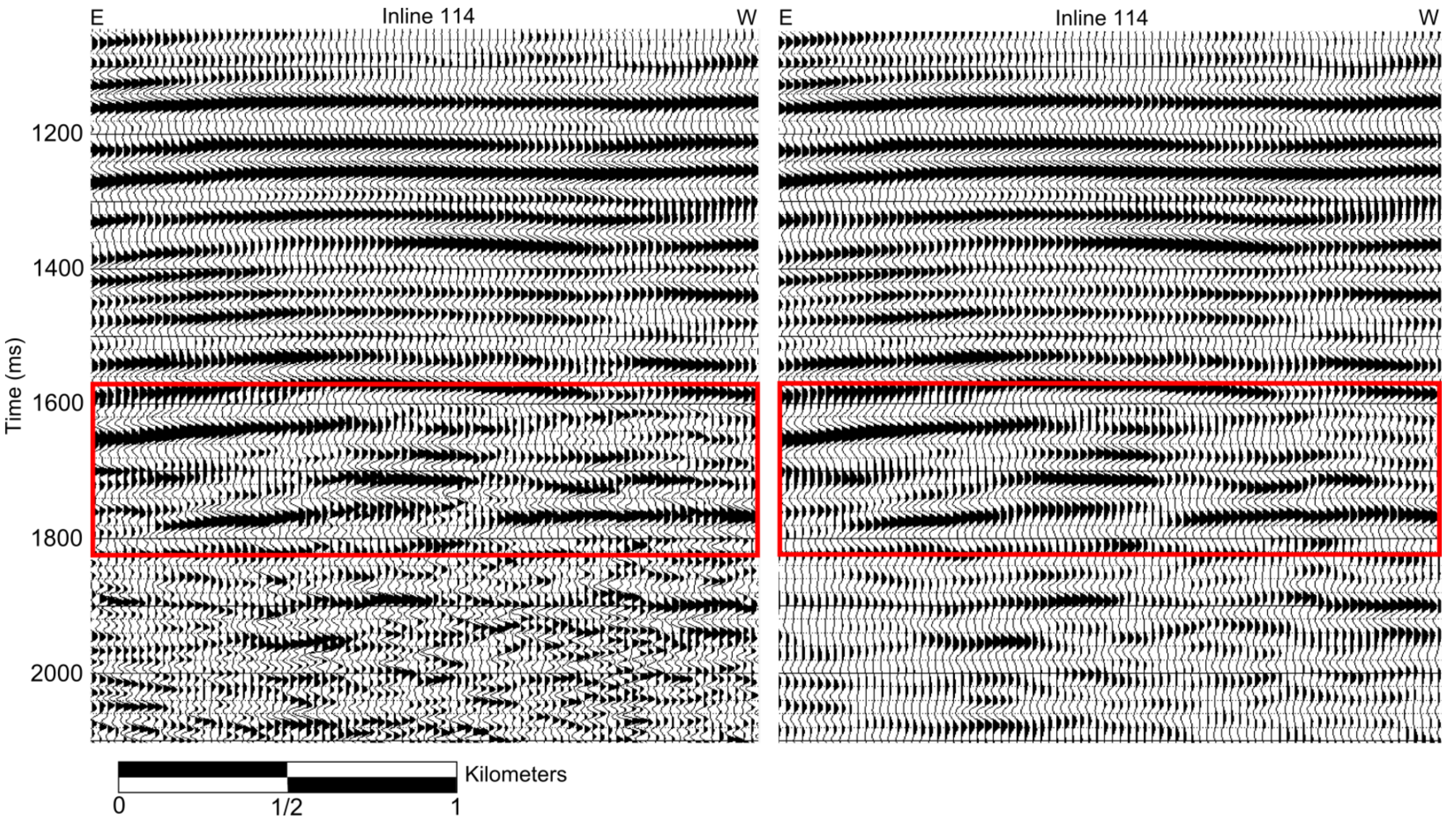

Figure 5.4. Comparison of P-SV profiles before and after low-pass filtering

5.3 P-SV well-to-seismic tie

The well-to-seismic tie for the P-SV data was generated using the Hampson-Russell ProMC software package. The P-SV well-to-seismic tie procedure is similar to that followed for the P-P data with one exception pertaining to the computation of the reflectivity series. Since no P-SV reflections occur at zero offset, incidence angles greater than zero must be employed to generate P-SV synthetic traces. P-SV synthetic traces in this procedure were calculated using an incidence angle of 25 degrees.

The statistical wavelet for the P-SV data was extracted from the survey at a time window of 1000 -1800 ms and a trace range of inlines 50-150 and crosslines 50-150. The extracted wavelet termed, “P-SV Statistical,” has dominant frequency of 19 Hz, bandwidth of 10 – 40 Hz, and period of 42 ms (Figure 5.5). The synthetic trace peak at 1200 m was matched with the observed trace peak at 1150 ms. A maximum correlation coefficient of 0.67 was obtained with a phase rotation of 96 degree (Figure 5.6). The “wavelet extraction using well” procedure, described in section 5.1, was attempted but did not improve the P-SV well-to-seismic tie. A good qualitative character match with a correlation coefficient of 0.84 is observed within the time window of 1100 ms – 1400 ms, which includes the UMS. The character match is markedly worse for times greater than 1400 ms, which includes the Arbuckle Group.

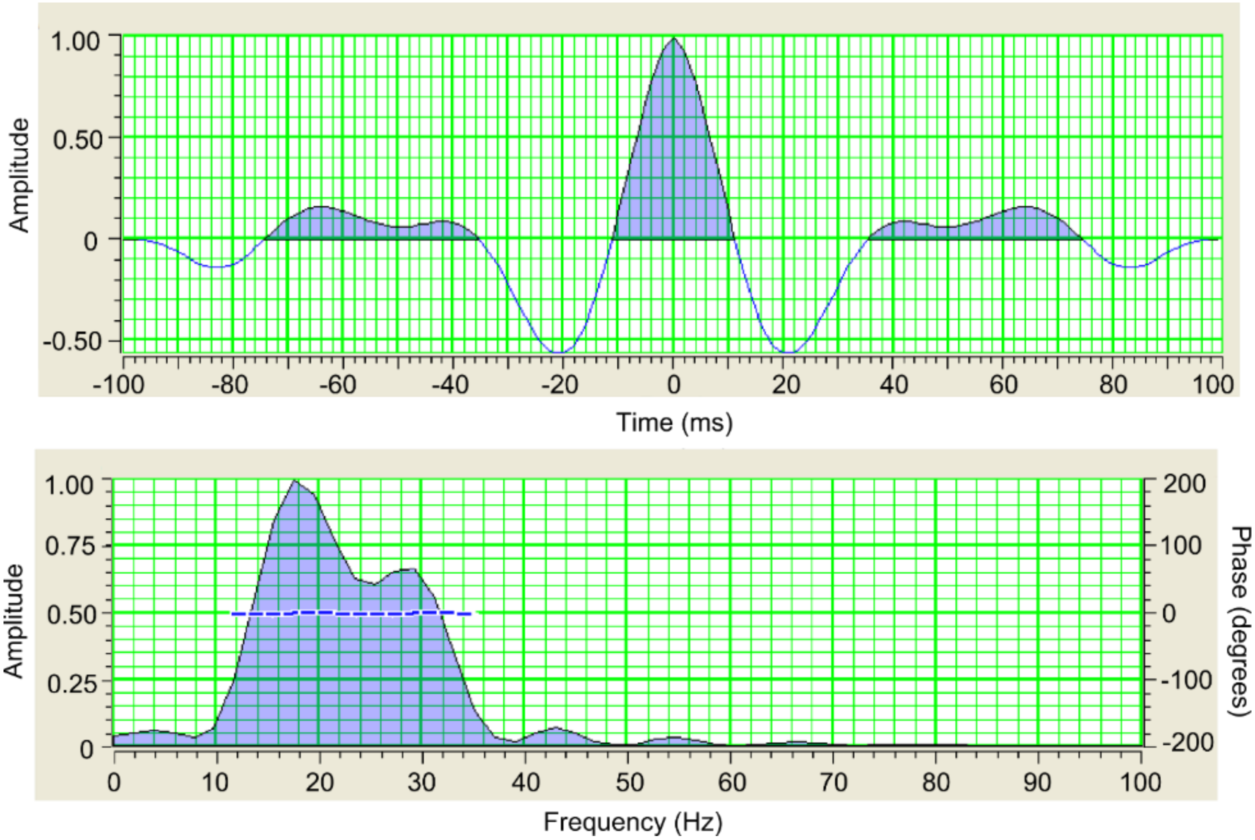

Figure 5.5. Wavelet P-SV Statistical estimated from a time window of 1000 – 1800 ms. The frequency content of the P-SV data is approximately half that of the P-P data.

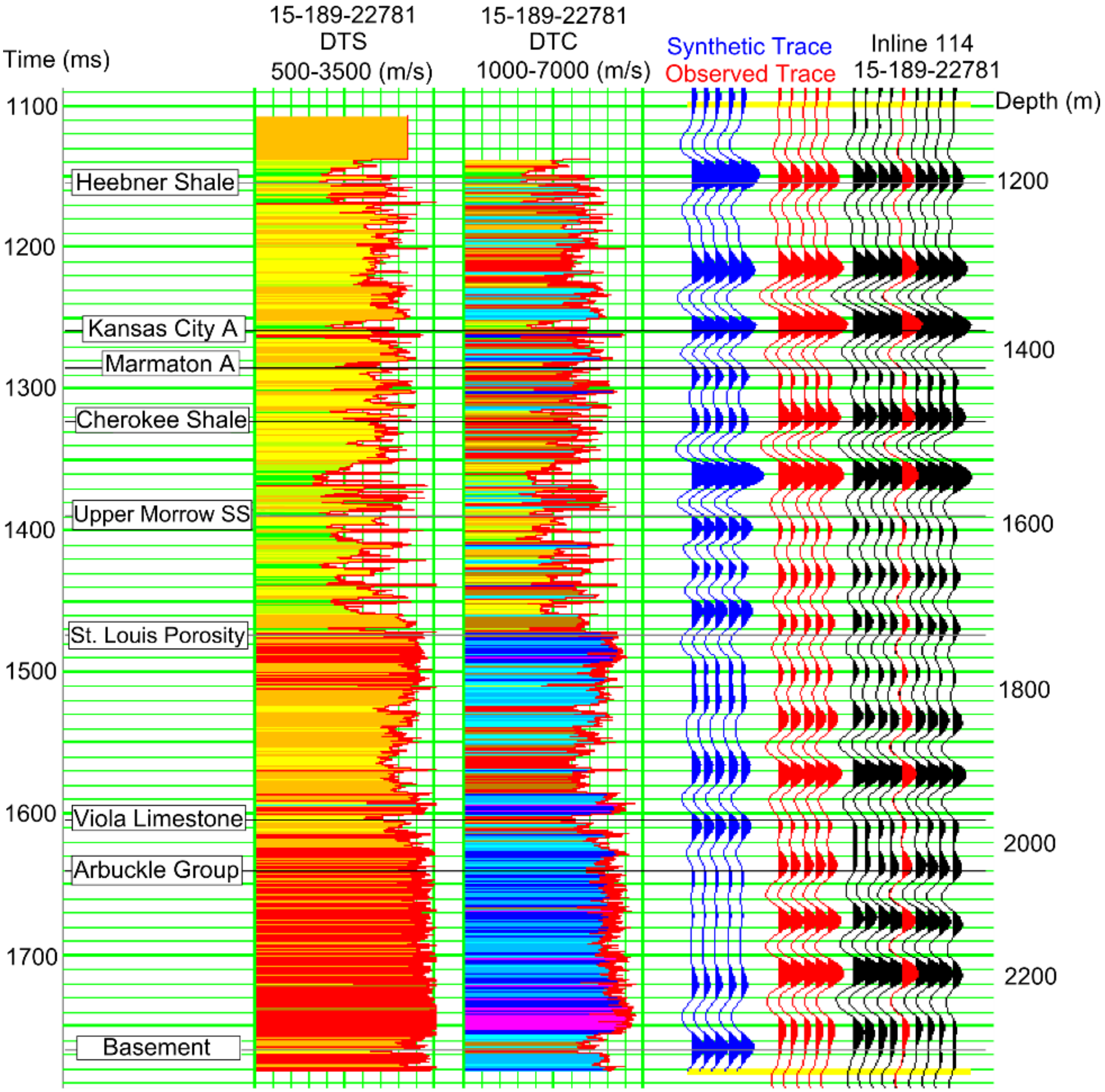

Figure 5.6. P-SV well-to-seismic tie. Correlation coefficient = 0.84 (1100-1400 ms).

5.4 Stratigraphic and structural interpretation

Six regional horizons corresponding stratigraphically to the tops of the Shawnee Group, Kansas City Group, Cherokee Group, Morrow Group, Viola Formation and Proterozoic basement were picked across the P-P volume using IHS Kingdom software (Figure 5.7). No major faulting is evident in the seismic data with the exception of a possible basement fault trending SW-NE in the northwestern corner of the Cutter 3D-3C survey area (Figure 5.8). Circular features, characteristic of karst (Brown, 2011), are visible in time slices as high as 810 ms and remain clearly visible down to approximately 930 ms (Figure 5.9). The karst features follow a linear SW-NE trend. This linear trend may be related to faulting or fracturing that created a preferred fluid pathway. Associated karst collapse features are visible on seismic profiles from the Kansas City horizon to the Viola horizon. The karst collapse features appear to be a caused by dissolution within the Viola Limestone or the Arbuckle Group. The Chester incised valley is a prominent feature in the seismic data and is visible in time slices from approximately 920 ms down to the basement (Figure 5.10).

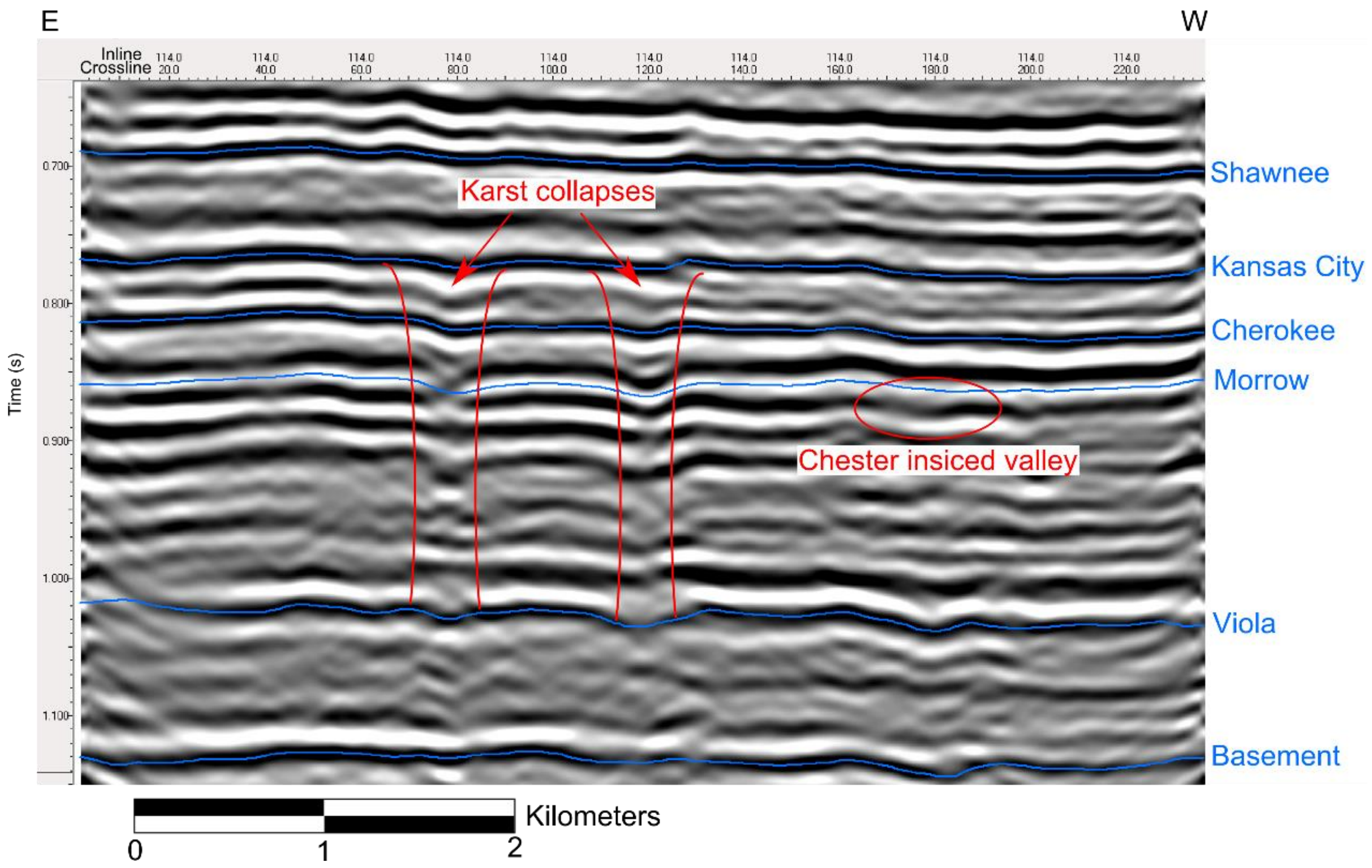

Figure 5.7. P-P inline 114 showing interpreted horizons and karst collapse features.

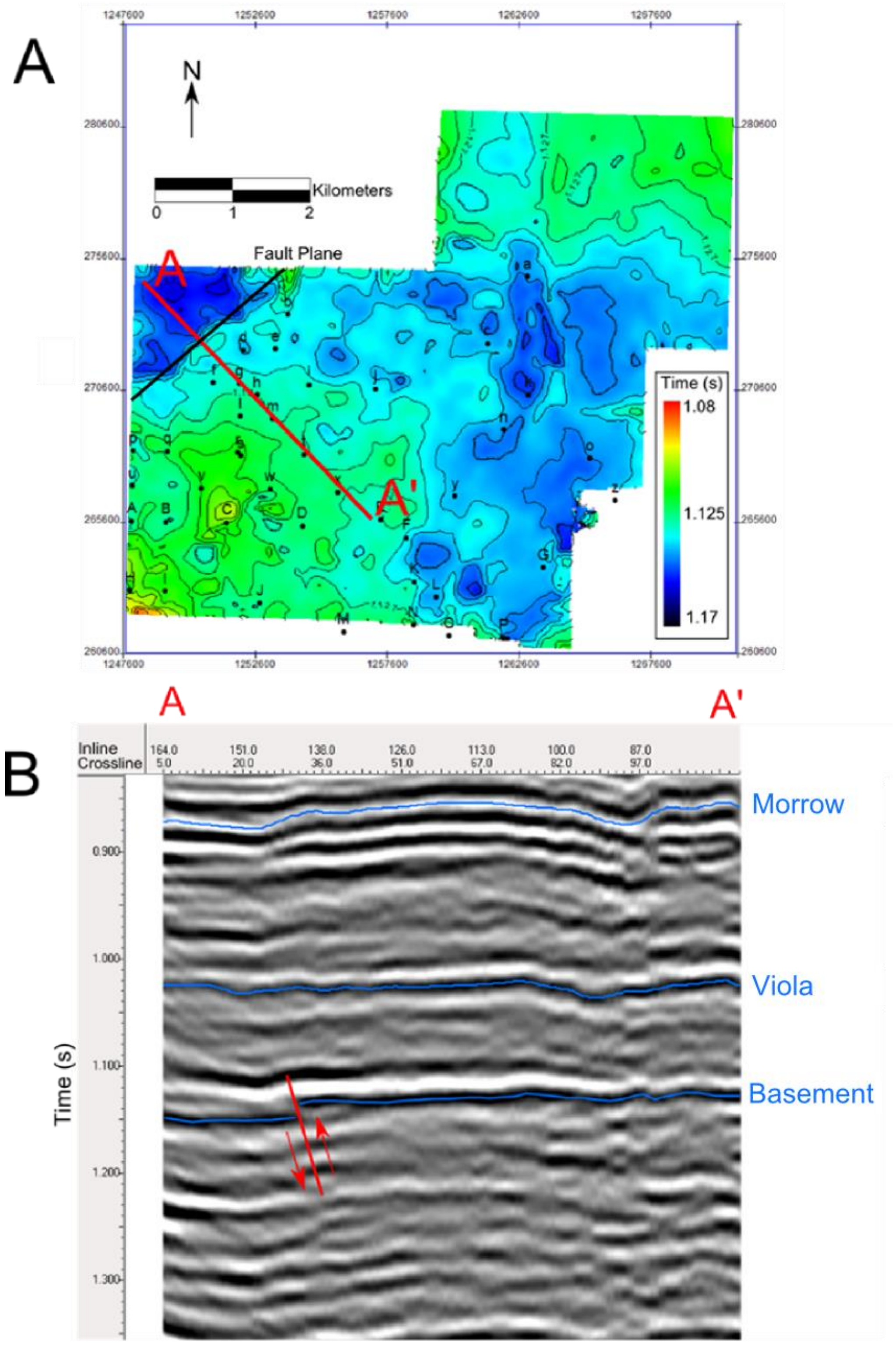

Figure 5.8. (A) Time-structure map of basement horizon with cross section A-A' oriented perpendicular to interpreted fault plane. The black line indicates the interpreted fault plane. (B) P-P seismic cross section A-A' showing interpreted fault.

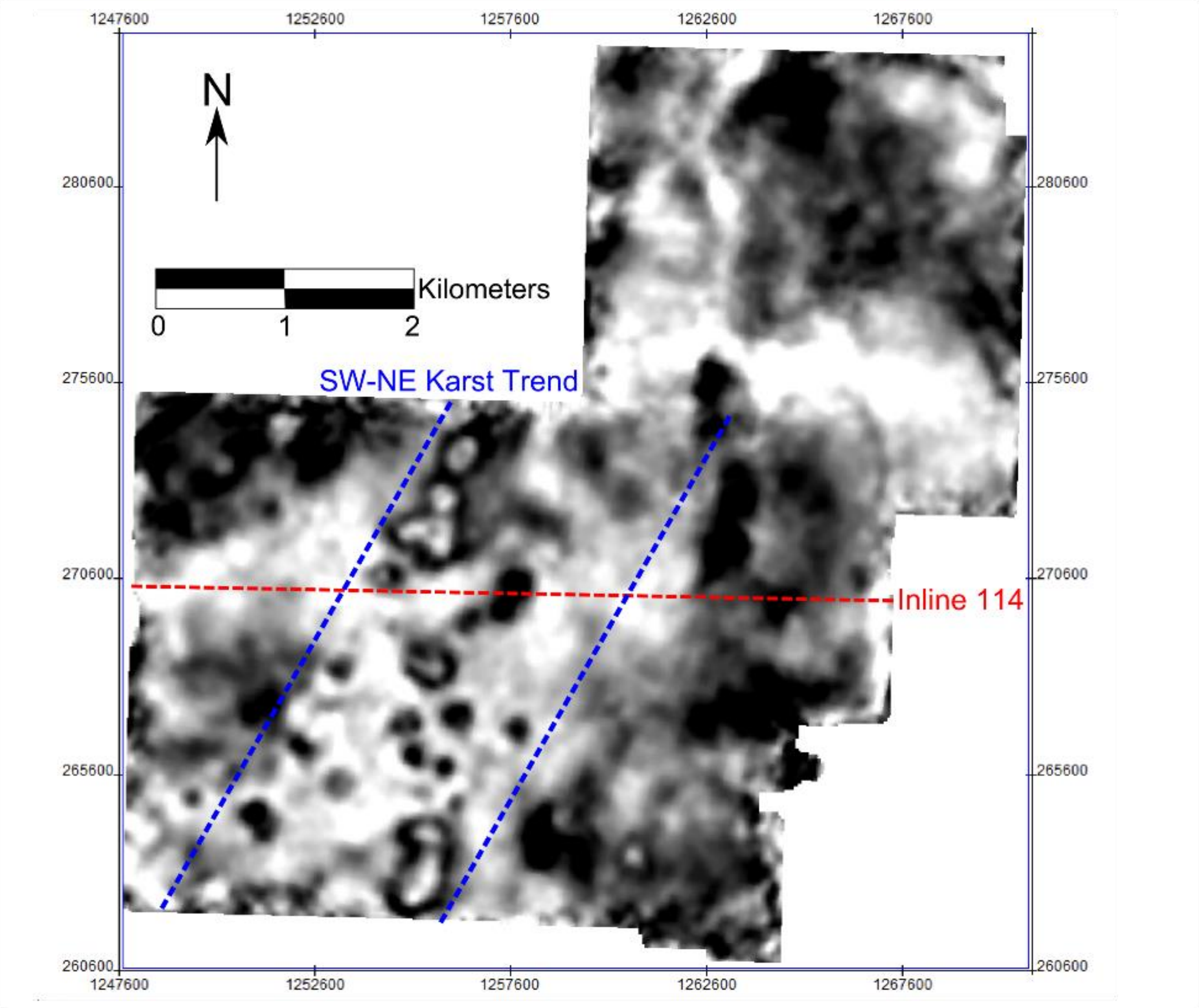

Figure 5.9. P-P time slice at 856 ms showing interpreted karst features. The red dotted line indicates inline 114. The blue dotted line indicates the SW-NE trend. The circular features located between the dotted blue lines are interpreted as karst.

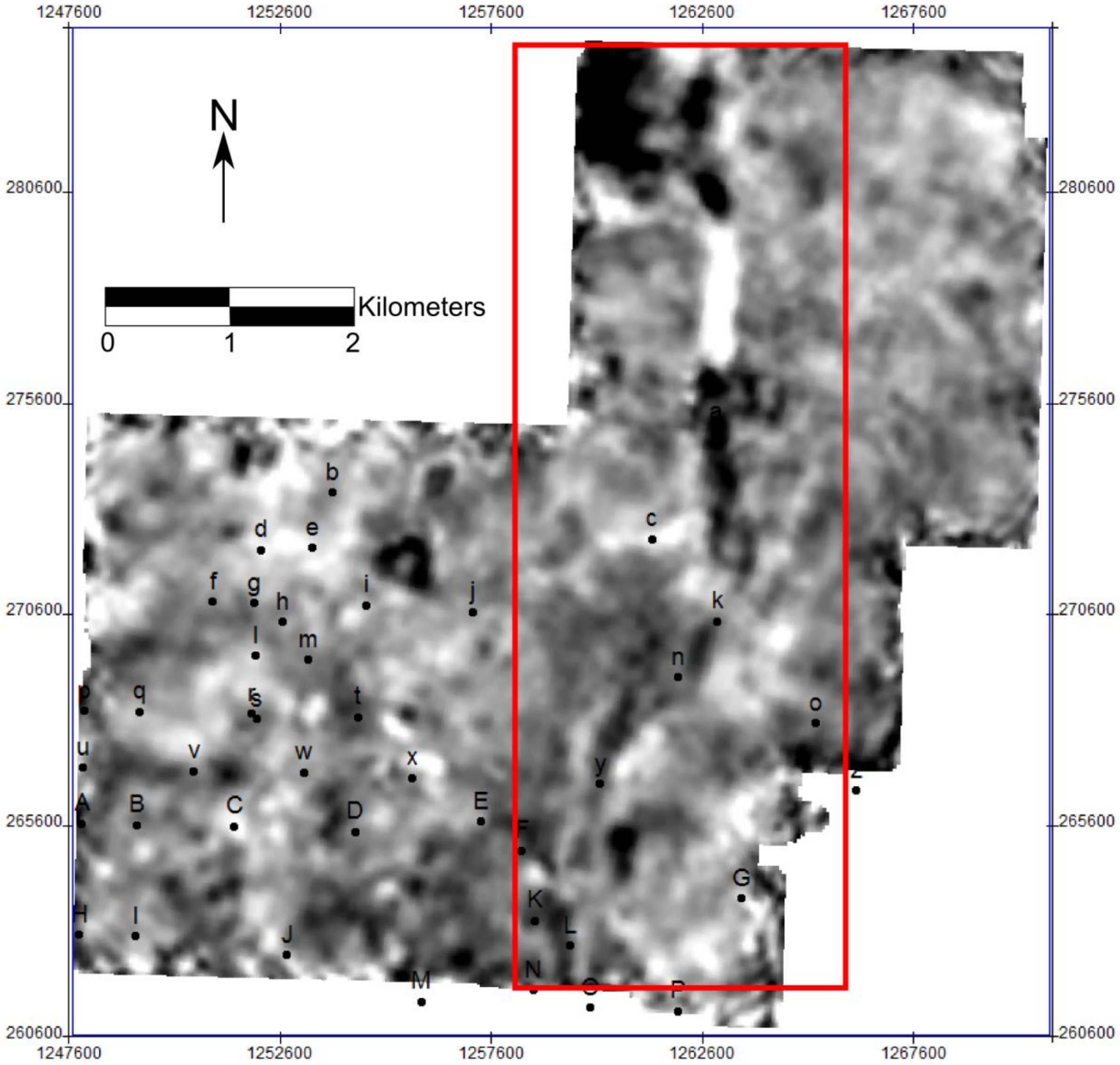

Figure 5.10. Time slice at 936 ms. Chester incised valley is located inside the red box. Dots indicate well locations. Letters indicate wells in Table 3.1.

Chapter 6: Upper Morrow Sandstone methods and results

6.1 Well correlations

At Cutter Field, the UMS is located at a depth of approximately 1600 m. Well log data from well 15-189-22781 shows the UMS to have an average P wave velocity of 4180 m/s, average S wave velocity of 2540 m/s, average density of 2.4 g/cc, and average porosity of 18%.

Well 15-189-22781 was used as the type log for correlating the UMS across additional wells in the Cutter 3D-3C survey area. Correlations were primarily based on the characteristic gamma ray motif (seen in Figure 6.1) and the characteristic P wave sonic velocity of 4180 m/s. Top and base of the UMS were correlated across 17 wells and determined to be absent in 25 wells within the Cutter 3D-3C survey area (Figures 6.2 and 6.3). Top A represents a laterally extensive shale layer that overlies the UMS and was picked as a reference top for wells in which the UMS is interpreted to be absent.

Fifteen of the 17 wells in which the UMS was correlated appear within a single UMS body located on the western side of the survey area. The remaining two wells are located on the eastern side of the survey area. They do not appear to be connected to the larger body on the western side of the survey because the UMS is absent at all well locations surrounding the two wells in question. It is unclear if the interval identified in these two wells is actually part of the UMS member. The well log correlations were used to construct an isopach map of the large UMS body (Figure 6.4).

The minimum resolvable thickness of the UMS, as determined by the 1/4 λ resolution limit, is ~23 m for the P-P data and ~33 m for the P-SV data. Resolution calculations were made using velocity data from well logs and wavelet periods found in Chapter 5. The apparent velocity, v_a, of the P-SV data was calculated to be 3160 m/s. Calculations are shown in Eq. (6.1 – 6.3):

$$\frac{\lambda_{P-P}}{4} = \frac{\left(4180\ \frac{\mathrm{m}}{\mathrm{s}}\right)(0.022\ \mathrm{s})}{4} \sim 23\ \mathrm{m}\,, \tag{6.1}$$

$$v_a = \frac{2}{\frac{1}{4180\ \mathrm{m/s}} + \frac{1}{2540\ \mathrm{m/s}}} \sim 3160\ \frac{\mathrm{m}}{\mathrm{s}}\,, \tag{6.2}$$

$$\frac{\lambda_{P-SV}}{4} = \frac{\left(3160\,\frac{\mathrm{m}}{\mathrm{s}}\right)(0.042\ \mathrm{s})}{4} \sim 33\ \mathrm{m}\,. \tag{6.3}$$

A maximum UMS thickness of 11.3 m, in well 15-189-2002, equates to ~1/8 λ for the P-P data and ~1/12 λ for the P-SV data in terms of seismic wavelength. The average UMS thickness of the 15 wells within the large body is 7.5 m.

Therefore, UMS thickness at Cutter Field is below the Rayleigh criterion of both the P-P and P-SV volumes and can only be inferred, in theory, through tuning effects. In the following sections, tuning effects are modeled and the results are compared to attributes extracted from the P-P and P-SV volumes

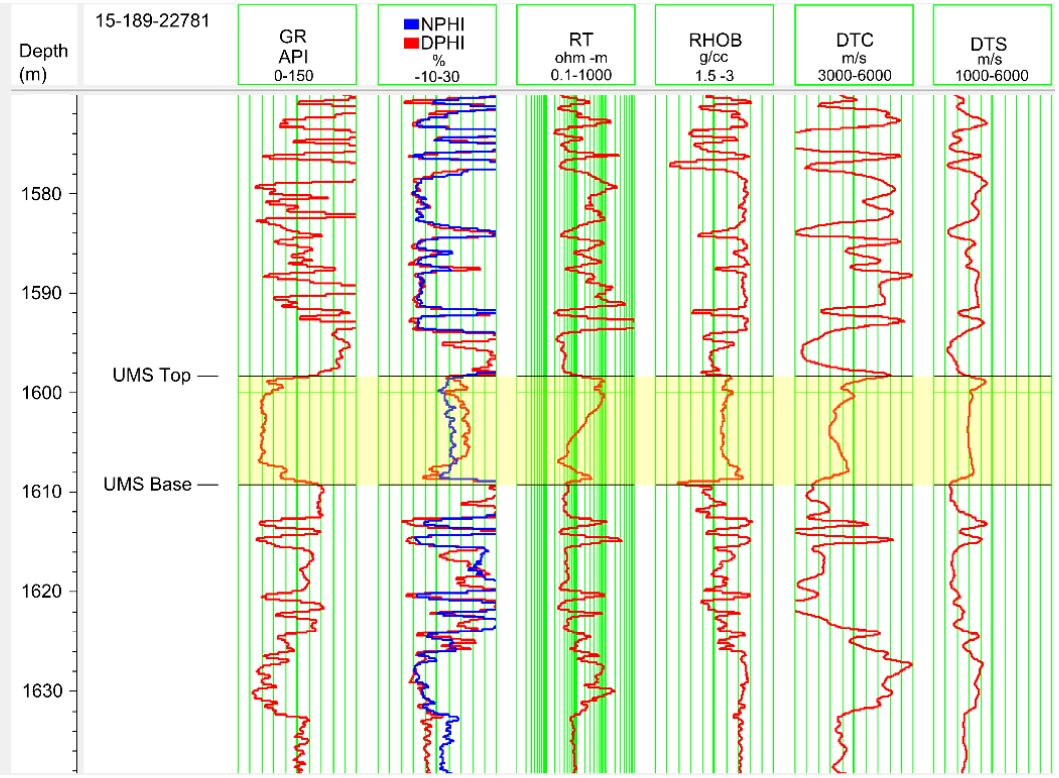

Figure 6.1. Well-log response of the UMS reservoir at Cutter Field.

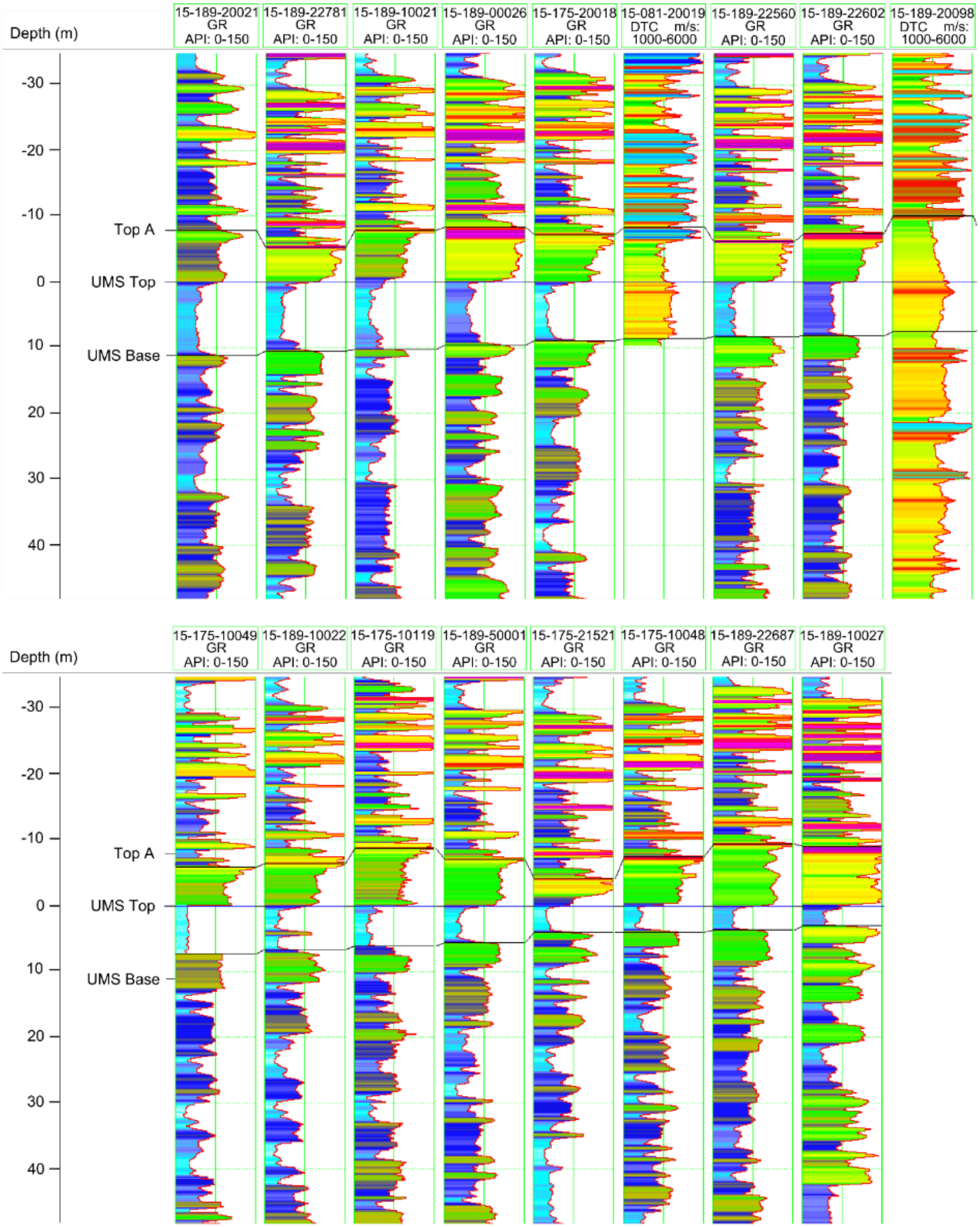

Figure 6.2. Gamma ray correlations of the UMS reservoir, datumed on the top of the UMS. Sonic logs are shown for wells that lacked gamma ray logs. Depth is relative to the top of the UMS. The UMS is identifiable by the characteristic motif of the gamma ray log and by a P wave velocity of 4180 m/s.

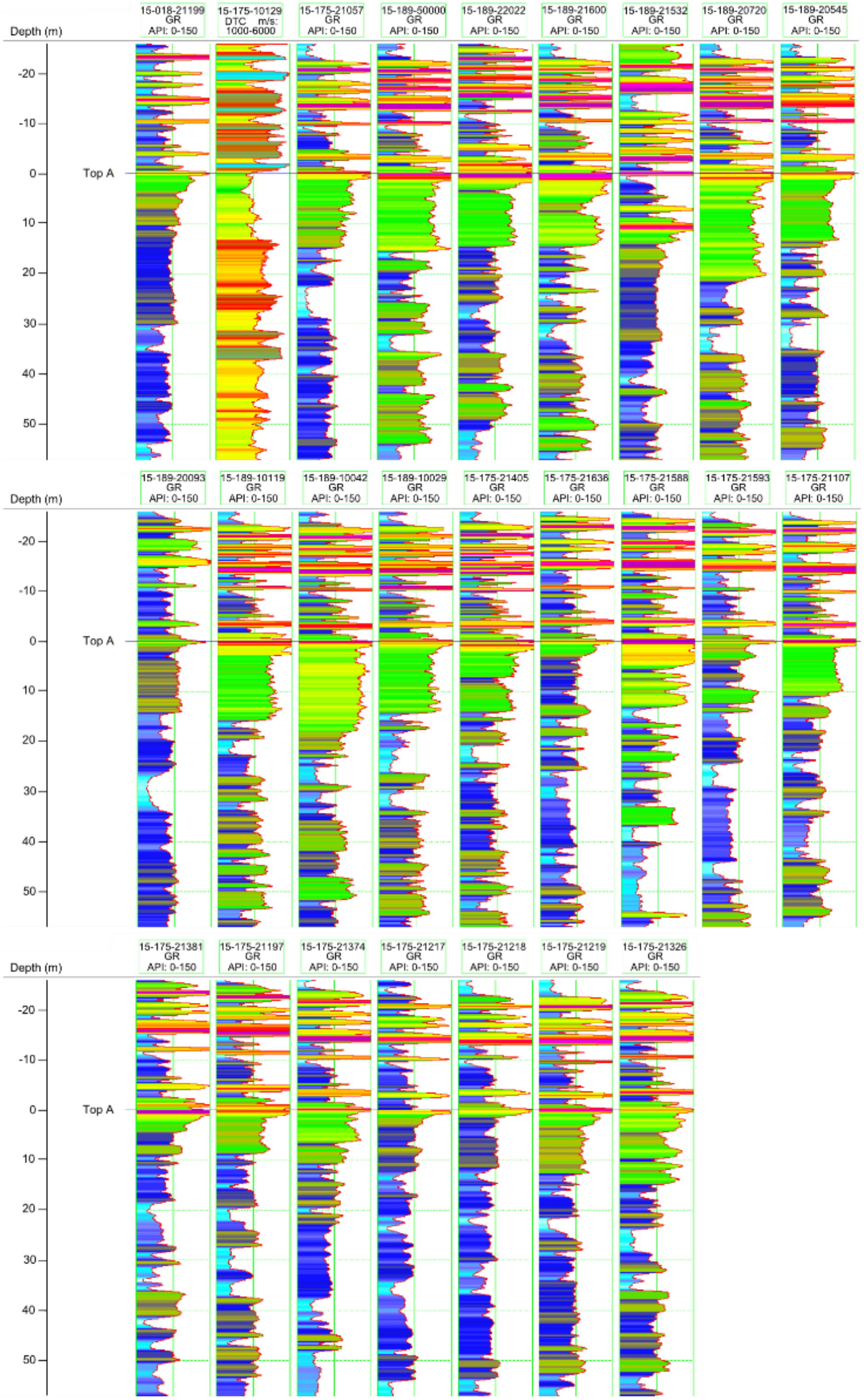

Figure 6.3. Gamma ray logs of wells in which the UMS was interpreted to be absent, datumed on Top A. Sonic log are shows for wells that lacked gamma ray logs. Depth is relative to Top A. The logs do not contain the gamma ray motif and average P wave velocity of 4180 m/s that are characteristic of the UMS.

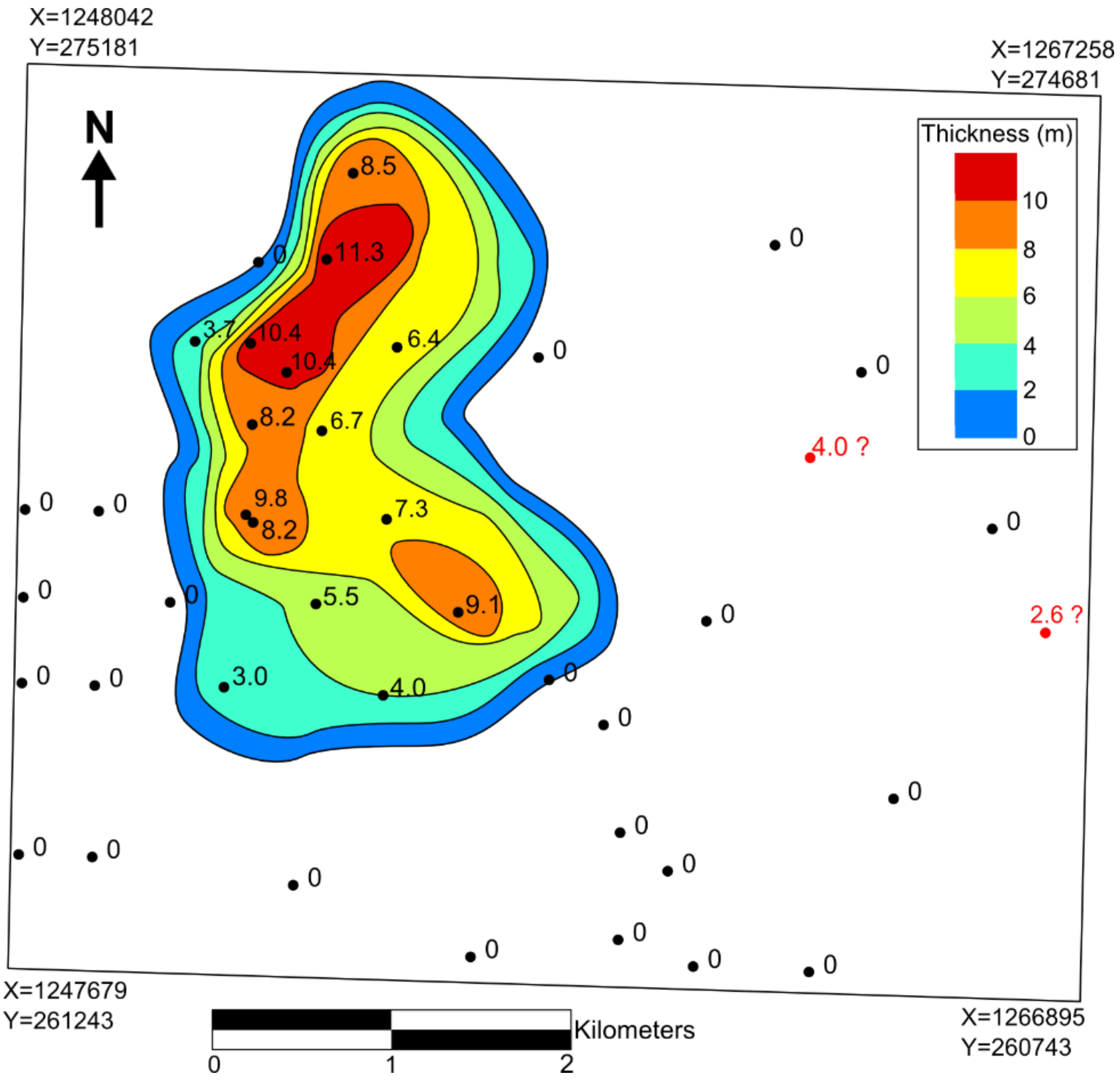

Figure 6.4. Isopach of the UMS reservoir constructed from well correlations. Dots indicate well locations and annotations indicate UMS thickness in meters. Wells with uncertain correlations are shown in red.

6.2 AVO modeling

The UMS at Cutter Field shows a distinct contrast with surrounding shale in terms of both P- impedance and S-impedance (Figure 6.5). The top interface of the UMS exhibits a 20% difference in P-impedance and a 33% difference in S-impedance with the overlying shale. For the top interface, the change in P-impedance is more gradational than the change in S-impedance. The bottom interface exhibits a 26% percent difference in P-impedance and a 38% increase in S-impedance with the underlying shale (Figure 6.5). Sharp bottom interfaces are evident for both P-impedance and S-impedance. Amplitude versus offset (AVO) modeling was performed to compare reflection coefficients of P-P and P-SV wave modes.

Reflection coefficients for the top and bottom interfaces of the UMS were modeled as a function of incidence angle using Eq. (2.4). Calculations were made for an incidence angle range of 0 – 45 degrees. Each interface was modeled as a half-space. The modeling parameters and results (shown in Figure 6.6) show a maximum P-P reflection coefficient magnitude of 0.10 at zero degrees of incidence. The maximum P-SV reflection coefficient magnitude of 0.13 occurs at 30 degrees of incidence. For the top interface, the magnitude of the P-SV reflection coefficients exceeds that of the P-P reflection coefficients for incidence angles greater than 14 degrees.

Modeling of the bottom interface shows a maximum P-P reflection coefficient magnitude of 0.13 at zero degrees of incidence. The maximum P-SV reflection coefficient magnitude of 0.15 occurs at 31 degrees of incidence. For the bottom interface, the magnitude of the P-SV reflection coefficients exceeds that of P-P reflection coefficients for incidence angles greater than 15 degrees.

The AVO modeling demonstrates that P-SV reflection magnitudes can exceed P-P reflection magnitudes if survey offsets are sufficiently long. In the next section, ray tracing illustrates the maximum angle of incidence of the P-SV data from the Cutter 3D-3C survey.

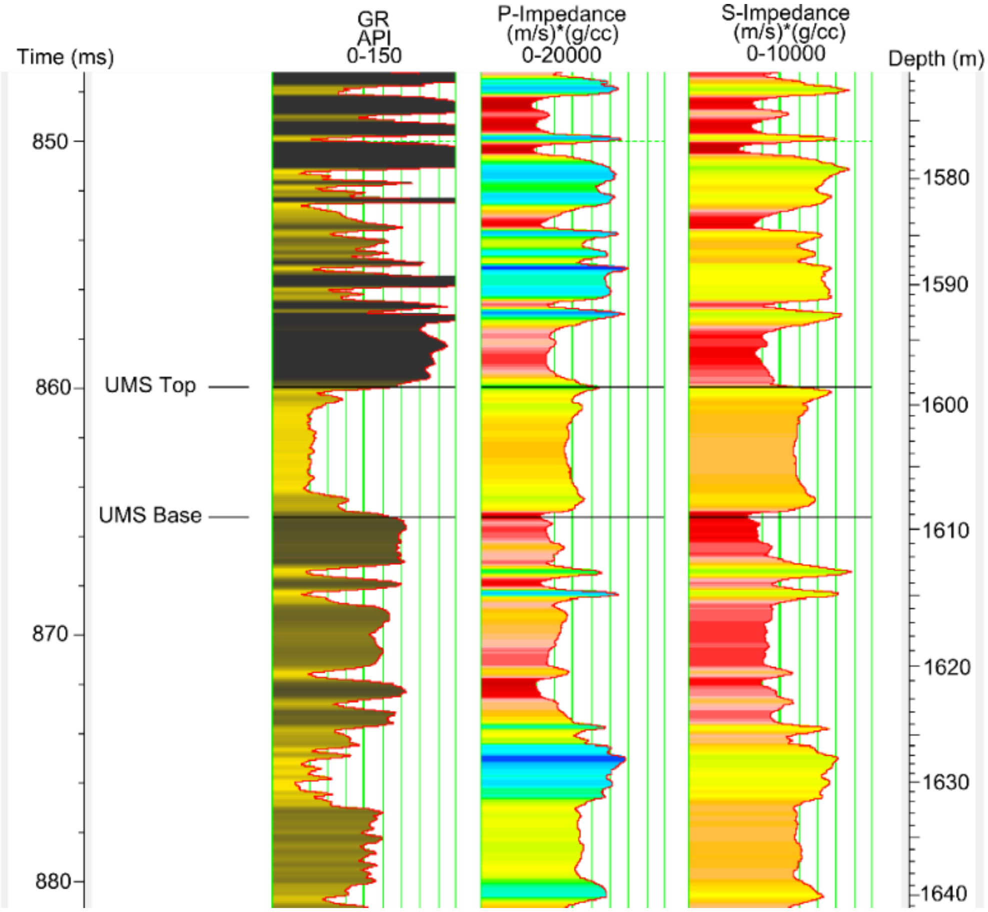

Figure 6.5. Comparison of P-impedance and S-impedance contrast between the UMS and encasing shale. Both P-impedance and S-impedance of the UMS are higher than that of the surrounding shale.

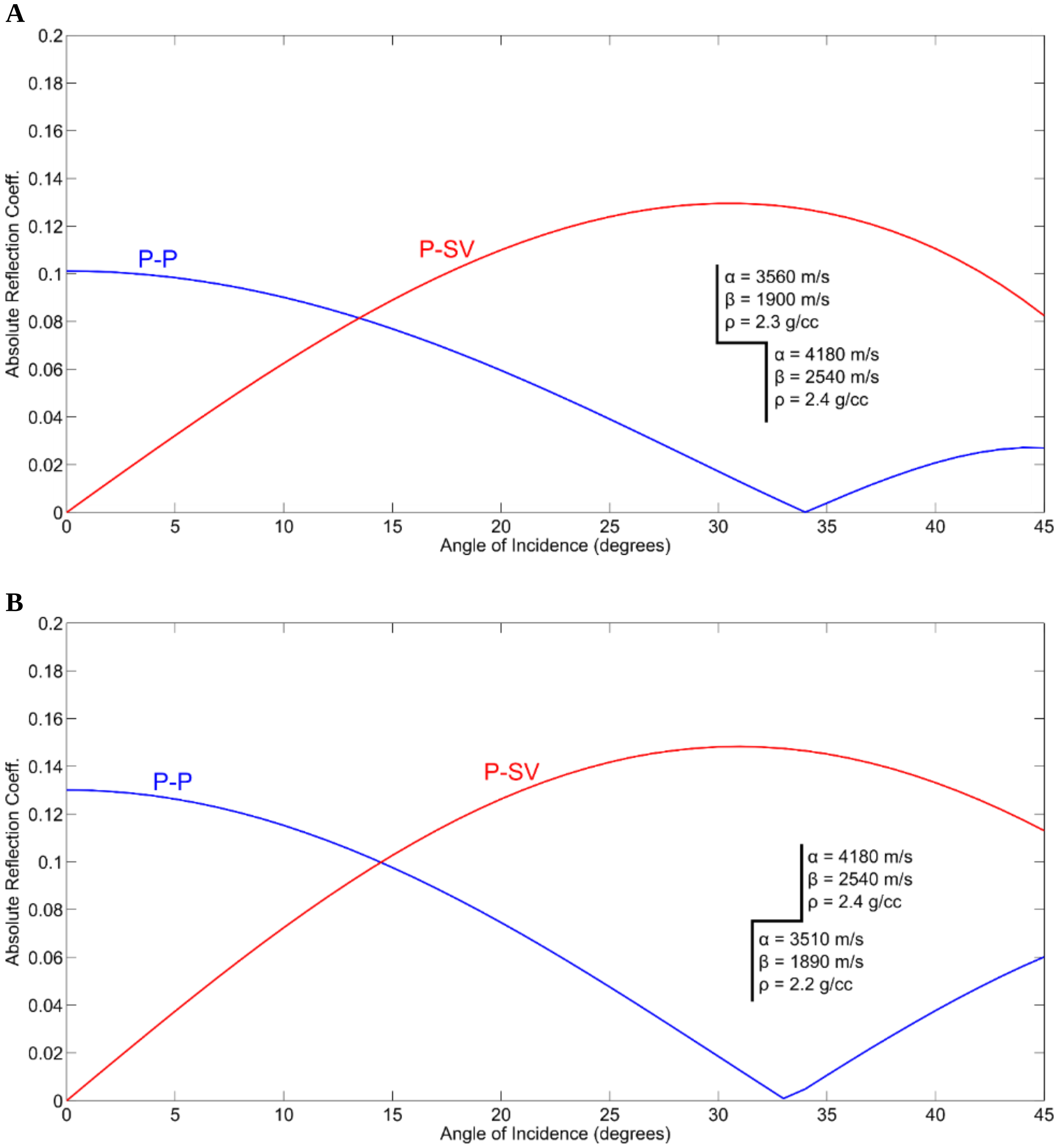

Figure 6.6. (A) AVO modeling of the top interface of the UMS. (B) AVO modeling of the bottom interface of the UMS. P-SV reflection coefficient magnitudes exceed P-P reflection coefficient magnitudes for incidence angles greater than 15 degrees.

6.3 Ray trace modeling

Ray tracing was completed on a four-layer velocity model to determine if the maximum offsets of the Cutter 3D-3C survey were sufficient for obtaining P-SV reflections of greater magnitude than P-P reflections. The velocity model was constructed from sonic logs in wells 15-189-22781 and 15-189-00026. Ray tracing was completed using Snell's law (Eq. 2.5). At the maximum offset of 1056 m, the ray trace model shows a P-SV incidence angle of 28 degrees (Figure 6.7). This angle corresponds to a modeled reflection coefficient magnitude 0.13 for the top interface and 0.14 for the bottom interface. A finer-scale velocity model could not be constructed because no sonic log data includes the upper 520 m of the stratigraphic column in the survey area. The ray trace modeling demonstrates that the maximum offset of the Cutter 3D-3C survey is sufficiently long to obtain P-SV reflection magnitudes that exceed P-P reflection magnitudes.

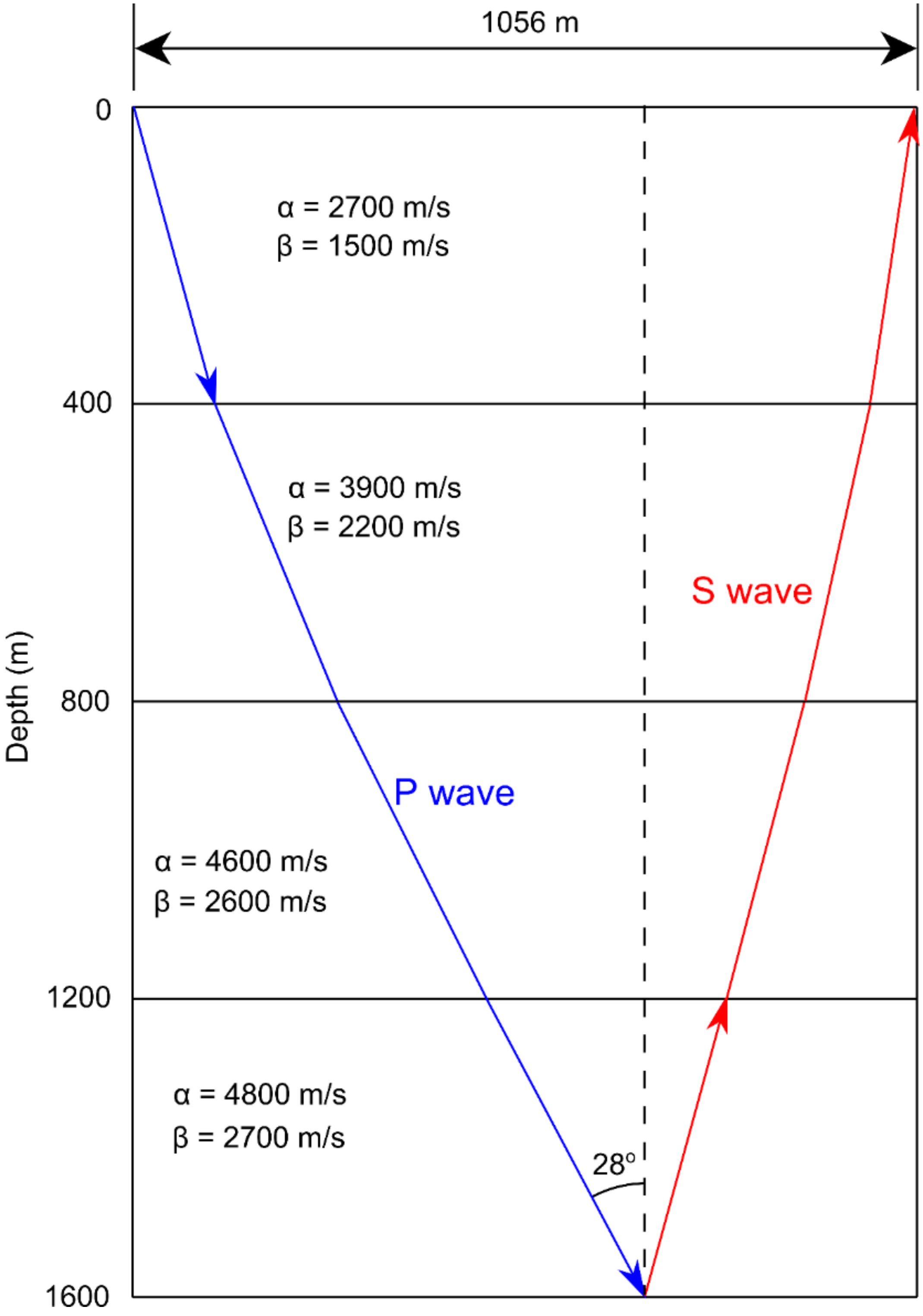

Figure 6.7. Ray tracing of P-SV reflection at maximum offset of 1056 m. Incidence angle at maximum offset is expected to be ~ 28 degrees.

6.4 Wedge modeling

To examine the effect of UMS thickness changes on amplitude, wedge modeling was conducted using the Hampson-Russell Geoview software package. A P-impedance wedge model was generated by stretching the thickness of the UMS interval in the sonic and density logs from the “base case” of well 15-189-22781. The thickness of the UMS interval was varied from 0 to 30 m with a step of 1 m. A P-P zero offset synthetic trace was calculated for each thickness using a 42 Hz, 90 degree phase Ricker wavelet (Figure 6.8). On the synthetic seismogram, the trough and peak around the UMS interval were picked and termed “UMS1” and “UMS2” respectively.

The amplitudes of UMS1 and UMS2 plotted as a function of thickness (Figure 6.9) reveal greater amplitude magnitudes are for horizon UMS2. Maximum amplitude magnitudes for both UMS1 and UMS2 are observed at a UMS thickness of 0 meters. Amplitudes of both horizons gradually decrease up to thicknesses of approximately 12 m and remain relatively constant for thicknesses of 12-30 m. The tuning response of the P-SV data is expected to be less pronounced because of its lower resolution in comparison to the P-P data.

RMS instantaneous frequency was computed for the interval between horizons UMS1 and UMS2 and plotted versus UMS thickness (Figure 6.10). For UMS thicknesses in the range of 0 – 14 m, instantaneous frequency decreases with increasing thickness. The development of the peak between horizons UMS1 and UMS2 produces several changes in the instantaneous frequency curve for UMS thicknesses in the range of 14 – 30 m. These changes are not of practical interest because UMS thickness does not exceed 14 m in the study area.

The key result from the wedge modeling is the prediction that amplitude magnitudes and instantaneous frequency will decrease with increasing UMS thickness. In the following section, attributes will be extracted from the P-P and P-SV volumes and compared to modeled results.

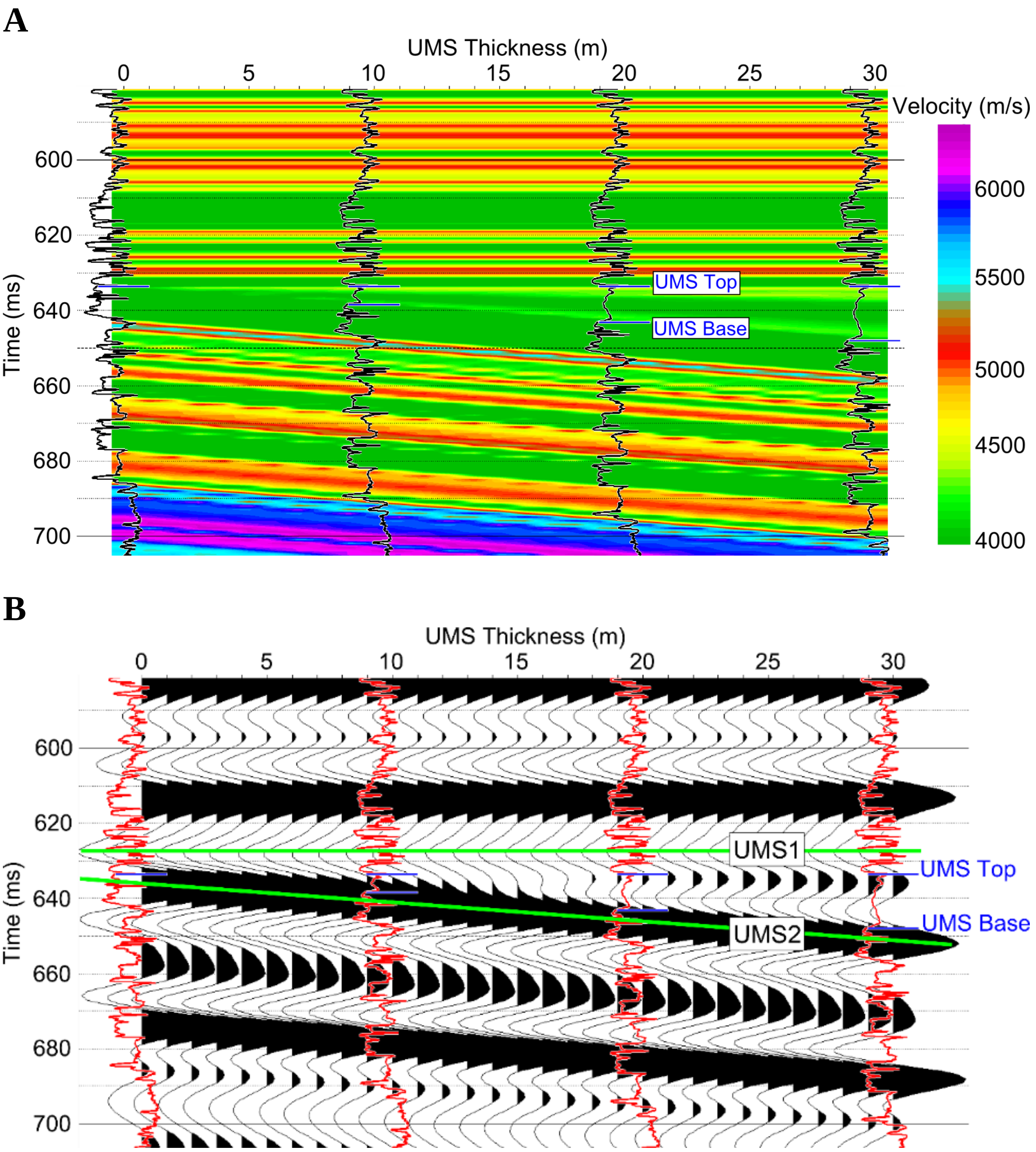

Figure 6.8. (A) Velocity wedge model generated with inserted sonic log curves. (B) Synthetic seismogram computed from velocity model with inserted sonic log curves and interpreted horizons UMS1 and UMS2.

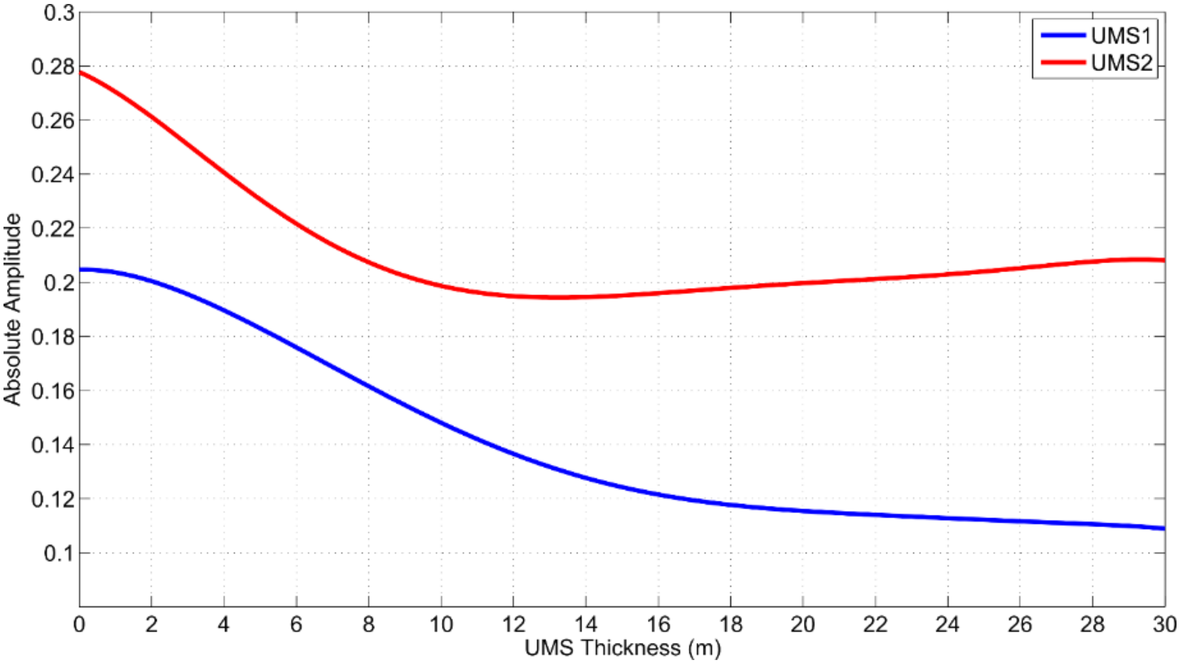

Figure 6.9. Amplitude magnitudes of horizons UMS1 and UMS2 as picked on the wedge model synthetic seismogram. Amplitude magnitudes of both horizons decrease with increasing UMS thickness.

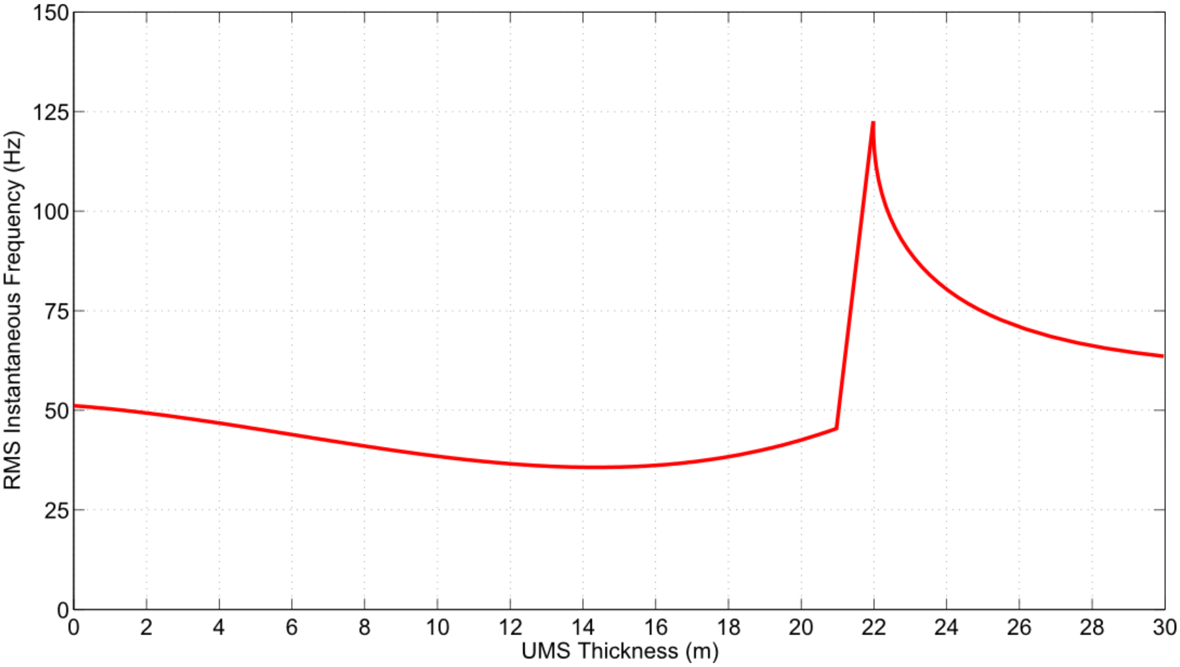

Figure 6.10. RMS instantaneous frequency computed between the interval of horizons UMS1 and UMS2 on the wedge model. RMS instantaneous frequency decreases with increasing thickness for UMS thicknesses ranging from 0 – 14 m.

6.5 Amplitude analysis

The wedge model results predict decreasing amplitude magnitudes of horizons UMS1 and UMS2 with increasing UMS thickness. To test this prediction, horizons UMS1 and UMS2 were picked on the P-P volume using IHS Kingdom software (Figure 6.11). A time-structure map of horizon UMS1 shows structural highs in the southwestern and northeastern corners of the survey area (shown in Figure 6.12). The UMS reservoir is partially located over the structural high in the in southwestern corner.

The predicted amplitude trend of decreasing amplitudes magnitudes with increasing UMS thickness not evident in the amplitude maps of horizon UMS1 or horizon UMS2 as picked on the P-P volume (Figure 6.13). Horizon UMS1 was also picked on the three P-SV volumes. The lower data quality exhibited in the P-SV data did not permit horizon UMS1 to be picked across the entire survey area. The quality of the P-SV data is deemed to be lower than that of the P-P data because P-SV reflections are less coherent than the corresponding P-P reflections. The reflection corresponding to horizon UMS2 was highly discontinuous on the P-SV data and was not picked. No amplitude trend associated with the UMS reservoir was discernible on the UMS1 amplitude map as picked on the P-SV data (Figure 6.14).

Further investigation of the UMS1 and UMS2 amplitudes was performed by extracting traces from 26 well locations. Wells located in low fold areas near the edge of the survey were excluded from the analysis. Representative traces for each well locations were generated by averaging a 3 x 3 grid of traces around each well location. Averaging was performed to reduce the effect of anomalous errors that may be present in individual traces. Horizons UMS1 and UMS2 were picked on the traces extracted from the P-P volume and horizon UMS1 was picked on the traces extracted from the three P-SV volumes. Amplitude magnitudes plotted versus

UMS thickness (Figures 6.15 and 6.16) reveal no discernible relationship between UMS thickness and amplitude magnitudes of the P-P or P-SV data.

No discernible relationship was evident between P-P or P-SV amplitudes and UMS thickness on horizons UMS1 and UMS2. Possible explanations for the lack of correlation are discussed in Section 6.6. The next section explores for correlations between windowed attributes and UMS thickness.

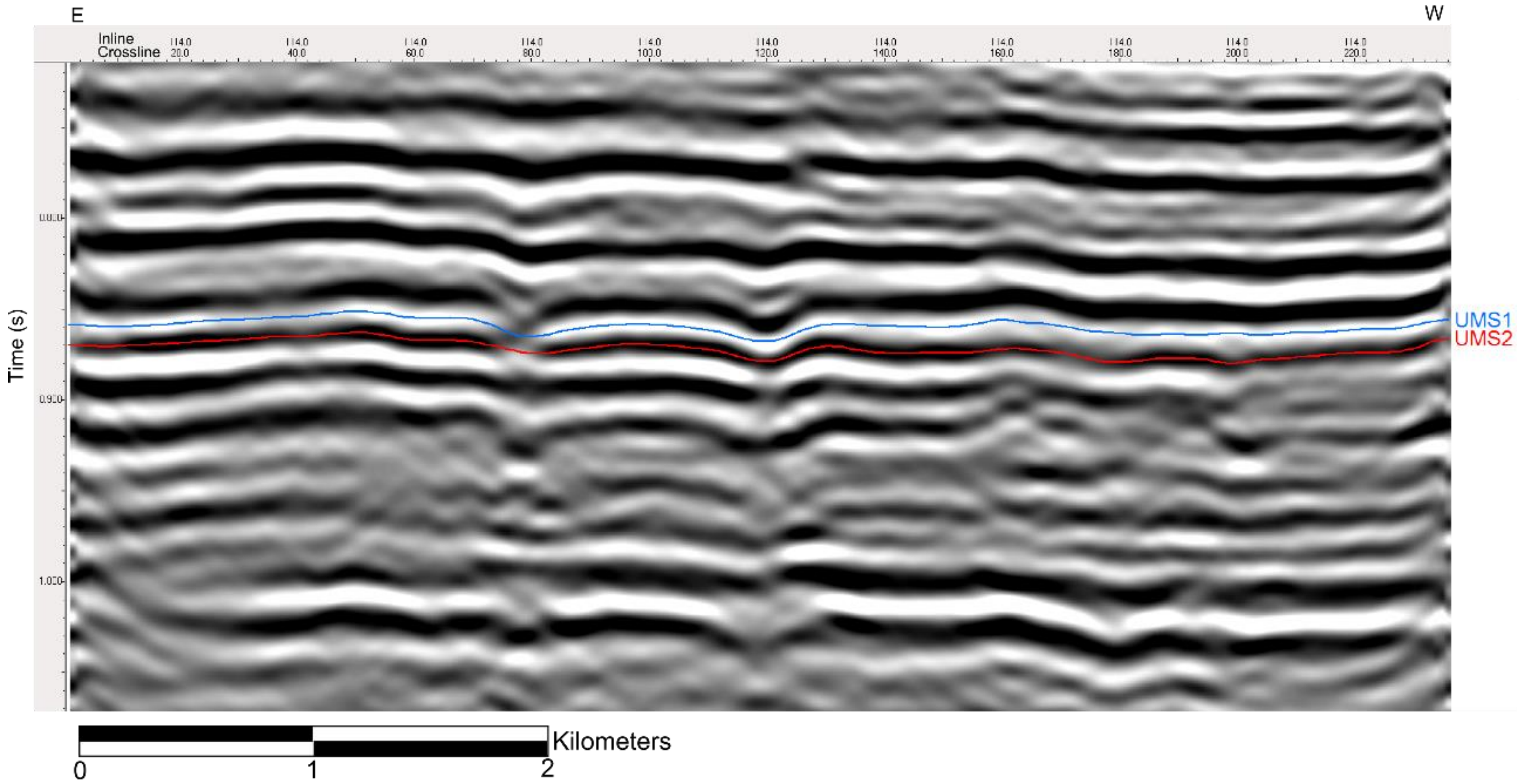

Figure 6.11. P-P profile of inline 114 showing picks of horizons UMS1 and UMS2.

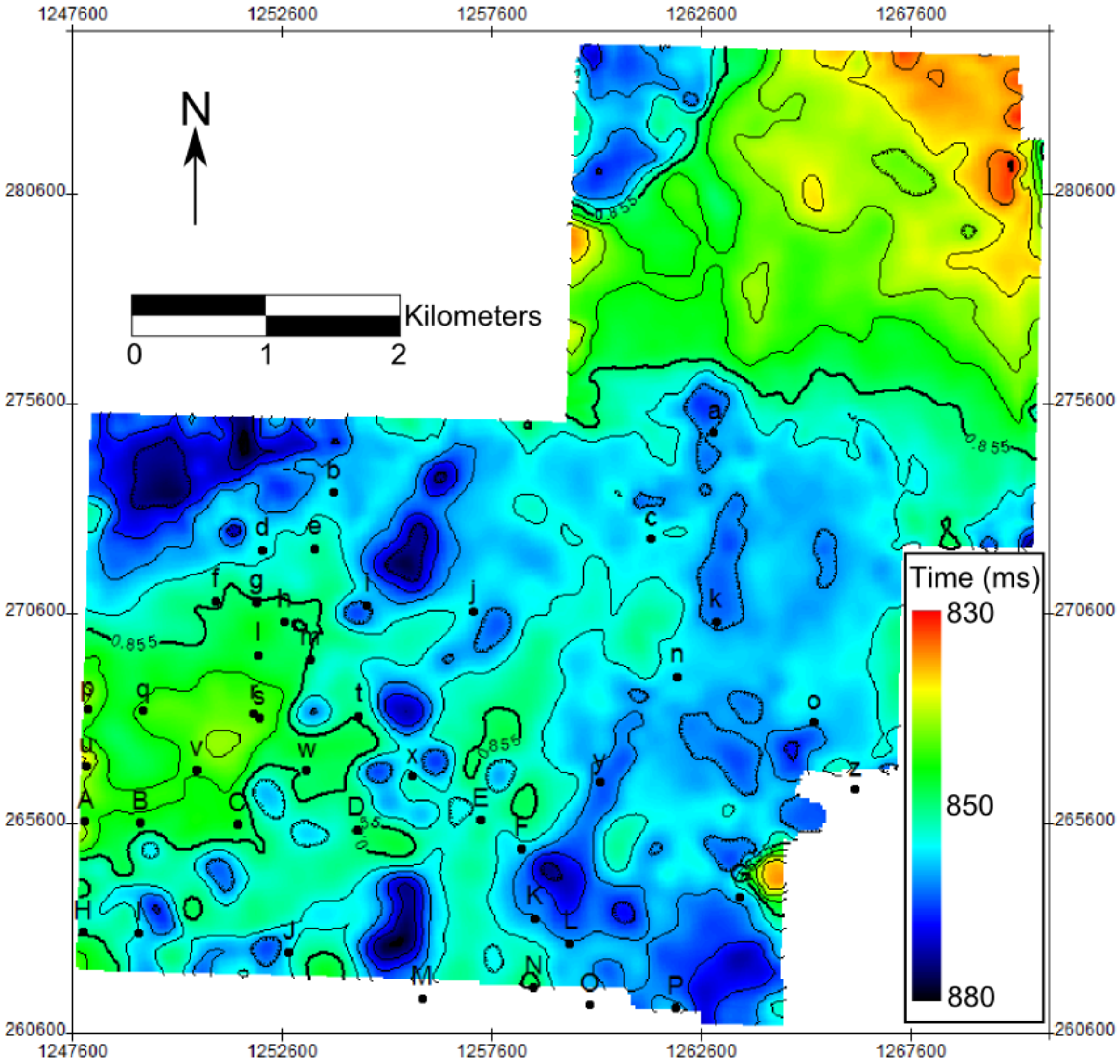

Figure 6.12. P-P time-structure map of horizon UMS1. Structural highs are present in the southwestern and northeastern corners of the survey area.

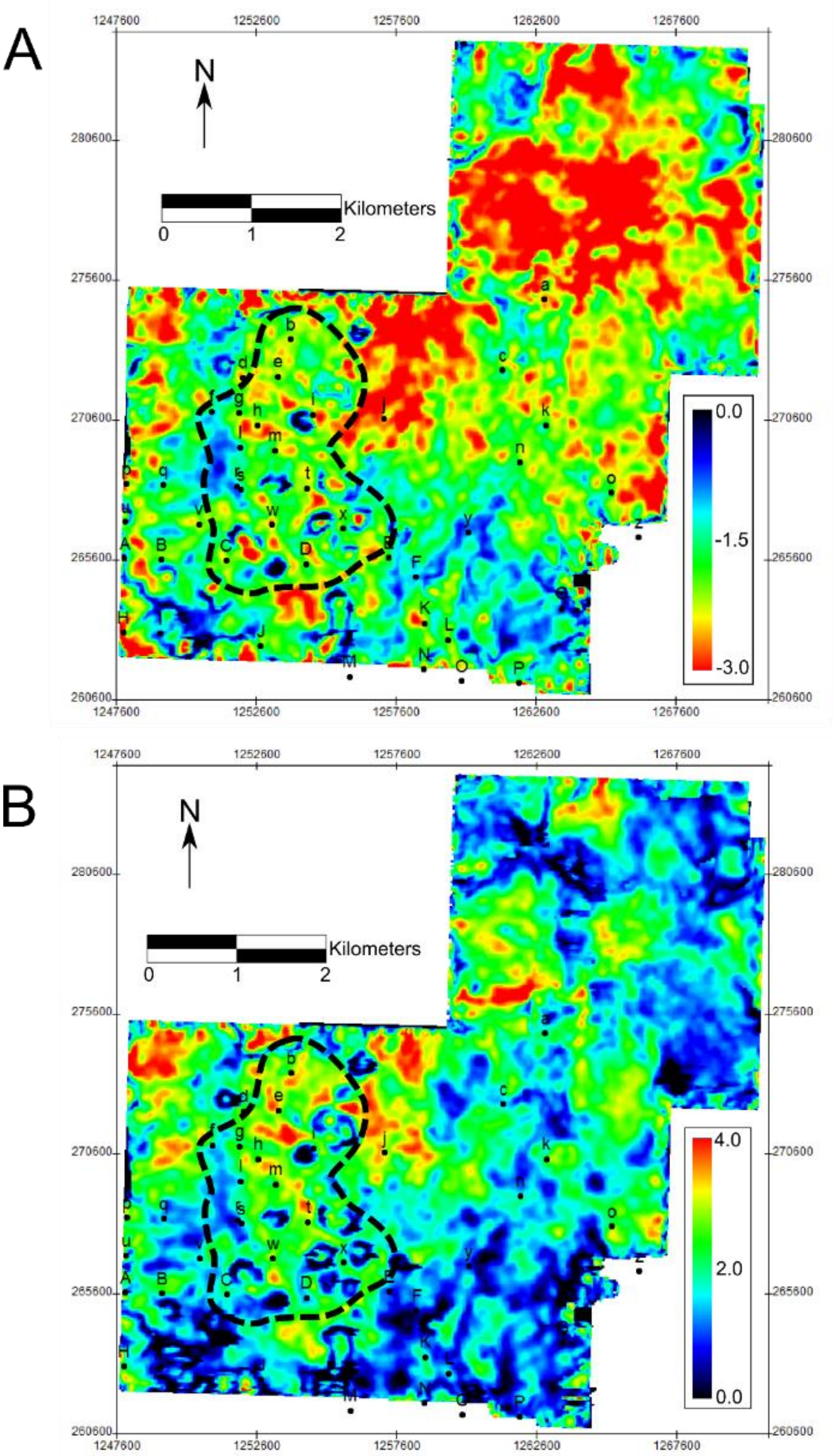

Figure 6.13. (A) P-P amplitude map of horizon UMS1. (B) P-P amplitude map of horizon UMS2. Boundary of the UMS reservoir, as determined by well data, indicated by dashed lines. P-P amplitudes do not delineate the UMS reservoir boundary.

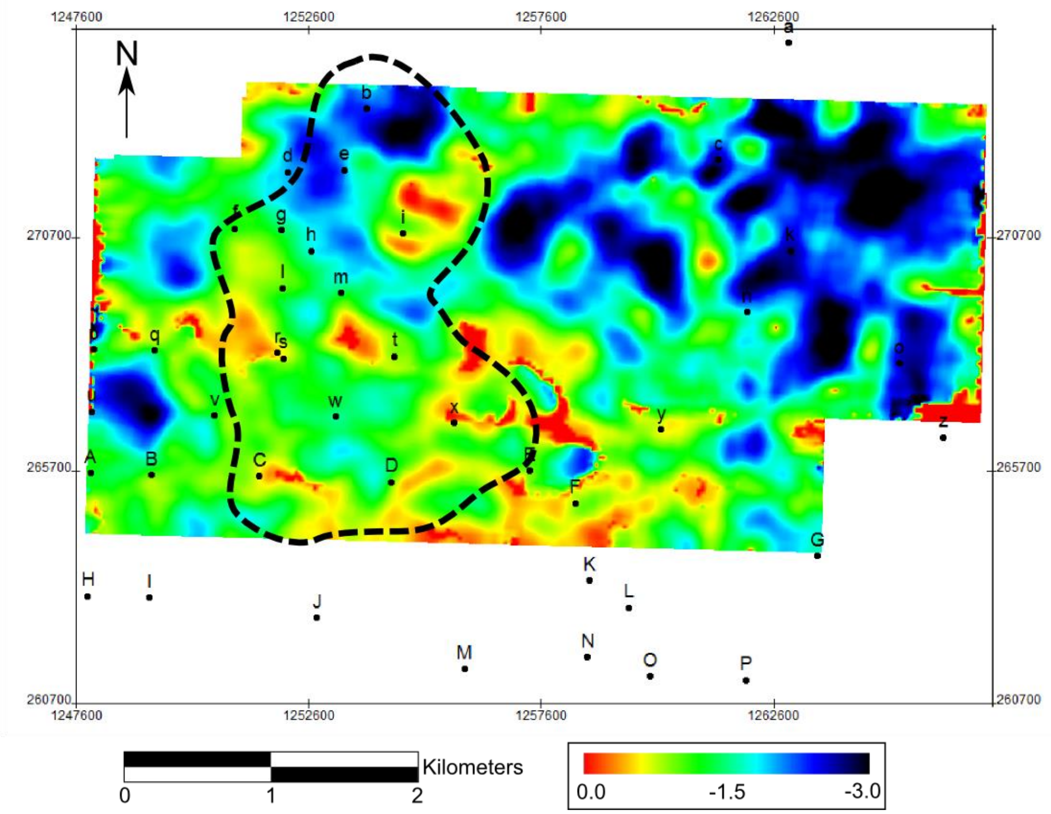

Figure 6.14. Amplitude map of horizon UMS1 as picked on the P-SV Fast volume. Similar results occur for P-SV Slow and P-SV Radial volumes. Boundary of the UMS reservoir, as determined by well data, indicated by dashed lines. P-SV amplitudes do not delineate the UMS reservoir boundary.

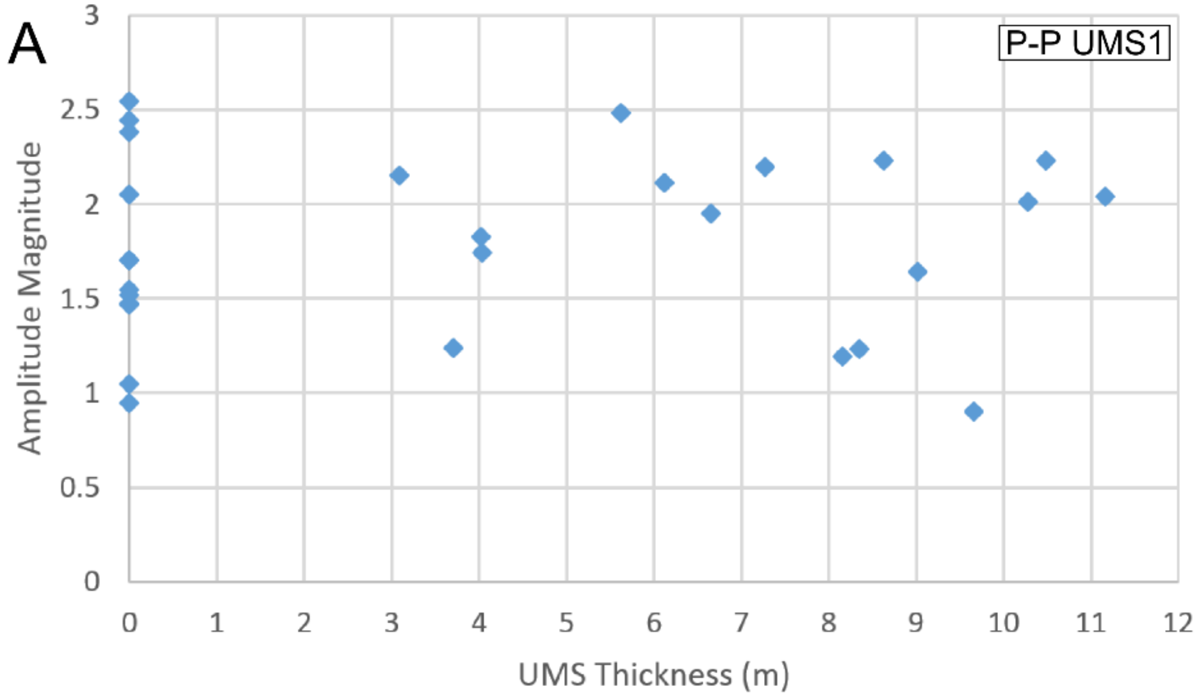

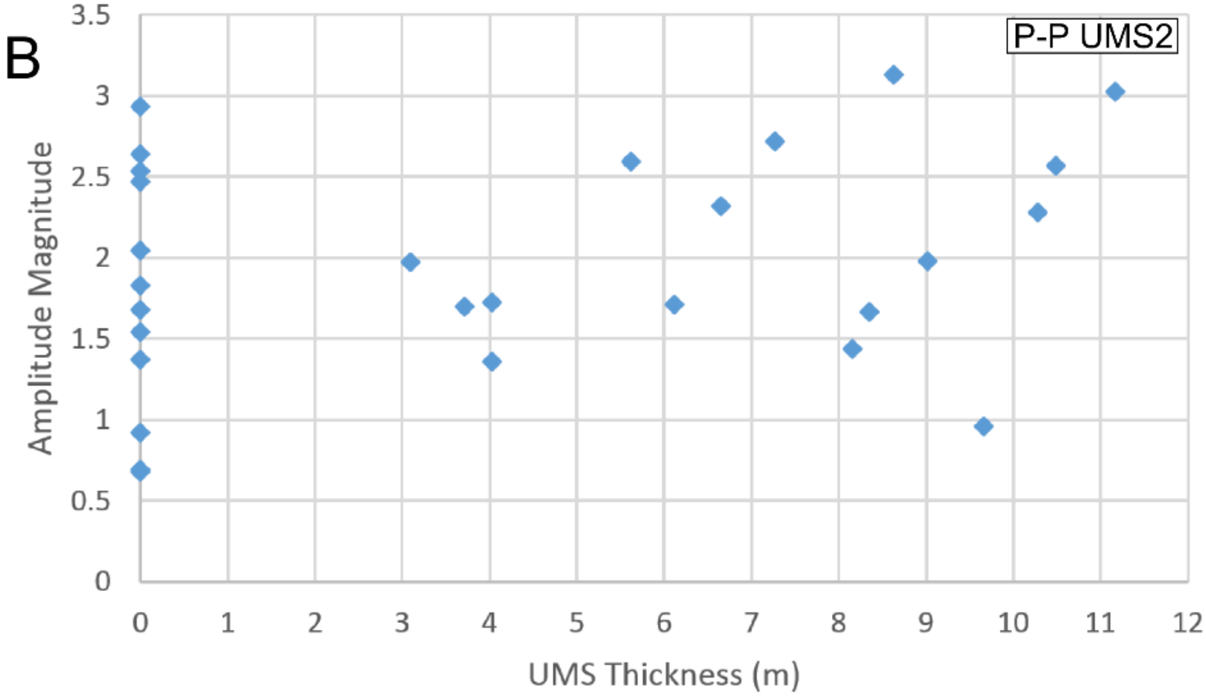

Figure 6.15. (A) P-P amplitude magnitudes of horizon UMS1 at well locations. (B) P-P amplitude magnitudes of horizon UMS2 at well locations. There is no discernible relationship between amplitudes and UMS thickness.

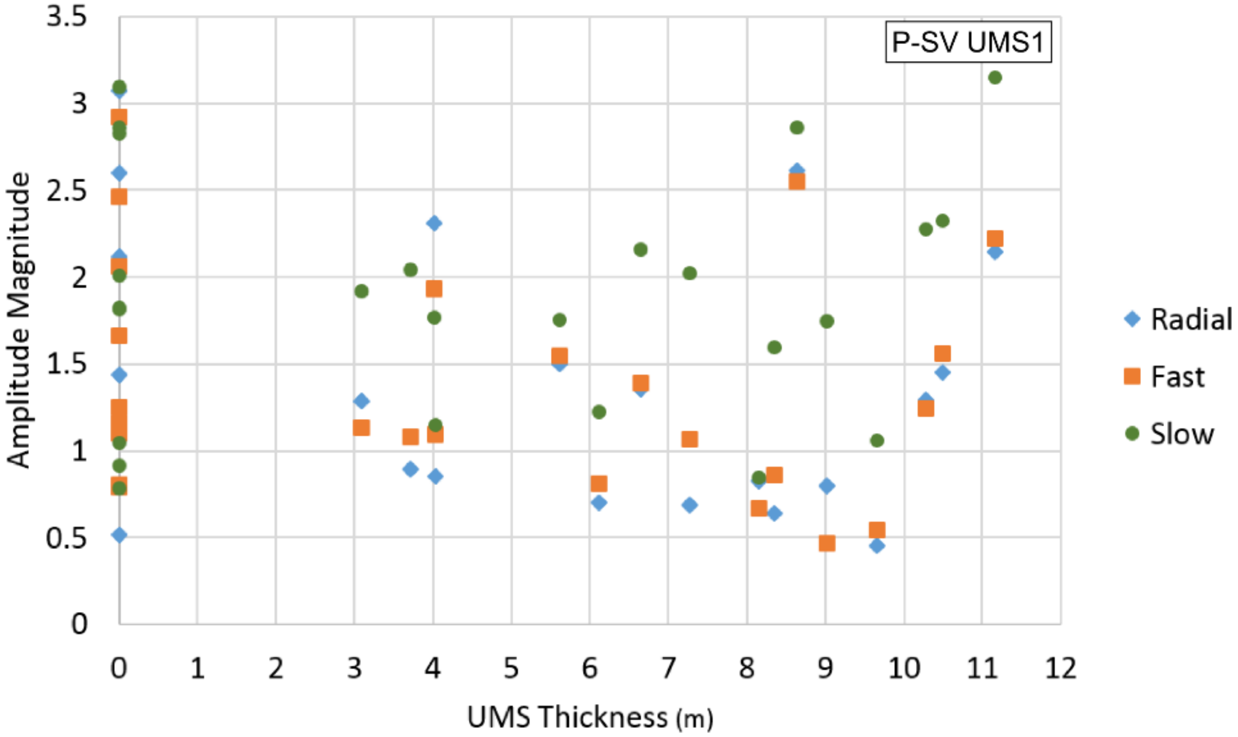

Figure 6.16. (A) P-SV radial, fast and slow amplitudes magnitudes of horizon UMS1 at well locations. There is no discernible relationship between amplitudes magnitudes and UMS thickness.

6.6 Volume attributes

Volume attributes were calculated for the P-P extracted traces in the window between horizons UMS1 and UMS2. Attributes included rms amplitude, rms envelope, and rms instantaneous frequency. Values of these attributes at each well location were plotted versus UMS thickness in the wells (Figure 6.17). No significant correlations with UMS thickness were observed for rms amplitude or rms envelope. An interesting anomaly was observed in the rms instantaneous frequency values. Well locations with UMS thickness greater than 5 m show an rms instantaneous frequency value of 43 ± 2 Hz. Well locations with UMS thickness less than 5 m, show an rms instantaneous frequency of 45 ± 6 Hz. The difference in the rms instantaneous frequency values is statistically significant at the 90% confidence interval. The statistical significance was determined using a t-test for two samples assuming unequal variances and a hypothesized mean difference of zero (Walpole et al., 2012). For bed thicknesses below vertical resolution, instantaneous frequency is, in theory, inversely related to bed thickness. This relationship occurs because the reflected composite waveform is equivalent to the derivative of the source wavelet (Widess, 1973). The peak frequency of the derivative of the source wavelet is equal to $\sqrt{3/2}\, f_0$, where f_0 is the peak frequency of the source wavelet (Chung & Lawton, 1995). The inverse relationship between instantaneous frequency and thickness is verified by wedge modeling (Section 6.4).

A map of rms instantaneous frequency shows low instantaneous frequency values (~43 Hz) within the UMS reservoir location as determined by well control. However, similarly low instantaneous frequency values are located to the north and east of the UMS reservoir. Consistently higher (~45 Hz) instantaneous frequency values are located to the south and west of the UMS reservoir. It is unclear if the lower instantaneous frequency values within the UMS reservoir location are directly related to the presence of the UMS reservoir. The apparent correlation between instantaneous frequency and UMS thickness may be attributable to a bias of well locations to the south and west of the UMS reservoir, where instantaneous frequency values are consistently lower than instantaneous frequency values to the north and east of the UMS reservoir.

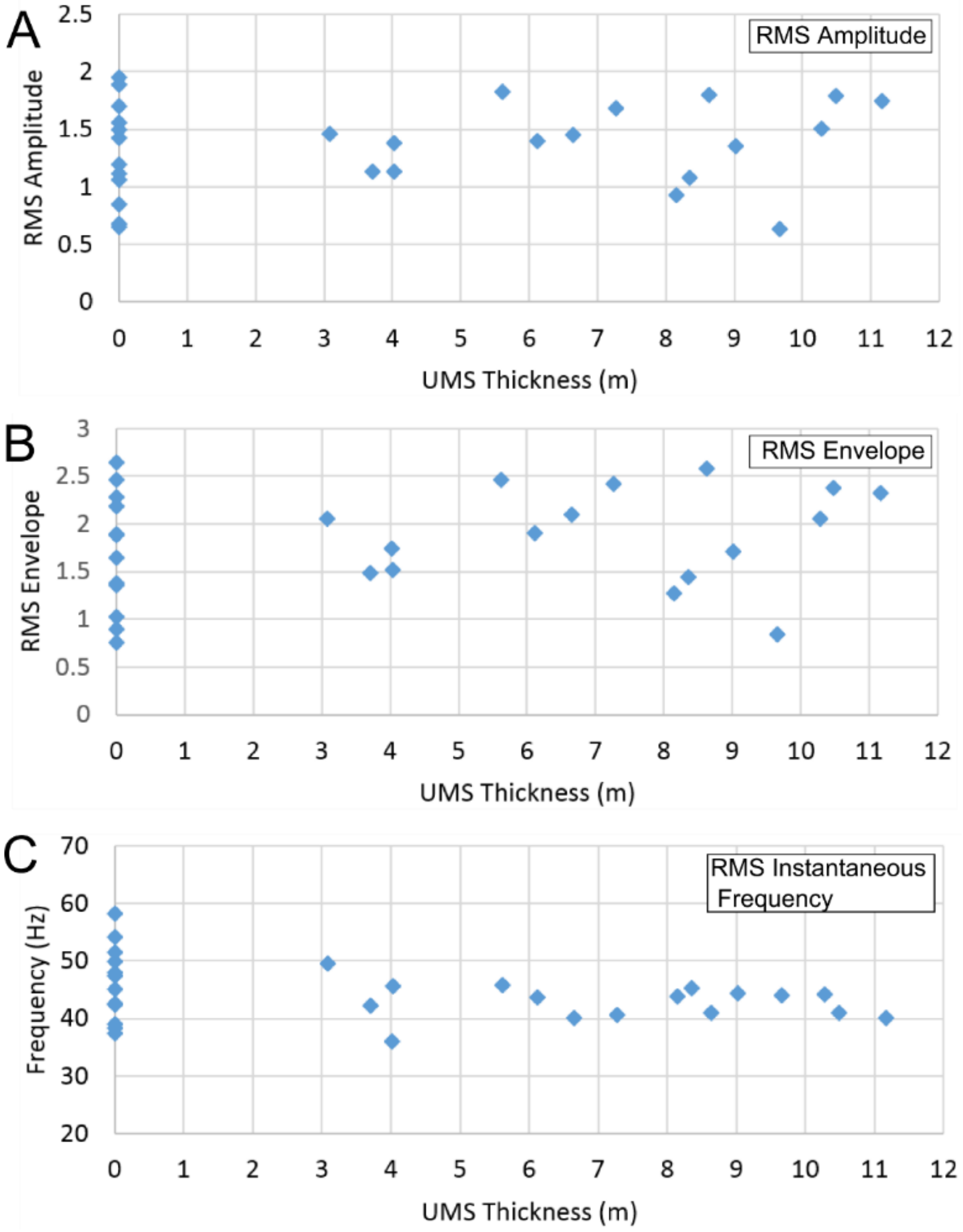

Figure 6.17. (A) P-P rms amplitude between horizons at well locations. (B) P-P rms envelope at well locations. (C) P-P rms instantaneous frequency at well locations. All values were calculated over the time interval between horizons UMS1 and UMS2. There is no discernible relationship rms amplitude or rms envelope and UMS thickness. Instantaneous frequency values tend to be lower at well locations where UMS thickness is greater than 5 m.

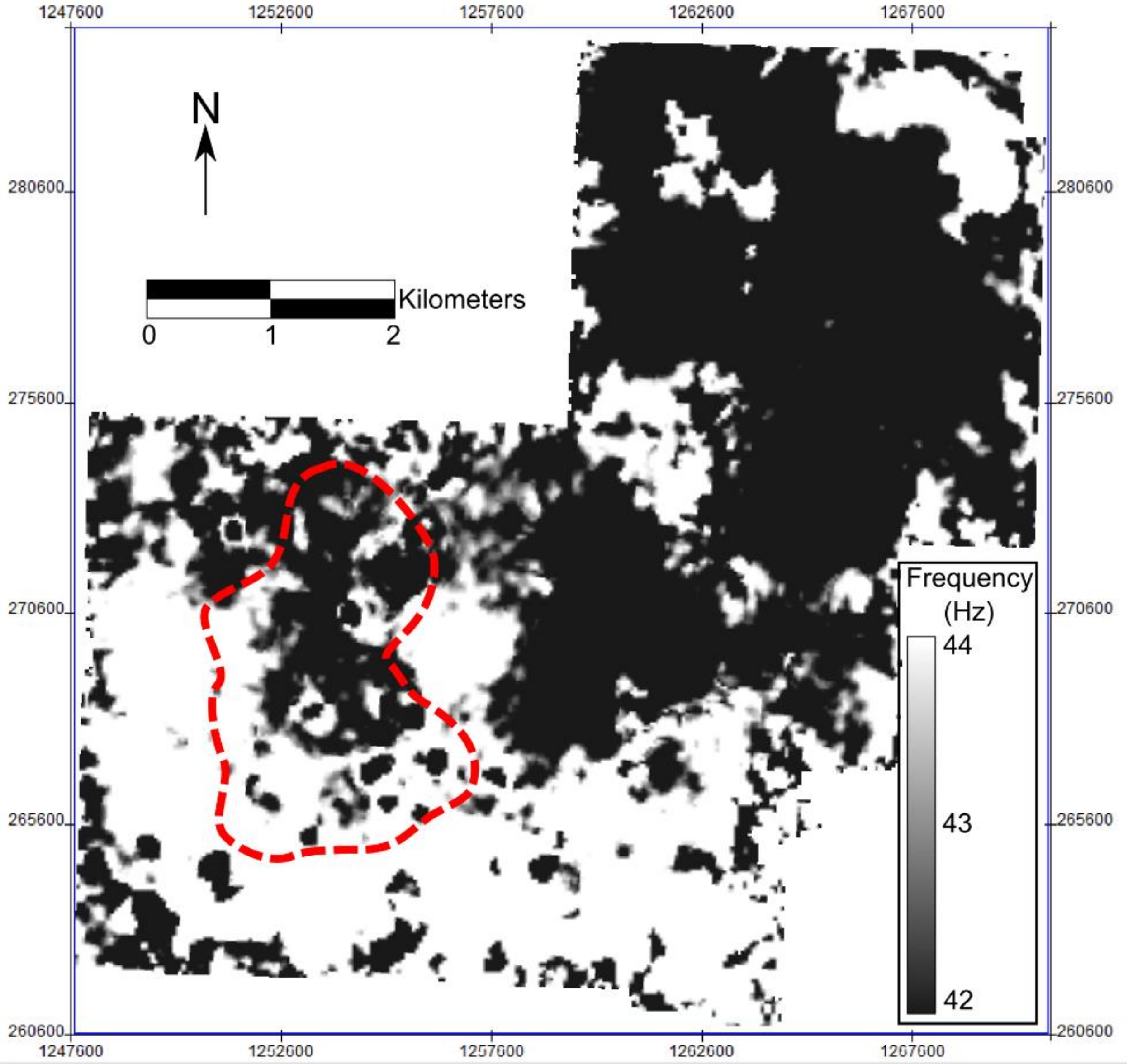

Figure 6.18. Map of rms instantaneous frequency values with UMS reservoir outline, as determined by well control. Lower instantaneous frequency values (~42 Hz) are present inside the UMS reservoir outline; however, similarly low instantaneous frequency values are present to the east and north where the UMS is absent.

6.7 P-impedance model-based inversion

P-impedance inversion can, in theory, improve seismic resolution (Latimer, 2011). This section examines if inverted P-impedance traces can resolve the UMS reservoir at Cutter Field. Model-based P-impedance inversion was performed on the P-P volume and is described in detail in Section 7.2.

Inverted P-impedance traces at the well locations of 15-189-22781, 15-189-00026, and 15-189-20021 were compared to computed P-impedance well logs from said wells. The P-P well-to-seismic tie procedure outlined in Section 5.1 was repeated for wells 15-189-00026 and 15-189-20021. Wells 15-189-00026 and 15-189-20021 lacked density logs, so a constant density of 2.4 g/cc was used to compute P-impedance. The inverted P-impedance traces and P-impedance logs were compared using Hampson-Russell Emerge over an interval of ± 10 m around the UMS reservoir (Figure 6.19). A cross plot of inverted P-impedance versus computed impedance was generated using log values averaged over 2 ms intervals. The averaging was necessary because the inverted traces are blocked on 2 ms intervals. The inverted P-impedance values show a poor correlation with the computed P-impedance values. Filtering the computed impedance logs to match the frequency of the inverted traces may improve the correlation but would “smooth out” the detail that this analysis aims to predict.

This analysis demonstrates that the inverted traces lack the resolution necessary for delineating the UMS reservoir. The failure of the inverted traces to delineate the UMS reservoir is not surprising given that the inverted traces are derived from P-P amplitudes (Section 2.7), which show a poor correlation with UMS thickness (Section 6.5).

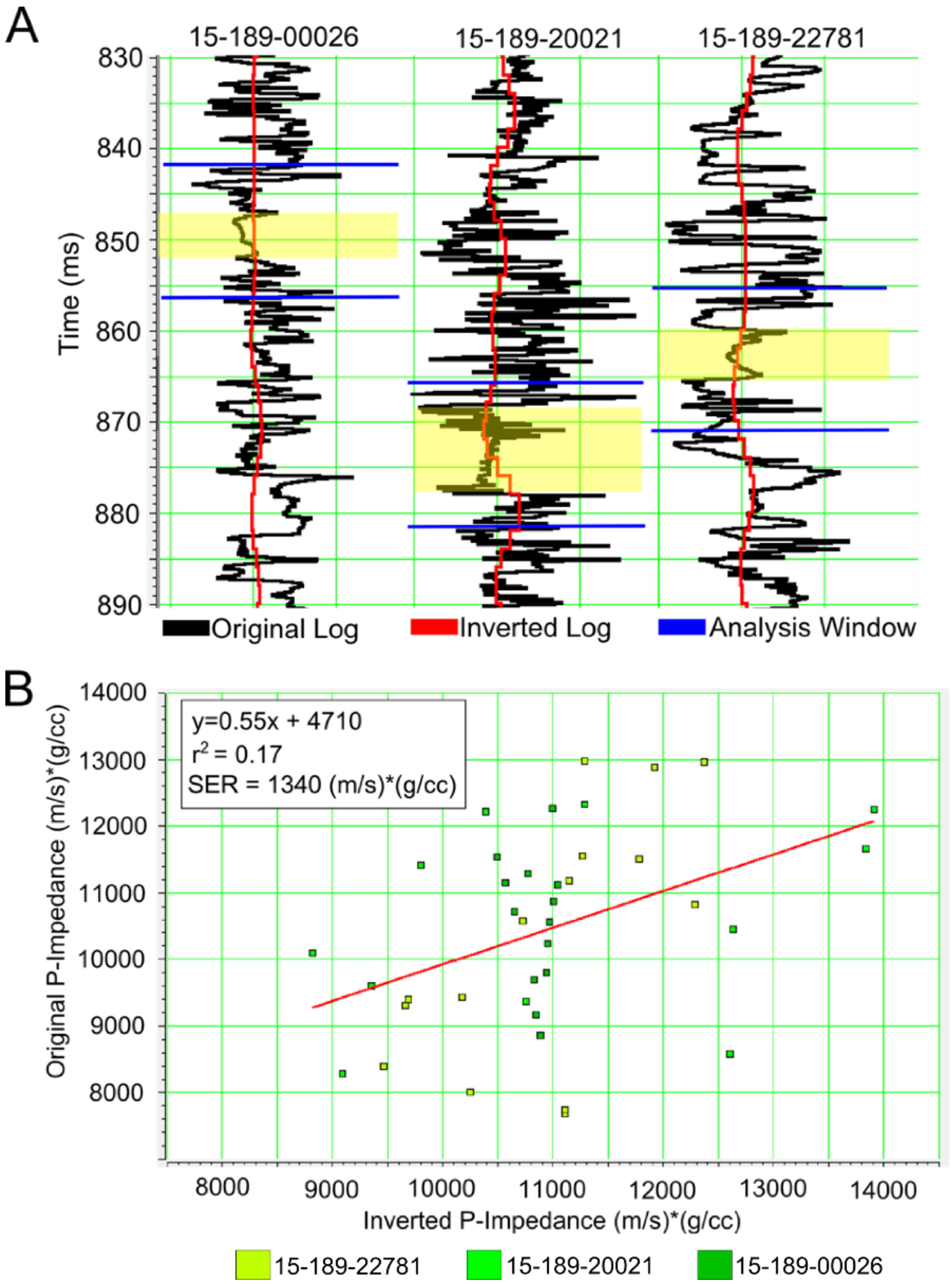

Figure 6.19. (A) Comparison of inverted (red) and well log (black) P-impedance values. The UMS reservoir is shaded in yellow. The analysis window is inside the blue lines. (B) Cross plot of inverted and well log P-impedance values averaged over 2 ms intervals from the analysis window. The inverted traces lack the resolution necessary for delineating the UMS reservoir.

6.7 Uncertainty analysis

Factors other than UMS thickness could affect amplitudes of horizons UMS1 and UMS2 including noise, lateral changes in fluid saturation, lateral changes in stratigraphy surrounding the UMS reservoir, changes in wavelet phase, lack of relative amplitude preservation during seismic processing, and acquisition artifacts.

Amplitude effects from seismic processing and acquisition artifacts could not be analyzed with the available data. Well correlations in Figures (6.2 and 6.3), show the stratigraphy directly surrounding the UMS reservoir to be vertically heterogeneous and variable from well to well. The effect of this variability on amplitudes of horizons UMS1 and UMS2 is difficult to quantify. Sonic and density logs in the survey area lack the consistency in data quality from well to well that is necessary for direct comparison of amplitudes on synthetic traces. However, since seismic reflections are primarily a response to low frequency changes in impedance, it is likely that the effect of lateral variability in stratigraphy directly surrounding the UMS reservoir on seismic amplitudes is minuscule.

Effects of fluid saturation on seismic amplitudes were modeled using the Hampson-Russell AVO software package. Fluid replacement modeling in Hampson-Russell AVO is based on Biot-Gassman theory (Gregory, 1997). Modeling was conducted using density, sonic, and neutron porosity logs from well 15-189-22781. Fluid saturation was varied from 100% brine to 100% gas in increments of 5%. The transition from 100% brine to 100% gas represents the largest possible change in elastic properties that could be caused by fluid saturation effects. A zero-offset trace was computed for each fluid saturation increment using a 42 Hz, 90 degree phase rotated Ricker wavelet. Horizon UMS2 was picked on the synthetic data and the amplitude magnitudes of horizon UMS2 were plotted as a function of gas saturation (Figure

6.20). The fluid saturation modeling demonstrates that fluid saturation can change amplitude magnitudes by ~10%. At well locations on the P-P volume where the UMS is interpreted to be absent, horizon UMS2 has an amplitude of 1.78 ± 0.77, where the uncertainty is given by one standard deviation. The uncertainty of 0.77 equates to ~43% of the mean. Therefore, the ~10% uncertainty caused by lateral changes in fluid saturation cannot alone account for the ~43% uncertainty seen in horizon UMS2.

The convolutional model used for computing synthetic traces in this study relies on the critical assumption that the seismic wavelet remains constant. In practice, seismic wavelets vary both spatially and in time with each survey. To estimate an uncertainty in wavelet phase, the “extract wavelet using wells” procedure described in Section 5.1 was repeated for three additional wells. The four extracted wavelets had an average wavelet phase of 117 ± 23 degrees, where ± 23 represents one standard deviation. Some of the variability in the extracted wavelets may be related to variable data quality between the sonic logs at each well. A phase uncertainty of ± 15 degrees was assumed for modeling purposes. The wedge model procedure described in Section 6.4 was repeated using a 42 Hz, 75 degree phase rotated Ricker wavelet and a 42 Hz, 105 degree phase rotated Ricker wavelet. The effect of amplitude on phase was inspected in horizons UMS1 and UMS2. The wedge modeling shows that a phase uncertainty of ± 15 degrees can change amplitude magnitudes by ~5% (Figure 6.21). Therefore, a phase uncertainty of ± 15 degrees cannot, alone, account the ~43% uncertainty seen in horizon UMS2.

The signal-to-noise ratio (S/N) of the P-P volume was estimated using a method developed by Lui and Li (1997). S/N was calculated over an inline range of 113-115, crossline range of 57-59, and time window of 850 – 880 ms. The time window includes the UMS interval and the trace range satisfies the assumptions of the method, namely that the waveform, amplitude, and phase of the seismic wavelet in the window remain stable. The Lui and Li (1997) method gives a S/N of 6.5 over said time window and trace range. Here, S/N is defined as

$$\frac{S}{N} = \frac{|A_{Signal}|}{|A_{Noise}|}, \tag{6.1}$$

A S/N of 6.5 represents an uncertainty in amplitude of ~15%. A S/N of 6.5 cannot alone account for the ~43% variability in amplitude seen in horizon UMS2. The trace range used to calculate the S/N of 6.5 only represents a small area of the survey. S/N is likely to decrease with closer proximity to the perimeter of the survey, due to lower fold near the survey perimeter.

The combined uncertainties of fluid saturation, wavelet phase, and noise, if they all impacted the signal in the same direction, could amount to an uncertainty in amplitude of ~30%. The combined maximum uncertainty of ~30% could not fully account for the ~43% variability in the amplitude of horizon UMS2. The remaining ~13% of variability is likely attributed to other factors that could not be quantified in this study, namely, lateral changes in the stratigraphy directly surrounding the UMS reservoir, poor amplitude preservation during seismic processing, and acquisition artifacts.

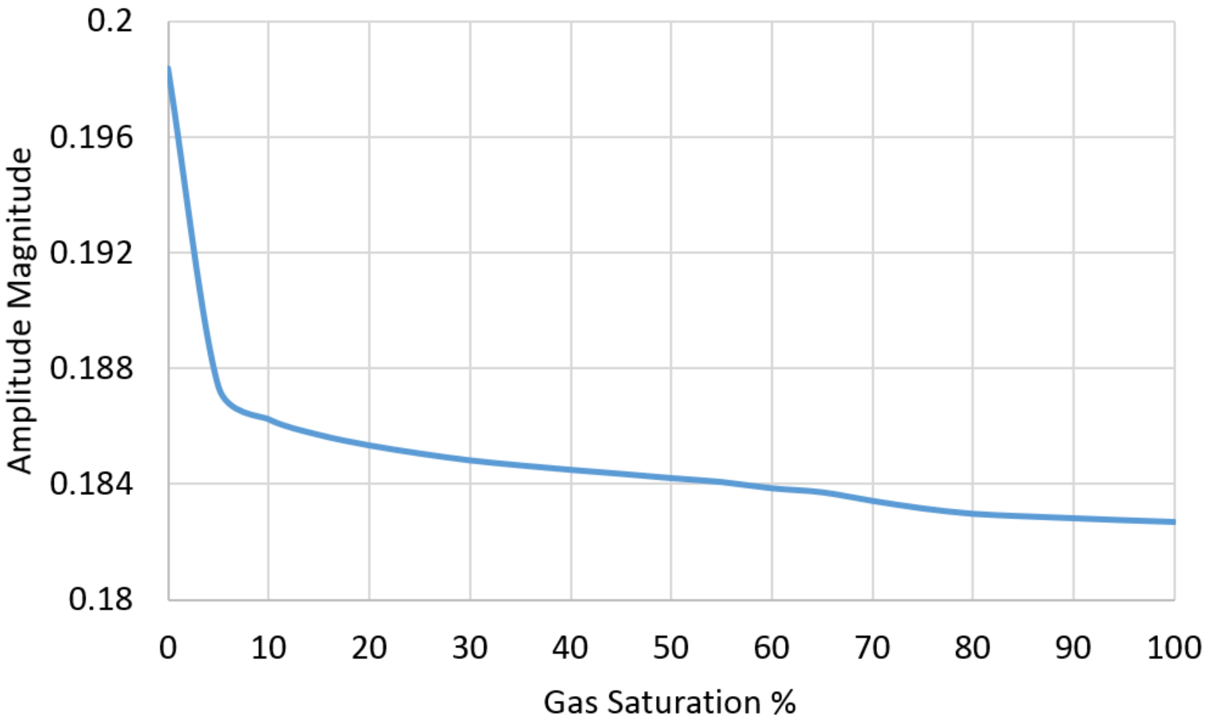

Figure 6.20. Horizon UMS2 as picked on the synthetic seismogram produced in the fluid saturation modeling. The initial state of the fluid saturation model is 100% brine. The brine is replaced by gas until the fluid suturing is 100% gas. The modeling shows ~10% change in the amplitude of horizon UMS2.

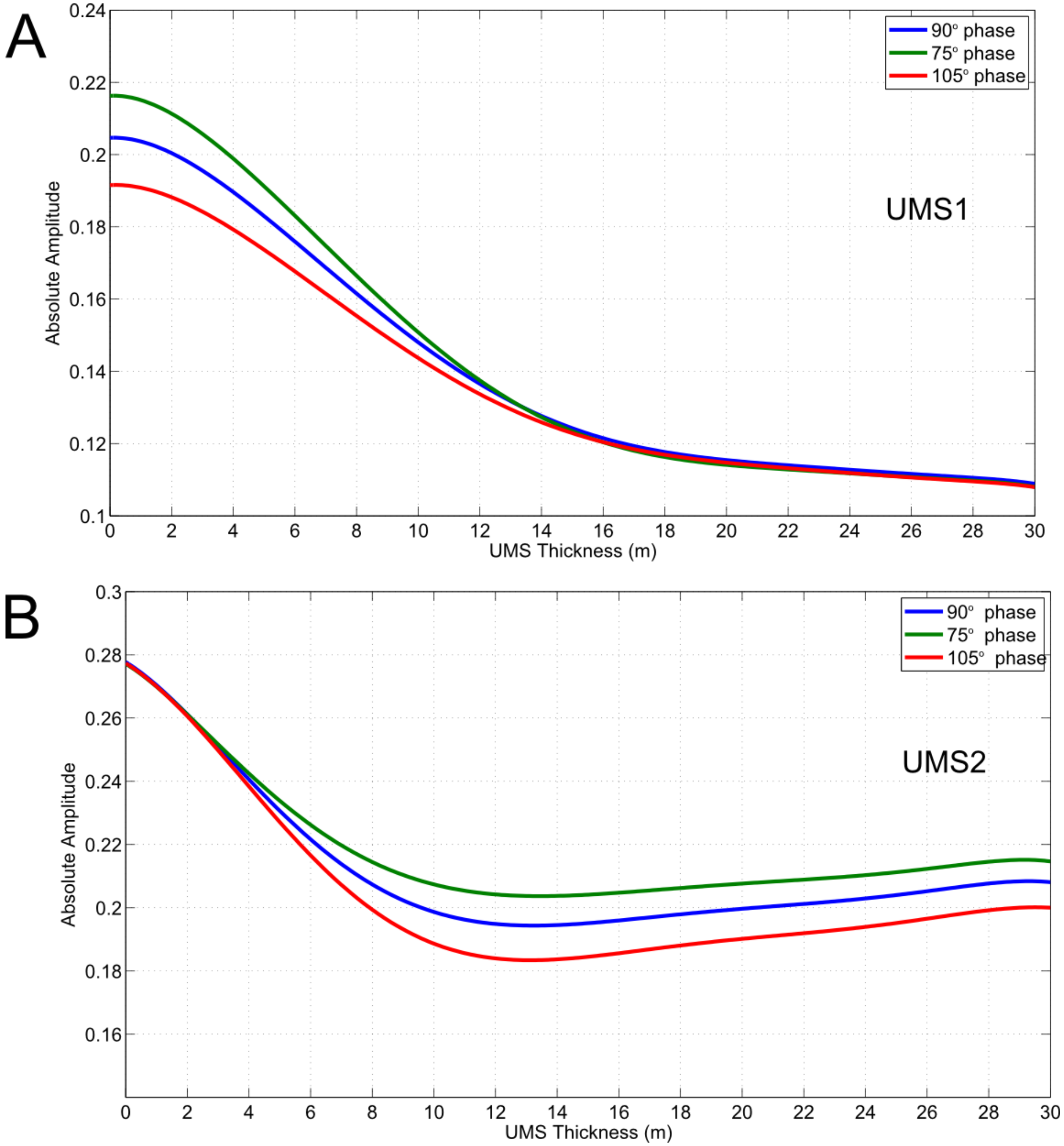

Figure 6.21. (A) P-P UMS1 and (B) P-P UMS2 amplitude magnitudes picked on wedge models generated with wavelet phases of 90, 75, and 105 degrees.

6.8 Summary of Upper Morrow Sandstone results

The UMS at Cutter Field is below resolution of the both the P-P and P-SV data. The maximum thickness of the UMS in terms of seismic wavelengths is ~1/8 λ for the P-P data and ~1/12 λ for the P-SV data. The P-impedance contrast between the UMS and encasing shale is greater at Cutter Field than in other areas of the Anadarko Basin (Singh and Davis, 2011). AVO modeling shows that P-SV waves offer only a slight advantage in reflection strength and only for P wave incidence angles greater than ~15 degrees. These considerations, coupled with the visibly lower signal-to-noise-ratio of the P-SV data, suggest that P-P data provides the highest probability of detecting the UMS at Cutter Field. The Cutter 3D-3C data showed no correlation between amplitudes and UMS thickness or inverted P-impedance and UMS thickness. The predicted tuning effect of the thin UMS reservoir is subtle and detection requires a high signal-to-noise ratio. A possible relationship between instantaneous frequency and UMS thickness was identified but is inconclusive.

Chapter 7: Arbuckle Group methods and result

7.1 Well log analysis

The Arbuckle Group at Cutter Field is approximately 2050 m deep and 250 m thick. It is characterized by an average neutron porosity of 7%, average P wave velocity of 6000 m/s, average S wave velocity of 3330 m/s, and average density of 2.7 g/cc (Figure 7.1). Cross plotting of neutron porosity versus computed P-impedance logs from well 15-189-22781 revealed an inverse relationship between porosity and P-impedance within the Arbuckle Group (Figure 7.2). The inverse relationship exhibited an r-squared value of 0.56 and standard error of regression of 0.02 porosity units. This correlation between neutron porosity and P-impedance is significant at the 99.9% confidence interval.

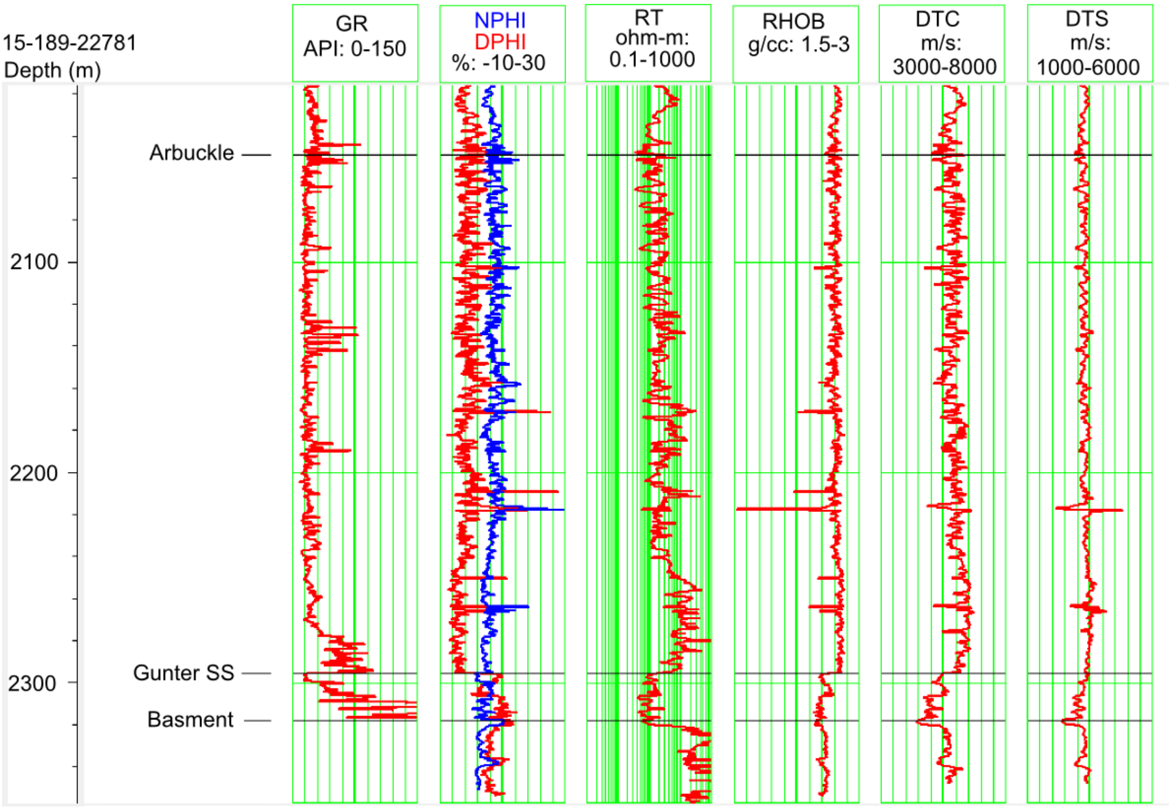

Figure 7.1. Well log response of the Arbuckle Group at Cutter Field. Neutron porosity within the Arbuckle Group ranges from 3-13%.

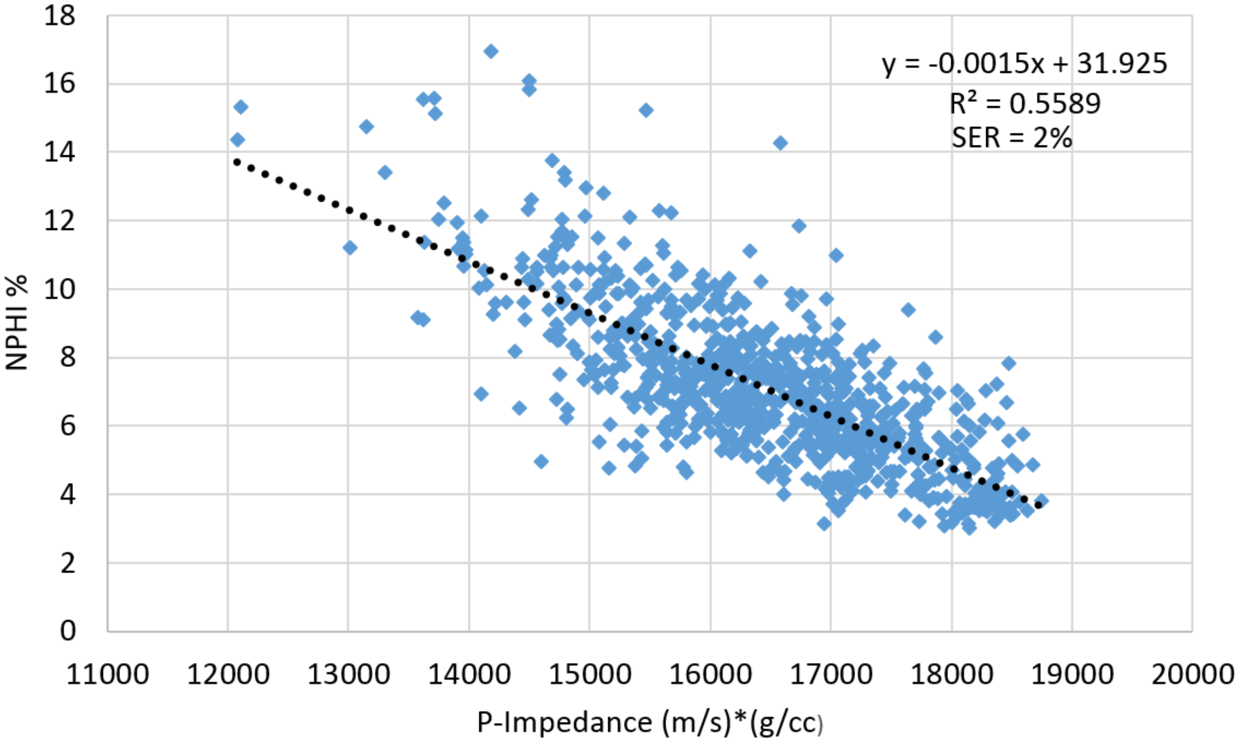

Figure 7.2. Arbuckle Group cross plot of neutron porosity versus computed P-impedance logs from well 15-189-22781. The correlation between neutron porosity and P-impedance is significant at the 99.9% confidence interval.

7.2 Post-stack model-based inversion

A post-stack model-based inversion was performed using the Hampson-Russell Strata software package. The inversion procedure, as described in Section 2.7, includes three basic steps: (1) wavelet estimation, (2) construction of an initial low frequency model, and (3) perturbing the model iteratively to produce an inverted P-impedance volume. The wavelet extraction procedure is described in Section 5.1. Wavelet P-P 22781 was used for the inversion.

Inputs for the initial low-frequency model were sonic and density logs from the well 15-189-22781 and the following horizons: Shawnee, Kansas City, Cherokee, Morrow, Viola, and Basement (Figure 7.3). Parameters for the initial low-frequency model are shown in Table 7.1

The final step of perturbing the initial low-frequency model is performed by running the inversion script written into the Hampson-Russell Strata software package. Prior to inverting the full seismic volume, the “inversion analysis” feature was used to analyze the accuracy of the inversion at the location of well 15-189-22781 (Figure 7.4). The inverted P-impedance was found to slightly overestimate the computed P-impedance log from well 15-189-22781. To improve the correlation, the “scalar” inversion parameter, which modifies the scale of the source wavelet, was decreased from 1.0 to 0.8. Increasing the “number of iterations” parameter from 10 to 50 was also found to improve the correlation. The final parameters used to invert the full seismic volume are shown in Table 7.2. A cross plot of the inverted P-impedance and computed P-impedance from well 15-189-22781 showed an r-squared value of 0.74 and standard error of regression of 1094 (m/s)*(g/cc) (Figure 7.5). A correlation coefficient of 0.99 was observed between the synthetic trace calculated on the inverted P-impedance and the observed P-P trace at the location of well 15-189-22781. A visual inspection of the inverted P-impedance along inline

114 reveals that the inversion clearly captures the low-frequency impedance trend that is present in the computed P-impedance log of well 15-189-22781 (Figure 7.6).

Setup	"Typical setup for Acoustic Impedance Inversion"
Wells	15-189-22781
Horizons	Shawnee, Kansas City, Cherokee, Morrow, Viola, Basement
Highcut frequency	10 / 15 Hz
Time range	680 – 1140 ms
Inline range	20 - 160
Crossline range	20 - 180
Trace filtering options	"Apply a smoother on modeled trace in the output domain"

Table 7.1. Input parameters for the initial low frequency model.

Inversion type	"Model Based – Hard Constraint"
Maximum change (single value: Upper)	100%
Maximum change (single value: Lower)	100%
Average block size:	2 ms
Prewhitening	1%
Number of iterations	50
Scalaer adjustment factor	0.8
Time range	680 – 1140 ms
Inline range	20 - 160
Crossline range	20 - 180

Table 7.2. Input parameters for the P-impedance inversion.

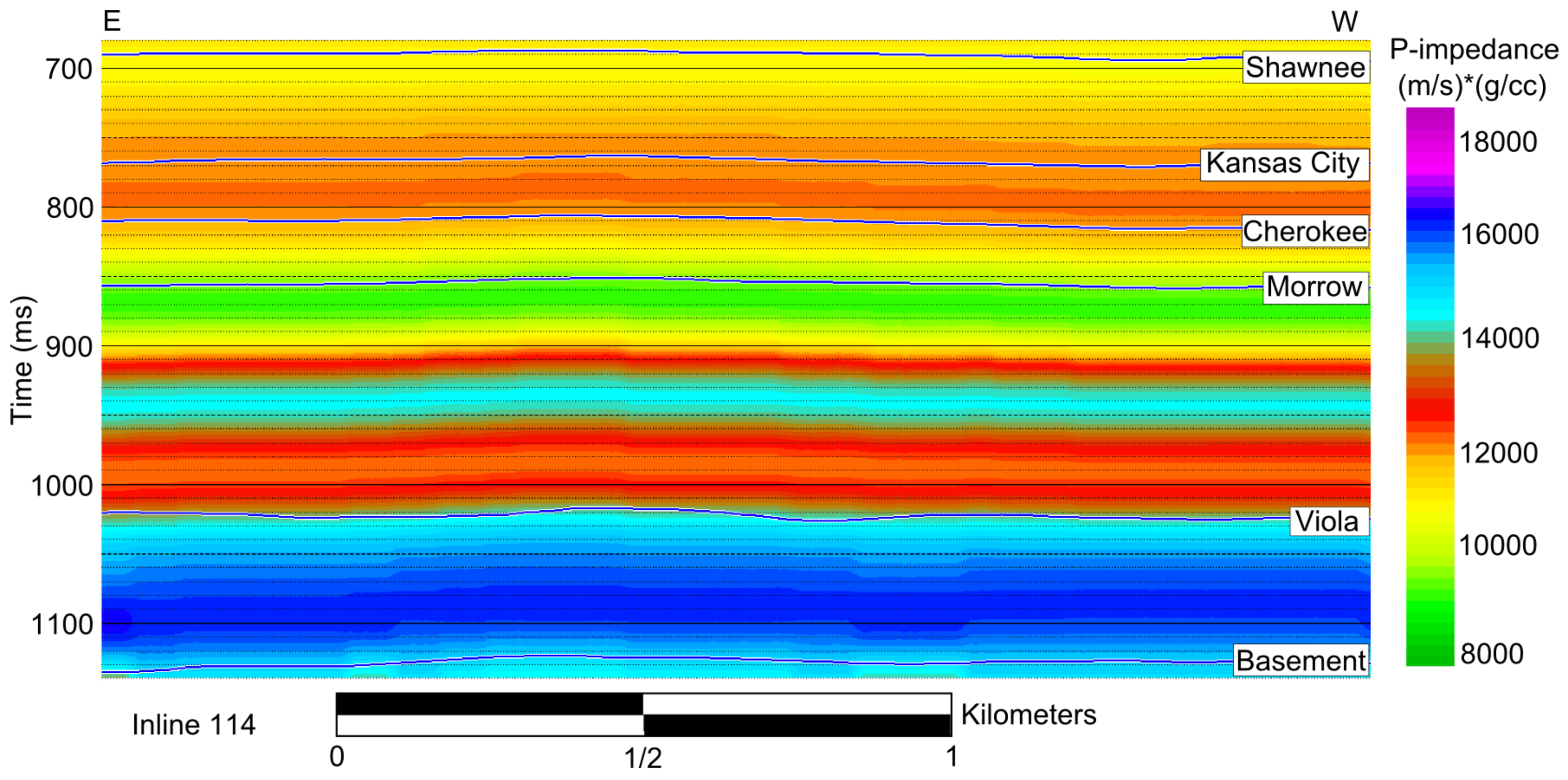

Figure 7.3. Initial P-impedance model. The initial model contains the low-frequency P-impedance trend in the stratigraphic section.

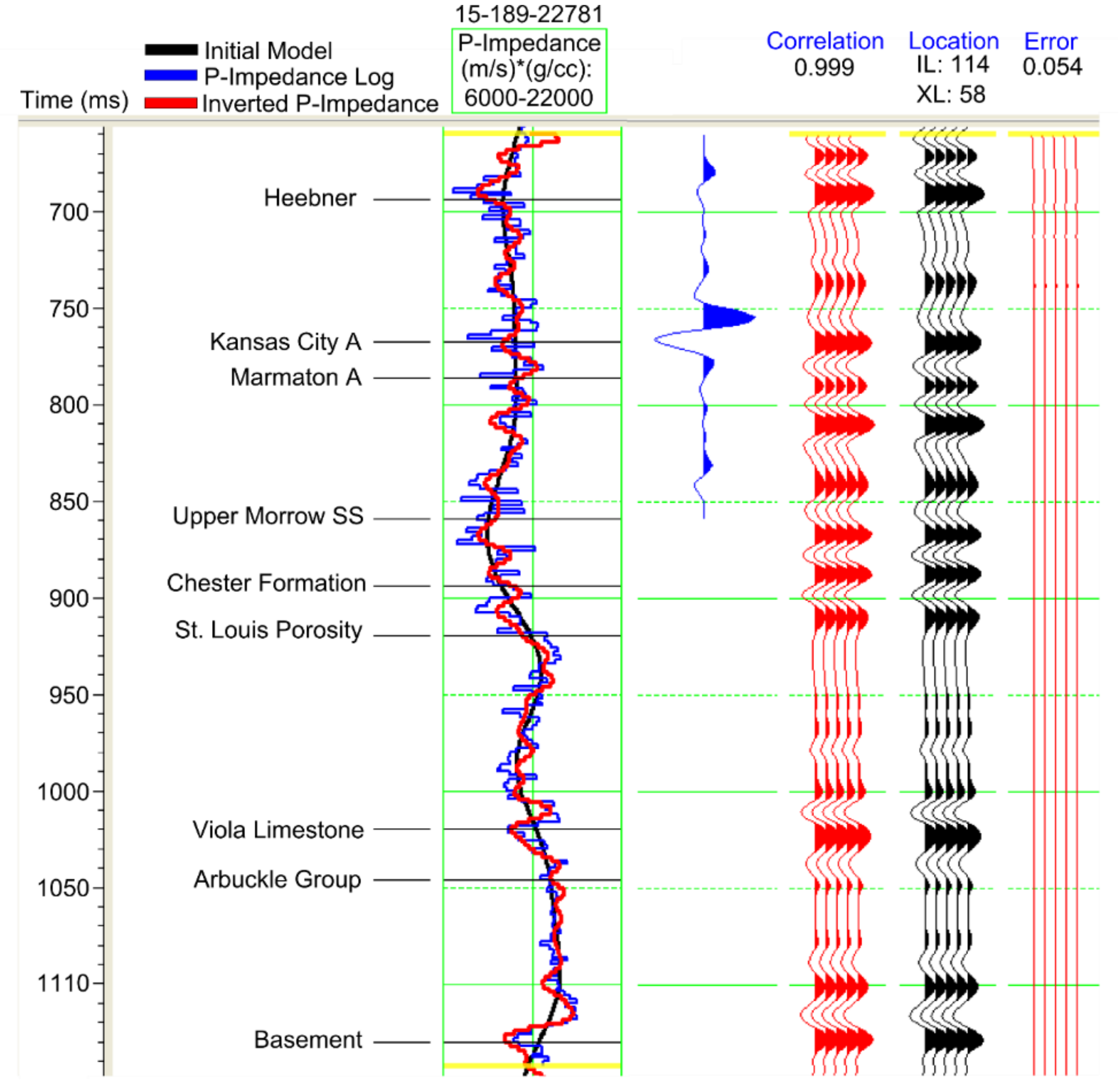

Figure 7.4. Inversion analysis at well 15-189-22781. The inverted P-impedance log closely resembles the computed impedance log and produces a synthetic trace nearly identical to the observed trace.

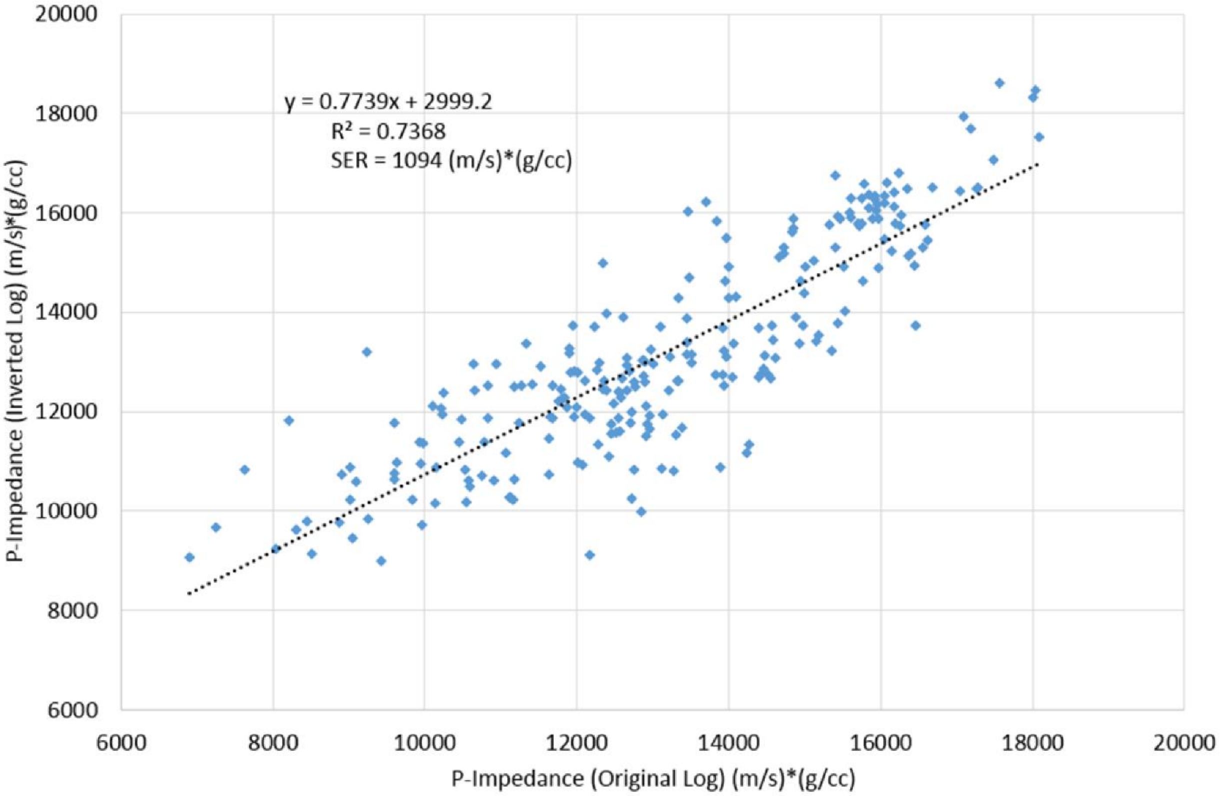

Figure 7.5. Cross plot and regression of inverted P-impedance log versus original P-impedance log.

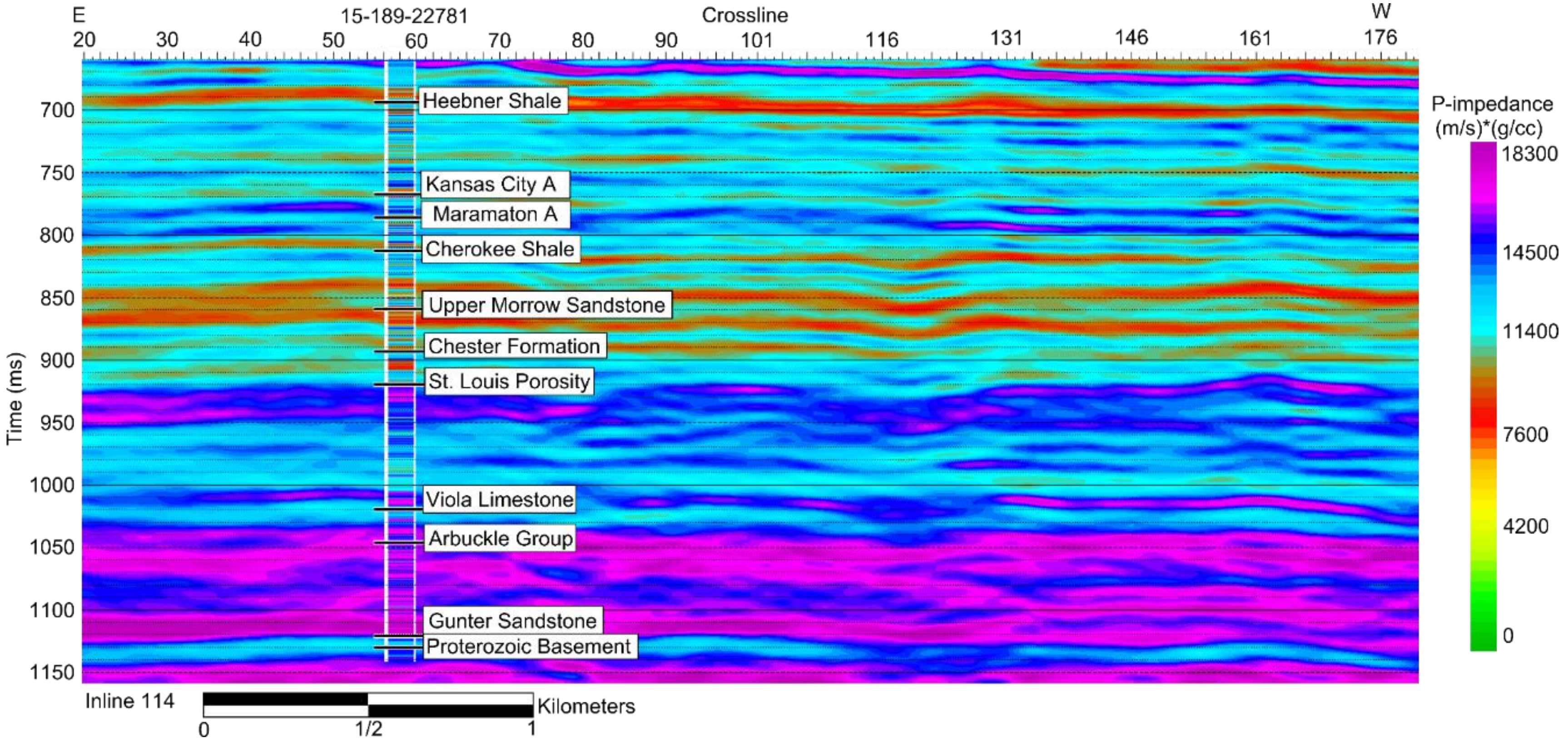

Figure 7.6. Inverted P-impedance profile with inserted P-impedance log from well 15-189-22781. The inverted volume lacks the resolution of the well log but provides an accurate approximation.

7.3 Porosity predictions

Low P-Impedance zones in the Arbuckle Group were identified by selectively removing P-impedance values greater than 13500 (m/s)*(g/cc) from the inverted volume (Figure 7.7). Based on the relationship between neutron porosity and P-impedance (Section 7.1), these zones are predicted to have porosities greater than 12%. The volume display shows several isolated zones of low P-impedance occurring stratigraphically in the middle of the Arbuckle Group, within a time range of 1070 – 1090 ms and a corresponding depth range of 2125 m – 2190 m. These low P-impedance zones appear to be related to high amplitude reflections within the Arbuckle Group (Figure 7.8). Analysis of Arbuckle Group strata from wells in south-central Kansas suggests that high porosity zones within the Arbuckle Group can be caused by brecciation (Lynn Watney, personal communication, March 7, 2015). More well control is needed to test the accuracy of the porosity predictions.

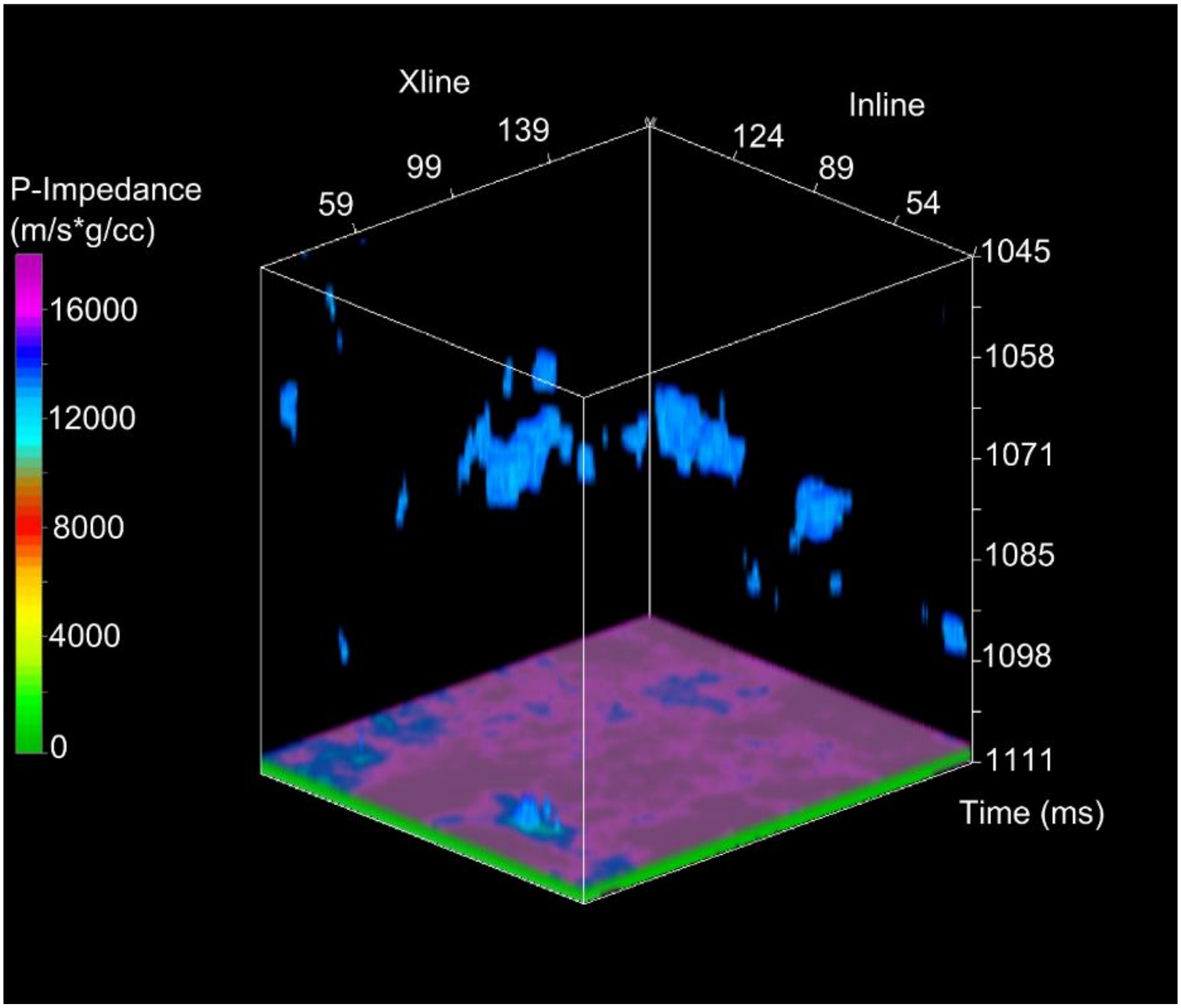

Figure 7.7. P-impedance volume of the Arbuckle Group with high impedance values removed. The remaining bodies (in blue) are predicted to have porosities greater than 12%.

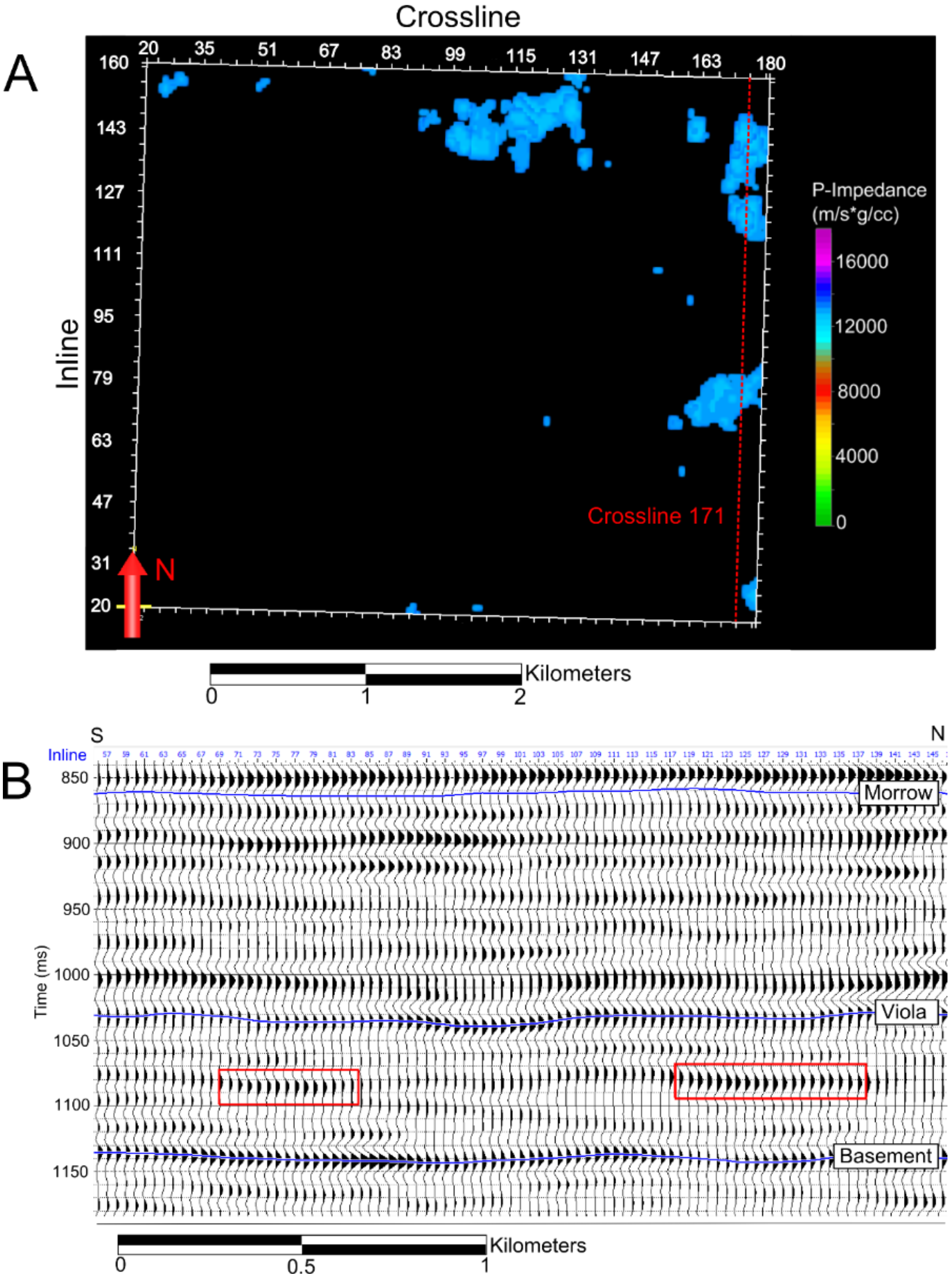

Figure 7.8. (A) Plan view of low P-impedance zones. Red dotted line indicates crossline 171. (B) P-P seismic section of crossline 171. Red boxes indicate location of low P-impedance zones. The low P-impedance zones appear to be related to high amplitudes within the Arbuckle Group.

7.4 Flow unit analysis

Gerlach (2014) identified three flow units within the Arbuckle Group at well 15-189-22781. The flow units appear to coincide with P-impedance layers on a low-pass filtered computed P-impedance log from well 15-189-22781 (Figure 7.9). Flow unit 3 coincides with a high P-impedance zone in the upper Arbuckle, flow unit 2 coincides with a low P-impedance zone in the middle Arbuckle, and flow unit 1 coincides with a high P-impedance zone in the lower Arbuckle. The coincidence of three flow units with three P-impedance layers suggests that flow unit boundaries within the Arbuckle Group may be related to P-impedance boundaries and can potentially be mapped with seismic methods.

However, seismic reflections within the Arbuckle Group are highly discontinuous and cannot be picked across the seismic volume (Figures 5.7 & 7.6). To examine if the low frequency impedance trend observed at well 15-189-22781 is laterally extensive, the P-impedance inverted volume was flattened on the Cherokee horizon to remove regional structure, and the mean value of each time slice was calculated through the Arbuckle Group. The resulting curve (Figure 7.10) shows the same three-layer pattern that was observed in the low-pass filtered computed P-impedance log from well 15-189-2278, namely high P-impedance in the upper Arbuckle, low P-impedance in the middle Arbuckle, and high P-impedance in the lower Arbuckle. The averaged P-impedance curve provides evidence that three-layer P-impedance trend is laterally extensive through the volume. A comparison of P-impedance time slices from the upper, middle, and lower Arbuckle Group further supports the notion that the three-layer P-impedance trend is laterally extensive (Figure 7.11). The time slices also reveal the presence of isolated high P-impedance zones in the middle Arbuckle, which may contribute to the discontinuity of the seismic reflections within the Arbuckle Group.

Given that the three P-impedance layers in the Arbuckle Group are laterally extensive and that neutron porosity within the Arbuckle Group is related to P-impedance (Section 7.1), it follows that porosity within the Arbuckle Group can be approximated by a three-layer model. The relationship between neutron porosity and P-impedance within the Arbuckle Group predicts the upper Arbuckle to have low porosity, the middle Arbuckle to have high porosity, and the lower Arbuckle to have low porosity. However, since the layers are not uniform, this three-layer model is only valid on a field-wide scale.

If the flow unit boundaries are indeed related to the P-impedance boundaries, then the lateral extensiveness of the P-impedance layers implies that the flow units should also be laterally extensive. In this case, flow units can also be approximated by a three-layer model on a field-wide scale. It is worth noting that lateral extensiveness does not necessarily imply continuity. More well control is needed to test the relationship between flow unit boundaries and P-impedance boundaries. A study by Fadolalkarem (2015) showed good agreement between pre-stack inverted P-impedance boundaries and flow unit boundaries within the Arbuckle Group at south-central Kansas.

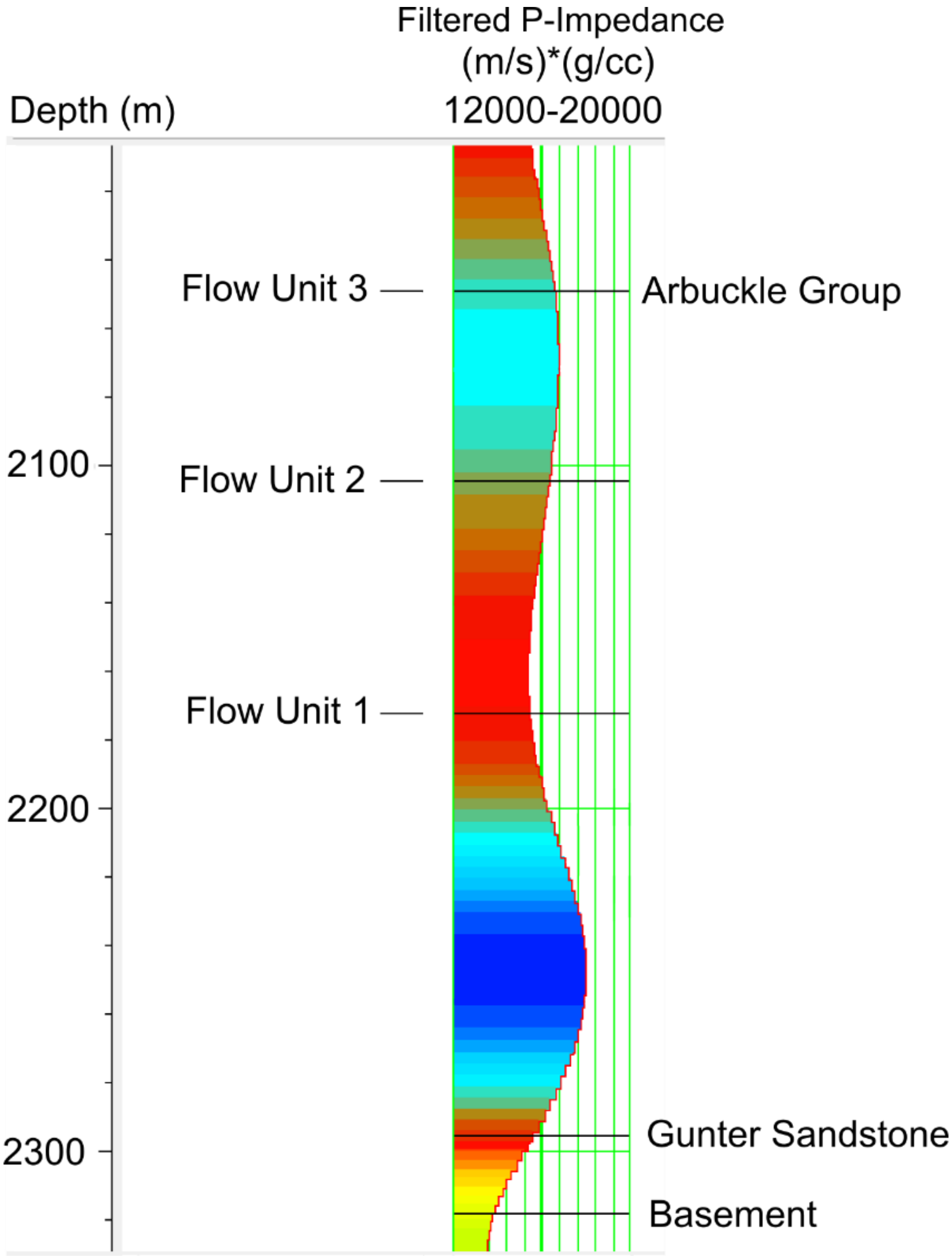

Figure 7.9. Filtered P-impedance curve with flow unit tops and formation tops. Flow unit 3 corresponds to a high P-impedance zone in the upper Arbuckle, flow unit 2 corresponds to a low P-impedance zone in the middle Arbuckle, and flow unit 1 corresponds to a high P-impedance zone in the lower Arbuckle.

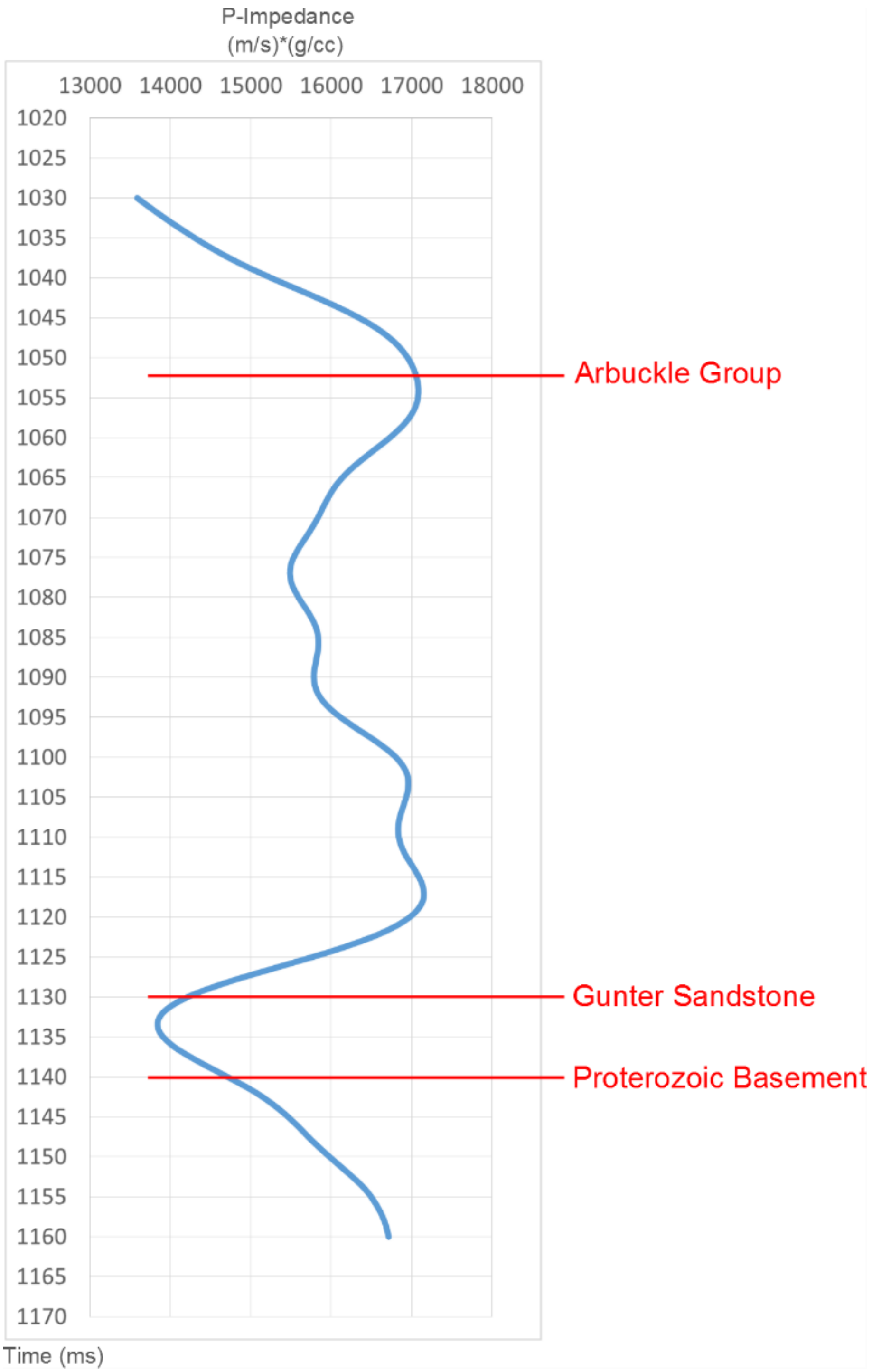

Figure 7.10. Average P-impedance of each time slice through the flattened inverted volume. This curve represents the average P-impedance trend over the entire survey area, as a function of time. The P-impedance layering that is evident in well 15-189-22781, namely high P-impedance in the upper Arbuckle, low P-impedance in the lower Arbuckle (Figure 7.8), is also evident in the average curve. This result suggests that the P-impedance layers are laterally extensive.

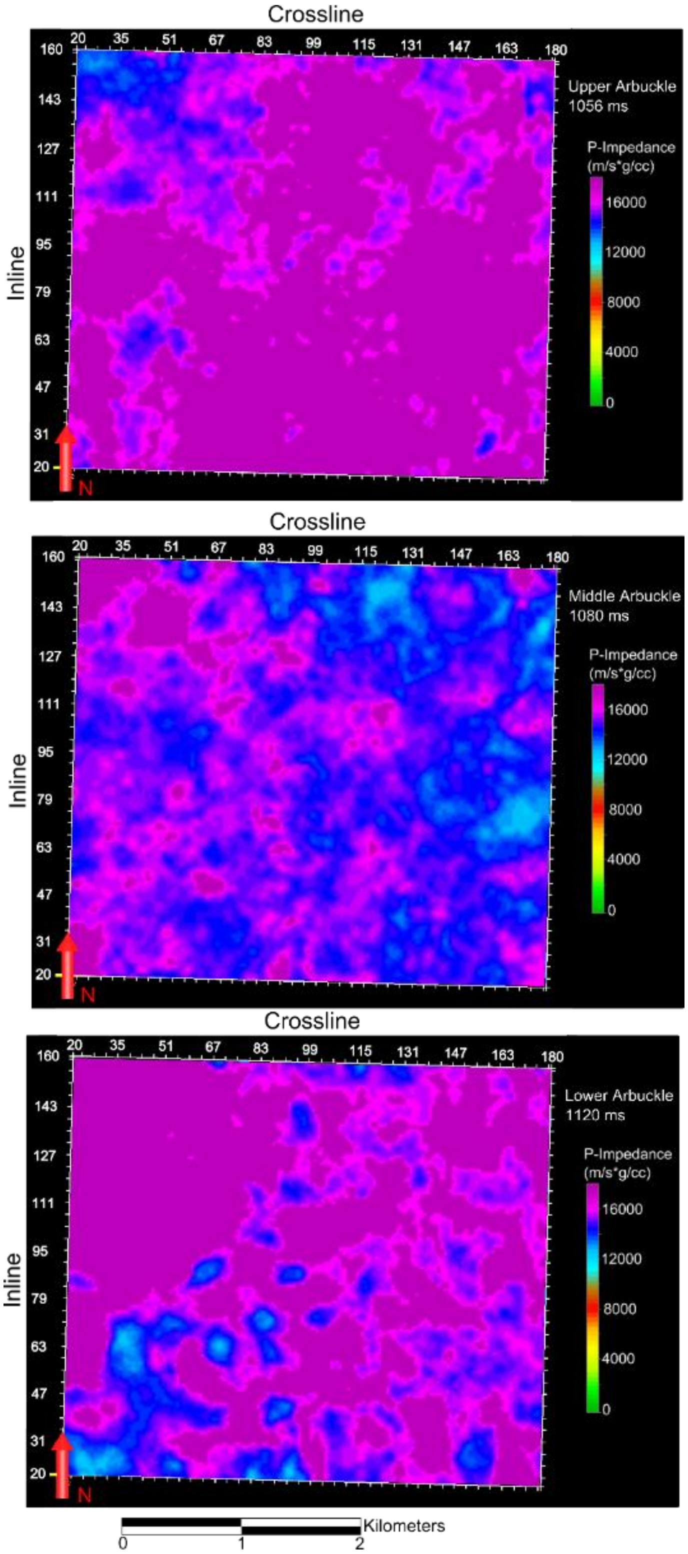

Figure 7.11. Comparison of P-impedance time slices through the upper, middle, and lower Arbuckle Group ordered from top to bottom figure panels. The time slices reveal a high P-impedance layer in the upper Arbuckle, a low P-impedance layer in the middle Arbuckle and a high P-impedance layer in the lower Arbuckle.

7.5 P-SV fast and slow time delay

Dipole sonic logs acquired at well 15-189-22781 show an average difference in fast and slow S wave velocity of ~90 m/s within the Arbuckle Group. This difference corresponds to ~2 ms of one- way time delay between fast and slow S waves traveling through the Arbuckle. Based on the theory of shear wave splitting, described in Section 2.3, this time delay is expected to be related to fracture density. A longer time delay is expected over areas that are highly fractured. An attempt to map this time delay through the Arbuckle Group and identify fracture zones was made by comparing isochron maps constructed from the Viola and Basement horizons on the P-SV Fast and P-SV Slow volumes. The high discontinuity of the P-SV reflections at Arbuckle Group depth made this a difficult endeavor. Horizons could only be picked reliably over a small area of the survey. The final time delay map contains a wide range of both positive and negative values that are geologically unrealistic (Figure 7.10). A dominant NW-SE trend is evident on the time delay map. The cause and significance of the trend is uncertain. The poor result of the time-delay analysis is most likely attributable to the poor P-SV data quality at Arbuckle depth. However, the presence of both negative and positive time delays could indicate that the fast and slow directions used to process the P-SV data are not valid for the Arbuckle.

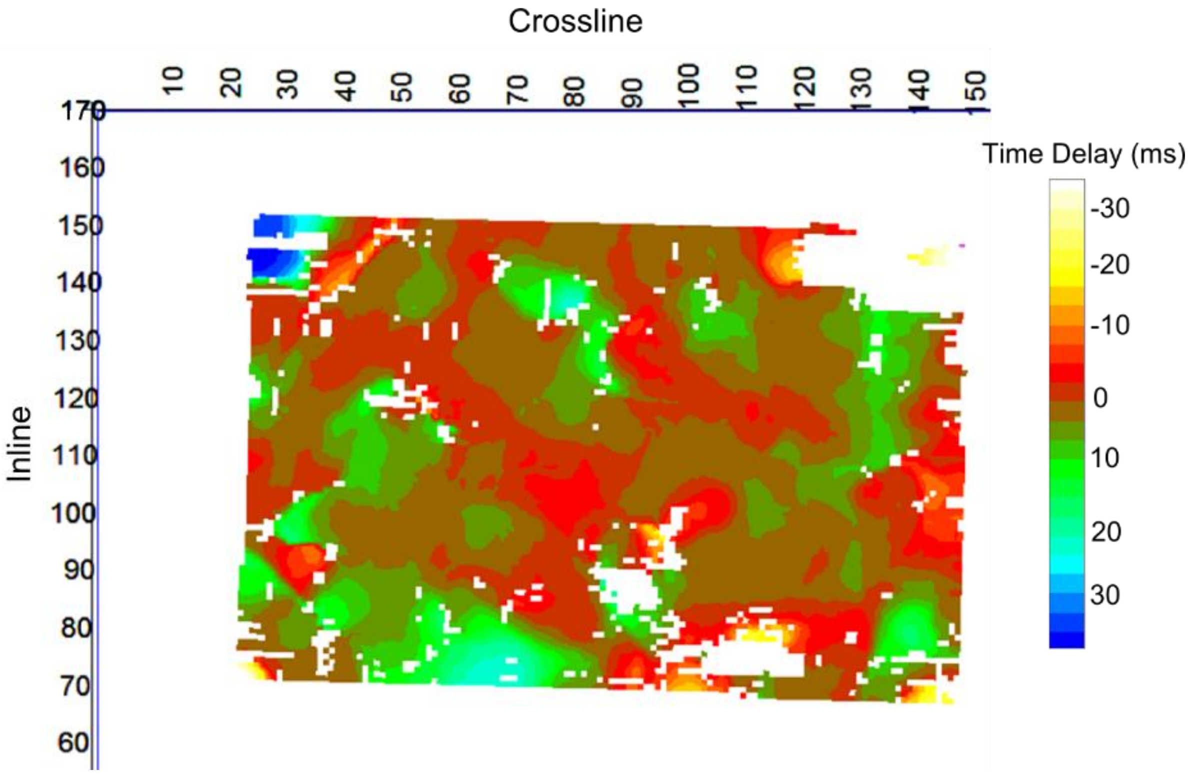

Figure 7.12. Time delay map created through differencing of P-SV Fast and P-SV Slow isochron maps constructed from the Viola and Basement horizons. The wide range of both positive and negative time delays make this result unrealistic geologically.

7.6 AVO and ray trace modeling

The quality of the P-SV data at Arbuckle Group depth was markedly worse than that of the P-P data. AVO and ray trace modeling were completed to gain a better understanding of the difference in quality of the two data sets. A close look at the synthetic seismic trace from well 15-189-22781 (Figure 5.2) reveals that the "basement" reflection is caused primarily by the contrast in elastic properties between the Arbuckle Group dolomite and the underlying Gunter Sandstone. The contrast between the Gunter Sandstone and the granite basement is relatively weak, in comparison.

Reflection coefficient magnitudes were modeled as a function of incidence angle using Eq. (2.4). The modeling shows a maximum P-P reflection coefficient magnitude of 0.14 at zero degrees of incidence and a maximum P-SV reflection coefficient magnitude of 0.93 at an incidence angle of 35 degrees. To estimate the maximum angle of incidence of the P-SV data, ray trace modeling was performed with Eq. (2.5) and a six-layer velocity model. The modeling shows a P-SV incidence angle of 22 degrees at the Cutter 3D-3C survey maximum offset of 1056 m. This corresponds to a P-SV reflection coefficient magnitude of 0.08. This reflection coefficient magnitude is 43% less than the maximum P-P reflection coefficient magnitude and likely contributes to poor P-SV data quality observed at basement depth.

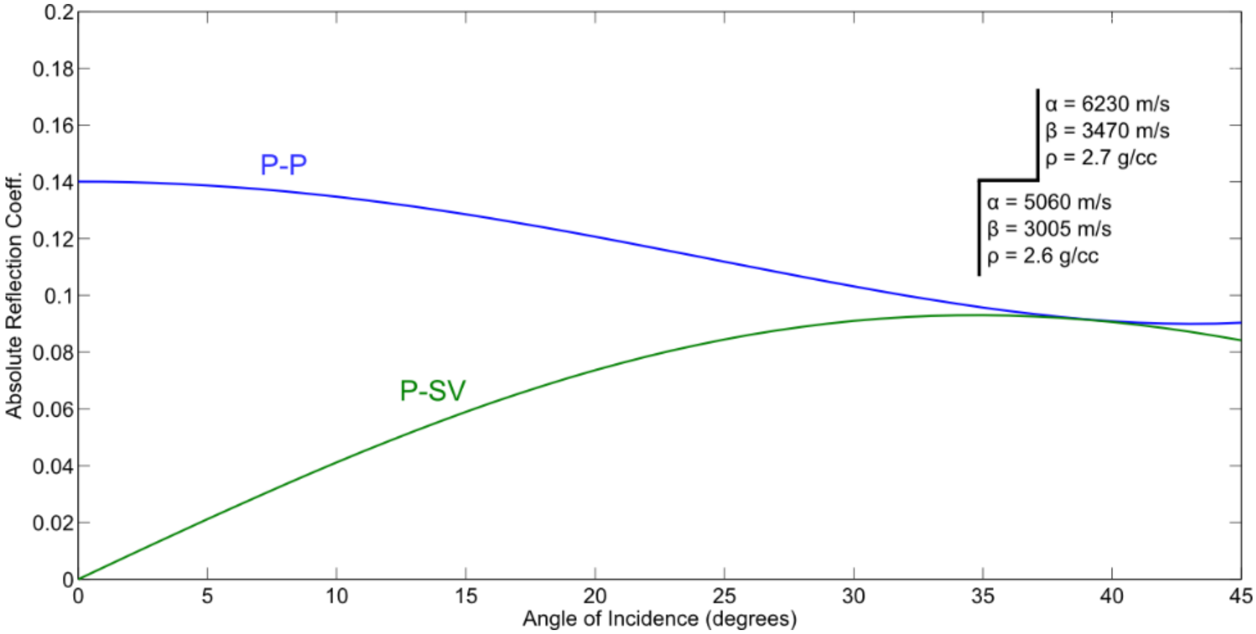

Figure 7.13. AVO modeling of the Arbuckle Group – Gunter Sandstone contact. For incidence angles less than 37 degrees, P-P reflectivity exceeds P-SV reflectivity.

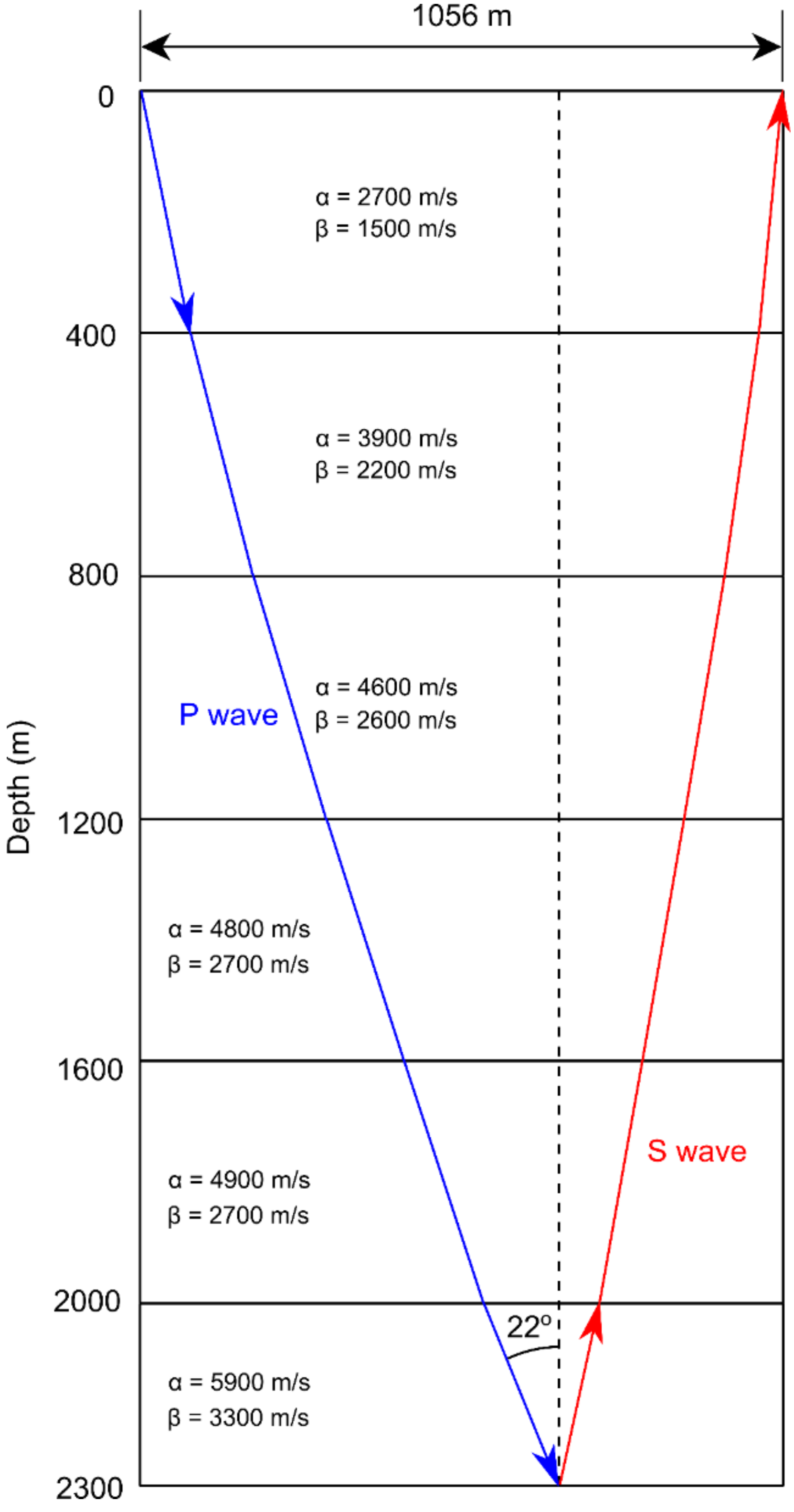

Figure 7.14. Ray trace modeling of a P-SV basement reflection at maximum offset of 1056 m. The P wave incidence angle at maximum offset is ~22 degrees. An incidence angle of 22 degrees corresponds to a P-SV absolute reflection coefficient of 0.08.

7.7 Summary of Arbuckle Group results

A strong correlation exists between neutron porosity and P-impedance within the well modeled for the Arbuckle Group. Model-based P-impedance inversion appears to be an effective method for approximating P-impedance, and thus porosity, within the Arbuckle Group at Cutter Field. More well control is necessary to test the accuracy of the inverted volume away from well 15-189-22781. The P-impedance distribution in the Arbuckle can be approximated by a three-layer model: a high P-impedance layer in the upper Arbuckle, a low P-impedance layer in the middle Arbuckle, and a high P-impedance layer in the lower Arbuckle.

This three-layer trend is laterally extensive across the inverted volume and P-impedance layer boundaries appear to coincide with flow unit boundaries. These results and suggest that porosity and perhaps flow units within the Arbuckle Group can be approximated by a three-layer model, on a field-wide scale.

The P-SV data exhibits poor quality and is not useful for quantitative interpretation. P-P and P-SV imaging of the Arbuckle could likely be improved by acquiring longer offsets. As a general rule, maximum offset should be equal to target depth (Vermeer, 2012). The maximum offset of the Cutter 3D-3C survey is ~1/2 of basement depth. Acquiring pure S wave data (SH-SH) would improve the probability of successful fracture characterization because it would double the expected time delay between fast and slow S waves.

Chapter 8: Conclusions

The objective of this study was to test the accuracy with which 3D-3C seismic data could delineate Upper Morrow Sandstone reservoirs and predict rock properties within the Arbuckle Group at Cutter Field. Overall, the P-SV data did not provide any additional benefits over the conventional P-P data. The Upper Morrow Sandstone reservoir could not be conclusively delineated with either data set. Model-based inversion of the P-P data showed potential for predicting porosity and mapping flow units within the Arbuckle Group. Key findings and recommendations are summarized in the following sections.

8.1 Key findings

1. AVO modeling of the Upper Morrow Sandstone interfaces shows that P-SV waves only provide a slight advantage (< 30%) in terms of reflection coefficient magnitude and only for incidence angles greater than ~15 degrees. The signal-to-noise ratio of the P-SV data is visibly lower than that of the P-P data.
2. The Upper Morrow Sandstone has a maximum thickness of 11.3 m at Cutter Field. In terms of seismic wavelengths, 11.3 m is approximately 1/8 λ for the P-P data and 1/12 λ for the P-SV data. The resolution of both data sets is well below the resolution limit of 1/4 λ.
3. At well locations where the UMS is absent, amplitude magnitudes of horizon UMS2 have an uncertainty equivalent to ± 43% of the mean of the amplitudes magnitudes. Uncertainty in amplitude magnitudes from noise, wavelet phase, and fluid saturation can account for ± 30% of the uncertainty in amplitude magnitudes. The remaining ± 13% of uncertainty is likely due to lateral changes in the stratigraphy directly surrounding the UMS reservoir, poor amplitude preservation during seismic processing, and acquisition artifacts.

4. Rms Instantaneous frequency values of 43 ± 2 Hz are observed at well locations where Upper Morrow Sandstone thickness is greater than 5 m whereas rms values of 45 ± 6 Hz are observed at well locations where thickness is less than 5 m. The difference in the rms values is statistically significant at the 90% confidence interval.
5. Neutron porosity within the Arbuckle Group ranges from 3-13%. Well logs show an inverse relationship between porosity and P-impedance within the Arbuckle Group with an r-squared value of 0.56 and a standard error of regression of 2 porosity units. This correlation is significant at the 99.9% confidence interval.
6. Post-stack model-based inversion is an effective method for approximating P-impedance and within the Arbuckle Group at Cutter Field. The linear relationship between the inverted P-impedance log and the original P-impedance log at well 15-189-22781 had an r-squared value of 0.74 and a standard error of regression of 1094 (m/s)*(g/cc).
7. P-impedance within the Arbuckle Group can be approximated by a three-layer model: a high P-impedance layer in the upper Arbuckle, a low P-impedance layer in the middle Arbuckle, and high P-impedance layer in the lower Arbuckle.
8. Interpreted flow unit within the Arbuckle Group appear to coincide with the three P-impedance layers.
9. P-SV data exhibit poor quality at Arbuckle Group depth and are not useful for quantitative interpretation.
10. Distinct karst collapse features are identifiable in the seismic data and appear to extend into the Arbuckle Group.

These results demonstrate varying degrees of success at overcoming seismic imaging challenges posed by the Arbuckle Group and the Upper Morrow Sandstone at Cutter Field. In particular, the quality and resolution of the P-SV data proved to be inadequate for delineating the UMS and characterizing rock properties within the Arbuckle Group. P-impedance inversion proved to be a valuable technique for making Arbuckle Group porosity predictions and for identifying internal stratigraphy within the Arbuckle Group that was not clearly evident in the seismic amplitude data Investigators should draw upon these results to guide seismic acquisition and interpretation practices in geologic settings analogous to Cutter Field. Recommendations are given in the following section.

8.2 Recommendations

P-SV data is not ideal for imaging the Upper Morrow Sandstone reservoir at Cutter Field. In comparison to P-P data it has lower resolution, lower signal-to-noise ratio, and provides only a slight advantage in reflection strength. Future efforts should focus on improving the resolution and signal-to-noise ratio of the P-P data. Extreme care should be taken to preserve relative amplitude information during seismic processing. The resolution of the P-P data set could be potentially improved by removing long offsets from the P-P stack. However, the benefits of higher resolution could be negated by a lower signal-to-noise ratio.

The relationship between Upper Morrow Sandstone thickness and instantaneous frequency at Cutter Field is inconclusive. Seismic data collected over Upper Morrow Sandstone reservoirs in other locations should be examined to determine if the instantaneous frequency result is reproducible. Future P-P seismic acquisition projects at Cutter Field should consider nonlinear sweeps in order to improve resolution. A nonlinear sweep method developed by Baeten and van der Heijden (2008) retrieved frequencies up to 150 Hz for depths down to 2000 m. AVO methods, including pre-stack inversion, should be considered for future studies of the Arbuckle Group.

References

Baeten, G., & van der Heijden, H. (2008). Improving S/N for high frequencies. The Leading Edge, 27(2), 144-153.

Bhattacharya, S., Byrnes, A., Gerlach, P. M., & Olea, R. A. (2002). Reservoir characterization to inexpensively evaluate the exploration potential of a small Morrow-incised valley-fill field. Kansas Geological Survey Open-file Report 2002-9, poster. Retrieved from: http://www.kgs.ku.edu/PRS/Poster/2002/2002-9/index.html

Bliefnick, D. M., & C., B. W. (1992). Karst-related diagenesis and reservoir development in the Arbuckle Group, Wilburton Field, Oklahoma. American Association of Petroleum Geologists Bulletin, 76(4), 571-572.

Blott, J. E., & Davis, T. L. (1999). Morrow sandstone reservoir characterization: a 3-D multicomponent seismic success. The Leading Edge, 18(3), 394.

Brown, A. R. (2011). Interpretation of three-dimensional seismic data (7th ed. AAPG Memoir 42; SEG Investigations in Geophysics, No. 9). Tulsa, OK: The American Association of Petroleum Geologists; Society of Exploration Geophysicists, 103-106.

Carr, T. R., Merriam, D. F., & Bartley, J. D. (2005). Use of relational databases to evaluate regional petroleum accumulation, groundwater flow, and CO2 sequestration in Kansas. AAPG Bulletin, 89(12), 1607-1627.

Cerveny, V. (2001). Seismic Ray Theory. New York: Cambridge University Press, 35.

Chung, H., Lawton D. (1995). Frequency characteristics of seismic reflections from thin beds. Canadian Journal of Exploration Geophysics, 31 (1 & 2), 32-37.

Fadolalkarem, Y. (2015). Pre-stack seismic attribute analysis of the Mississippian Chert and the Arbuckle Group at the Welling Field, south-central Kansas. Unpublished master's thesis, The University of Kansas, Lawrence, KS.

Franseen, E. K. (2000). A review of Arbuckle Group strata in Kansas from a sedimentologic perspective: Insights for future research from past and recent studies. The Compass: Journal of Earth Sciences Sigma Gamma Epsilon, 75(2 & 3), 68-69.

Franseen, E. K., Byrnes, A. P., Cansler, J. R., Steinhauff, D. M., & Carr, T. R. (2004). The geology of Kansas: Arbuckle Group. Current Research in Earth Sciences, Kansas Geological Survey Bulletin, 250(2), 1-43.

Gerlach, P. (2014). Subsurface fluid chemistry and flow regime analysis. In W. L. Watney & J. Rush (Eds.), Modeling CO2 sequestration in saline aquifer and depleted oil reservoir to evaluate regional CO2 sequestration potential of Ozark Plateau aquifer system, south-central Kansas, 19th quarterly progress report. DE-FE0002056. University of Kansas Center for Research and Kansas Geological Survey. Retrieved from: http://www.kgs.ku.edu/PRS/Ozark/Reports/2014/Q19_2014.pdf

Gregory, A. R. (1997). Aspects of rock physics from laboratory and log data that are important to seismic interpretation. AAPG memoir 26, 15-46.

Halverson, J. R. (1988). Seismic expression of the Upper Morrow sands, western Anadarko Basin. Geophysics, 53(3), 290-303.

Hardage, B. A. (2007). Fundamentals of Geophysics. In E. D. Holstein (Ed.), Reservoir Engineering and Petrophysics, 5, 33. Richardson, TX: Society of Petroleum Engineers.

Hardage, B. A., DeAngelo, M. V., Murray, P. E., & Sava, D. (2011). Multicomponent Seismic Technology. Tulsa, Oklahoma: Society of Exploration Geophysicists, 79, 147.

Johnson, K. S. (1989). Geologic evolution of the Anadarko basin. Oklahoma Geological Survey Circular, 90, 3-12.

Kansas Geological Survey. (2015). Digital petroleum atlas, Cutter field general information. 2015. Retrieved from: http://chasm.kgs.ku.edu/ords/gemini.dpa_general_pkg.build_general_web_page?sFieldKID=1000148969

Knott, C. G. (1899). Reflexion and refraction of elastic waves, with seismological applications. Philosophical Magazine Series 5, 48(290), 64-97.

Latimer, R. B. (2011). Inversion and interpretation of impedance data. In S. E. Lauback & V. Grechka (Ed.), Interpretation of Three-Dimensional Seismic Data (7th ed., AAPG Memoir 42, SEG Investigations in Geophysics, No. 9). Tulsa, Oklahoma: The American Association of Petroleum Geologists and the Society of Exploration Geophysicists, 309-346.

Liner, C. L. (2004). Elements of 3D Seismology (2nd ed.). Tulsa, Oklahoma: Penwell Corporation, 168.

Liu, Y., Li, C., (1997). Some methods for estimating the signal/noise ratio of seismic data. Oil Geophysical Prospecting, 32, 257-262.

Hampson-Russell Software Services (1999). Theory of the strata program. 2015. Retrieved from http://www.cgg.com/data/1/rec_docs/585_STRATA_Theory.pdf

Merriam, D. F. (1963). The geologic history of Kansas. Kansas Geological Survey Bulletin, 162. Retrieved from: http://www.kgs.ku.edu/Publications/Bulletins/162/index.html

Mueller, M. C. (1992). Using shear waves to predict lateral variability in vertical fracture intensity. The Leading Edge, 11(2), 29-35.

Nissen, S. E., Bhattacharya, S., Doceton, J., & Watney, W. L. (2007). Improving geologic and engineering models of midcontinent fracture and karst-modified reservoirs using new 3-D seismic attributes. SEISKARST, Dec. 2007 Semi-Annual Report, 1-40. Retrieved from: http://www.kgs.ku.edu/SEISKARST/DE_FC26_04NT15504_Dec07.pdf

Pujol, J. (2003). Elastic wave propagation and generation in seismology. Cambridge, United Kingdom: Cambridge University Press, 129-187.

Russell, B. H. (1988). Introduction to Seismic Inversion Methods. Tulsa, OK: Society of Exploration Geophysicists, 8-3.

Salcedo, G. A. (2004). Depositional environments of Lower Pennsylvanian reservoir sandstones, southwestern Kansas. Kansas Geological Survey Open-file Report 2004-18, poster. Retrieved from: http://www.kgs.ku.edu/PRS/publication/2004/AAPG/LPenn/index.html

Singh, P., & Davis, T. (2011). Advantages of shear wave seismic in morrow sandstone detection. International Journal of Geophysics, 2011, 1-16.

Sondergeld, C. H., & Rai, C. S. (1992). Laboratory observations of shear-wave propagation in anisotropic media. The Leading Edge, 11(2), 38-43.

Stein, S., & Wysession, M. (2003). An introduction to seismology, earthquakes, and earth structure. Malden, Massachusetts: Blackwell Publishing Ltd, 29-118.

Stewart, R. R., Gaiser, J. E., Brown, J. R., & Lawton, D. C. (2002). Converted-wave seismic exploration: Methods. Geophysics, 67(5), 1348-1363.

Upadhay, S. K. (2004). Seismic reflection processing. Heidelberg, Germany: Springer, 194.

Van Dok, R., & Gaiser, J. (2001). Stratigraphic description of the Morrow Formation using mode-converted shear waves: Interpretation tools and techniques for three land surveys. The Leading Edge, 20(9), 1042-1047.

Vermeer, G. J. O. (2012). 3D seismic survey design (2nd ed.). Tulsa, OK: Society of Exploration Geophysicists, 208.

Walpole, R. E., Myers, R. H., & Myers, S. L. (2012). Probability and statistics for engineers and scientists (9th ed.). Boston, MA: Prentice Hall, 350, 404.

Walters, R. F. (1958). Differential entrapment of oil and gas in Arbuckle dolomite of Central Kansas. Bulletin of the American Association of Petroleum Geologists, 42(9), 2133-2173.

Wheeler, D. M., Scott, A. J., Coringrato, V. J., & Devine, P. E. (1990). Stratigraphy and depositional history of the Morrow formation, southeast Colorado and southwest Kansas. In S. A. Sonnenberg, L. T. Shannon, K. Rader, W. F. von Drehle, & G. W. Martin (Eds.), Morrow sandstones of southeast Colorado and adjacent areas (pp. 9-36): Rocky Mountain Association of Geologists.

Widess, M. B. (1973). How thin is a thin bed? Geophysics, 38(6), 1176-1180.

Zoeppritz, K. (1919). Uber reflexion und durchgang seismischer Wellen durch Unstetigkerlsflaschen. Uber Erdbebenwellen VII B, Nachrichten der Koniglichen Gesellschafl der Wissenschaflen zu Gottingen, Math. Phys., K1, 57-84.